Grid Computing for LHC and Methods for W Boson Mass Measurement at CMS

Zur Erlangung des akademischen Grades eines
DOKTORS DER NATURWISSENSCHAFTEN
von der Fakultät für Physik der
Universität Karlsruhe (TH)

genehmigte

DISSERTATION

von

Dipl.-Phys. Christopher Jung

aus Karlsruhe

Contents

Chapter 1

Introduction

One of the many intriguing fields of physics is particle physics, which tries to answer amongst other questions one that has been raised by humans for thousands of years, "what is the world made of?" The modern version of this question is "what are the fundamental particles and their interactions?" Today's best answer is the Standard Model (SM) of particle physics, which describes the fundamental particles and their electromagnetic, weak and strong interactions with great accuracy. In the SM, a special field is introduced so that particles can acquire their masses; this field is called the Higgs field. Its scalar boson is the only particle of the SM that has not been discovered yet, the Higgs boson.

In spring of 2008, the Large Hadron Collider (LHC) and its four particle detectors will go on-line (chapter 3). Because of LHC's high center-of-mass energy and its large design luminosity, not only the Higgs boson's mass will be measured, but also the precision knowledge on many other SM parameters, such as the W boson mass and the top quark mass, will be gained. In addition, physics models beyond the SM will be investigated, such as Supersymmetry and extra dimensional models.

In the SM, the mass of the W boson is dependent on the masses of the Z boson, the top quark and Higgs boson. With the Z boson's mass already precisely measured at the Large Electron Proton Collider (LEP), the measurement of the Higgs boson's mass and the precision measurements of the top quark mass and of the W boson mass at the LHC will allow a very good test on the electroweak corrections in the SM (chapter 2).

High event rates and large event sizes of the four detectors at the LHC need a new model for computing, access and storage. This model is grid computing, which will be explained in chapter 4. Since even simulating the events needed for this thesis would have exceeded the resources of the local computing cluster, all simulation was performed on the grid.

This thesis presents two methods for determining the W boson mass with the CMS

(<u>C</u>ompact <u>M</u>uon <u>S</u>olenoid) detector. Both methods use similarities between W boson and Z boson events. Further, the thesis will investigate the muonic decay channels of the massive intermediate vector bosons.

These studies require complex software tools for simulation, reconstruction and physics analysis. The tools will be explained in more detail in chapter 5.

The physics analysis itself will be presented in chapter 6. Large parts of this analysis have been published in [PhysJG] and included in the CMS Physics Technical Design report (Volume 2) [PTDR2]. The statistical uncertainty and systematic effects for data corresponding to an integrated luminosity of one inverse femtobarn taken with the CMS detector are studied for both of these methods.

Chapter 2

The W Boson in the Standard Model

In the Standard Model of particle physics, the W boson and the Z boson mediate the weak interaction. This chapter outlines the Standard Model, summarizes the latest mass and width measurements of W and Z boson, discusses the correlation between the masses of of the W boson, of the top quark, and of the Higgs boson, describes the theory of the W and Z boson production, and explains the concept of the transverse mass.

2.1   The Standard Model of Particle Physics

Despite its plain name, the Standard Model of particle physics is powerful and gives the best description of the elementary particles and their interactions that we know today. Detailed descriptions are given in many publications, e.g. the recent ones by [Pich1], [Pich2] and [Schm]. This section has been primarily inspired by [Pich1]. Out of the four known interactions of Nature, the Standard Model considers three. At the energies of the Standard Model, gravitation, described by General Relativity, is insignificant and can be neglected. The weak interaction and electromagnetism have been unified by Glashow, Weinberg and Salam to the electroweak interaction; the respective symmetry group is $SU(2)_L \times U(1)_Y$. The strong interaction is described by Quantum Chromodynamics (QCD), which is a $SU(3)_C$ theory.

There are two types of fundamental particles: fermions and bosons. Bosons have integer spin, while fermions carry half-integer spin. In the Standard Model there are two kinds of fermions: leptons and quarks, each of these groups having a substructure of three families.

2.1.1   Gauge Theories

Gauge theories are theories, in which Lagrangians have not only global symmetries but also local symmetries. These local symmetries are of special importance for the Standard Model of particle physics. First, an easy example from electrodynamics is given, followed by gauge invariance in Quantum Electrodynamics (QED).

Gauge Invariance in Electrodynamics

The Maxwell equations (e.g. [Jackson]) in vacuum are given by

$$\vec{\nabla} \cdot \vec{E} = \varrho, \tag{2.1}$$

$$\vec{\nabla} \cdot \vec{B} = 0, \tag{2.2}$$

$$\vec{\nabla} \times \vec{B} = \vec{J} + \frac{\partial \vec{E}}{\partial t}, \tag{2.3}$$

$$\vec{\nabla} \times \vec{E} = -\frac{\partial \vec{B}}{\partial t}. \tag{2.4}$$

One can introduce the potentials V and $\vec{A}$ by requiring

$$\vec{E} = -\vec{\nabla}V - \frac{\partial \vec{A}}{\partial t} \text{ and } \vec{B} = \nabla \times \vec{A}. \tag{2.5}$$

By using the covariant notations

$$A^\mu := (V, \vec{A}) \text{ and } J^\mu := (\varrho, \vec{J})$$

and defining the field strength tensor

$$F^{\mu\nu} := \partial^\mu A^\nu - \partial^\nu A^\mu, \tag{2.6}$$

the Maxwell equations (2.1) and (2.3) can be written as

$$\partial_\mu F^{\mu\nu} = J^\nu, \tag{2.7}$$

and the Maxwell equations (2.2) and (2.4) can be written as

$$\partial_\alpha F_{\beta\gamma} + \partial_\beta F_{\gamma\alpha} + \partial_\gamma F_{\alpha\beta} = 0.$$

Equation (2.7), as well as the physical fields $\vec{E}$ and $\vec{B}$, is invariant under the gauge transformation

$$A^\mu \to A^\mu + \partial^\mu \Lambda,$$

with $\Lambda = \Lambda(x)$ being an arbitrary scalar function. Therefore, the same physics is given by different A^μ.

We can derive $\partial_\mu J^\mu = 0$ out of $\partial_\mu \partial_\nu F^{\mu\nu} = 0$. Using the Lorentz gauge

$$\partial_\mu A^\mu = 0,$$

the equation

$$\partial_\mu F^{\mu\nu} = \Box A^\nu - \partial^\nu(\partial_\mu A^\mu) = J^\nu$$

is reduced to

$$\Box A^\mu = J^\mu,$$

which is the Klein-Gordon equation for massless particles with a source term. There is an invariance remaining,

$$A^\mu \to A^\mu + \partial^\mu \Lambda \text{ with } \Box\Lambda = 0,$$

resulting in two polarization states for photons.

Quantum Electrodynamics

The Lagrangian $\mathcal{L}_{fD}$ describes a free Dirac fermion of mass m,

$$\mathcal{L}_{fD} = \bar{\psi}(i\gamma^\mu \partial_\mu - m)\psi.$$

This Lagrangian is invariant under global $U(1)$ transformations

$$\psi(x) \xrightarrow{U(1)} \psi'(x) = e^{i\Theta}\psi(x),$$

with Θ being an arbitrary real constant. In this case, the phase has no physical meaning.

The Lagrangian loses its invariance when the phase transformation is space-time dependent, i.e $\Theta = \Theta(x)$, which is a local phase redefinition. The derivatives of ψ change under the local phase transformation in the following way

$$\partial_\mu \psi(x) \xrightarrow{U(1)} e^{i\Theta}(\partial_\mu + i\partial_\mu\Theta)\psi(x). \tag{2.8}$$

To make the $U(1)$ phase invariance hold locally, we need to change the Lagrangian in such a way that the $i\partial_\mu\Theta$ term in (2.8) is canceled out. We do so by introducing a new spin-1 field, the photon field, $A_\mu(x)$, which transforms as

$$A_\mu(x) \xrightarrow{U(1)} A'_\mu(x) := A_\mu(x) + \frac{1}{e}\partial_\mu\Theta \tag{2.9}$$

(for the moment the factor $\frac{1}{e}$ is included for convenience) and by defining the covariant derivative

$$D_\mu \psi(x) := [\partial_\mu - ie A_\mu(x)]\psi(x),$$

which has the property of transforming as the field

$$D_\mu \psi(x) \xrightarrow{U(1)} e^{i\Theta} D_\mu \psi(x).$$

The real constant e introduced in (2.9) is arbitrary, it is identified with the electric charge of the fermion.

To write down the full Lagrangian, we need to add a gauge-invariant kinetic term

$$\mathcal{L}_{kin} := -\frac{1}{4} F_{\mu\nu}(x) F^{\mu\nu}(x),$$

with $F_{\mu\nu}$ being the electromagnetic field strength tensor defined in (2.6). A possible mass term for the gauge field,

$$\mathcal{L}_M = \frac{1}{2} m_\gamma^2 A^\mu A_\mu,$$

is forbidden, since it would violate gauge invariance, i.e. it is not invariant under (2.9). Therefore, the photon is predicted to be massless. The overall QED Lagrangian is

$$\mathcal{L}_{QED} = \bar{\psi}(i\gamma^\mu D_\mu - m)\psi - \frac{1}{4} F_{\mu\nu} F^{\mu\nu}. \tag{2.10}$$

2.1.2   Quantum Chromodynamics

As an example for a non-Abelian gauge theory, QCD will be considered. In QCD, there is an extra quantum number called color (q^1=red, q^2=green, q^3=blue). In the following, a quark field of color α and flavor f will be denoted by q_f^α. A vector notation will be used in color space, $q_f^T := (q_f^1, q_f^2, q_f^3)$.

The free Lagrangian is given by

$$\mathcal{L}_0 = \sum_f \bar{q}_f (i\gamma^\mu \partial_\mu - m_f) q_f, \tag{2.11}$$

which is invariant under arbitrary $SU(3)_C$ transformations in color space:

$$q_f^\alpha \xrightarrow{SU(3)_C} q_f'^\alpha = U_\beta^\alpha q_f^\beta \quad (\text{with } UU^\dagger = U^\dagger U = 1 \text{ and } \det U = 1). \tag{2.12}$$

From now on, the $SU(3)_C$ matrices will be parametrized in the form

$$U = e^{i\frac{\lambda^a}{2}\Theta_a}, \tag{2.13}$$

where Θ_a are real parameters and $\frac{1}{2}\lambda^a$ ($a \in \{1, \ldots, 8\}$) are the generators of the fundamental representation of $SU(3)_C$. The traceless matrices λ^a, called the Gell-Mann matrices, have the following commutation relation:

$$\left[\lambda^a, \lambda^b\right] = i2f^{abc}\lambda^c,$$

with f^{abc} being the real and totally antisymmetric $SU(3)_C$ structure constants. An explicit realization of the λ^a's can be found in many textbooks, e.g. in [Wein].

Now we require the Lagrangian to be invariant under local $SU(3)_C$ transformations, i.e. we allow $\Theta_a = \Theta_a(x)$ in (2.13). To do so, we change the derivatives in (2.11) to covariant objects. Since we have eight generators, we need eight different gauge bosons $G_a^\mu(x)$:

$$D^\mu := \left(\partial^\mu - ig_s\frac{\lambda^a}{2}G_a^\mu(x)\right) =: \left(\partial^\mu - ig_sG^\mu(x)\right).$$

The fields G^μ are called the gluon fields. For easier notation we use the compact matrix notation $(G^\mu(x))_{\alpha\beta} := \left(\frac{\lambda^a}{2}\right)_{\alpha\beta} G_a^\mu(x)$. We want $D^\mu q_f$ to transform in the same way as the color vector q_f:

$$D^\mu \to (D^\mu)' = UD^\mu U^\dagger, \ G^\mu \to (G^\mu)' = UG^\mu U^\dagger - \frac{i}{g_s}(\partial^\mu U)U^\dagger.$$

Under infinitesimal transformations $\delta\Theta$, quark fields and gluon fields change in the following way:

$$q_f^\alpha \to (q_f^\alpha)' = q_f^\alpha + i\left(\frac{\lambda^a}{2}\right)_{\alpha\beta}\delta\Theta_a q_f^\beta,$$

$$G_a^\mu \to (G_a^\mu)' = G_a^\mu + \frac{1}{g_s}\partial^\mu(\delta\Theta_a) - f^{abc}\delta\Theta_b G_c^\mu.$$

The noncommutativity of the $SU(3)_C$ matrices results in an additional term containing the gluon fields themselves. Also, there is a unique $SU(3)_C$ coupling g_s.

For building the gauge-invariant kinetic term for the gluon fields we need to introduce corresponding field strengths:

$$G^{\mu\nu}(x) := \frac{i}{g_s}[D^\mu, D^\nu] = \partial^\mu G^\nu - \partial^\nu G^\mu - ig_s[G^\mu, G^\nu] = \frac{\lambda^a}{2}G_a^{\mu\nu}(x),$$

$$G_a^{\mu\nu}(x) = \partial^\mu G_a^\nu - \partial^\nu G_a^\mu + g_s f^{abc} G_b^\mu G_c^\nu.$$

Note that $G^{\mu\nu}$ and the color trace $\text{tr}(G^{\mu\nu}G_{\mu\nu}) = \frac{1}{2}G_a^{\mu\nu}G_{\mu\nu}^a$ remain invariant under a gauge transformation.

Normalizing the gluon kinetic term properly, we get the Lagrangian of QCD:

$$\mathcal{L}_{QCD} := \sum_f \bar{q}_f(i\gamma^\mu \ D_\mu - m_f)q_f - \frac{1}{4}G_a^{\mu\nu}G_{\mu\nu}^a.$$
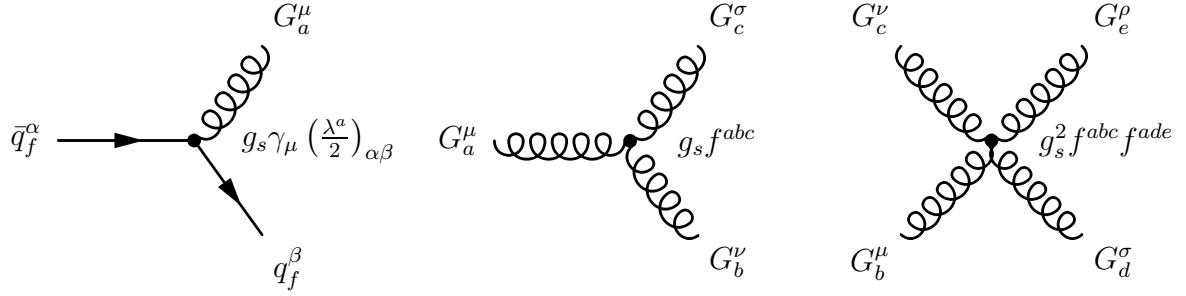
Figure 2.1: The interaction vertices in the QCD Lagrangian: basic quark-quark-gluon vertex, three-gluon self-interaction, four-gluon self-interaction.

When decomposing the Lagrangian, one sees that the color interaction between quarks and gluons involves the generator of the fundamental representation $\frac{1}{2}\lambda^a$ and that there are cubic and quartic self-interactions of gluons. All interaction vertices of the QCD Lagrangian are shown in Figure 2.1.

2.1.3   Electroweak Interaction

For a theory of the electroweak interaction, the following experimental facts have to be considered.

- Flavor-changing currents couple only to left-handed fermions and right-handed anti-fermions; this is a maximal breaking of parity.

- A flavor-changing current carries an electrical charge of $\pm e$.

- All fermion doublets couple to flavor-changing currents with the same strength.

- The doublet partners of u, c, t quarks are not the mass eigenstates d, s, b, but are given by
$$\begin{pmatrix} d' \\ s' \\ b' \end{pmatrix} = V_{CKM} \begin{pmatrix} d \\ s \\ b \end{pmatrix}.$$
  V_{CKM} is a unitary matrix called the Cabibbo-Kobayashi-Maskawa matrix. This matrix characterizes flavor-mixing phenomena.

- In neutral currents, all interaction vertices are flavor conserving.

- Fermions with the same electric charge Q_f have the same coupling to flavor conserving currents. Although neutrinos do not have any electrical charge they couple to flavor-conserving currents as well.

- Flavor-conserving currents couple differently to left- and right-handed fermions; only left-handed neutrinos couple to flavor-conserving currents.

- The neutrino masses are tiny (and therefore are neglected in the Standard Model).

These experimental requirements show that we need an elaborate structure in order to describe the weak interaction. Since left-handed fermions should appear in doublet, we start with the simplest group with a doublet representation, $SU(2)$. Considering QED, we require an additional $U(1)$ group. Hence we have to consider a

$$G := SU(2)_L \otimes U(1)_Y$$

symmetry, with L standing for left-handed and Y to be specified later.

For the sake of simplicity, only the first family of quarks (u,d) will be considered and the notation

$$\psi_1(x) = \begin{pmatrix} u \\ d \end{pmatrix}_L, \quad \psi_2(x) = u_R, \quad \psi_3(x) = d_R$$

will be used; for the lepton sector the notation is

$$\psi_1(x) = \begin{pmatrix} \nu_e \\ e^- \end{pmatrix}_L, \quad \psi_2(x) = \nu_R, \quad \psi_3(x) = e_R^-.$$

The free Lagrangian

$$\mathcal{L}_0 = i\bar{u}\gamma^\mu \partial_\mu u(x) + i\bar{d}(x)\gamma^\mu \partial_\mu d(x) = \sum_{j=1}^{3} i\bar{\psi}_j(x)\gamma^\mu \partial_\mu \psi_j(x)$$

is invariant under global transformations G in flavor space:

$$\psi_1(x) \xrightarrow{G} e^{iy_1\beta} U_L \psi_1(x),$$
$$\psi_2(x) \xrightarrow{G} e^{iy_2\beta} \psi_2(x),$$
$$\psi_3(x) \xrightarrow{G} e^{iy_3\beta} \psi_3(x).$$

The parameters y_i ($i \in \{1, 2, 3\}$) are called hypercharges, β is a real free rotation angle and the U_L,

$$U_L := e^{i\frac{\sigma_i}{2}\alpha_i},$$

is a $SU(2)_L$ transformation only acting on the doublet field ψ_1 (U_L is non-Abelian like in QCD, due to non-commuting Pauli matrices). α_i are also free rotation angles.

In the free Lagrangian no mass term was included, because it would have spoiled the symmetry considerations by mixing left- and right-handed fields (the masses of the vector bosons will be introduced via the Higgs mechanism in subsection 2.1.4).

According to the gauge principle, the Lagrangian is required to be invariant under local gauge transformations, so we use $\alpha^i = \alpha^i(x)$ and $\beta = \beta(x)$. Yet again, we need to change the fermion derivatives by covariant objects; having four gauge parameters $(\alpha^1, \alpha^2, \alpha^3, \beta)$, we need four gauge bosons:

$$
\begin{aligned}
D_\mu \psi_1(x) &:= \left(\partial_\mu - ig\tilde{W}_\mu(x) - ig'y_1 B_\mu(x) \right) \psi_1(x), \\
D_\mu \psi_2(x) &:= \left(\partial_\mu - ig'y_2 B_\mu(x) \right) \psi_2(x), \\
D_\mu \psi_3(x) &:= \left(\partial_\mu - ig'y_3 B_\mu(x) \right) \psi_3(x);
\end{aligned}
$$

with $\tilde{W}_\mu(x) = \frac{\sigma_i}{2} W_\mu^i(x)$ being a $SU(2)_L$ matrix field. So we have the right number of gauge fields for $W^\pm$, Z and γ.

We want $D_\mu \psi_j(x)$ to transform in the same way as the $\psi_j(x)$ fields; this requirement fixes the transformation properties:

$$
\begin{aligned}
B_\mu(x) &\xrightarrow{G} B_\mu(x) + \frac{1}{g'}\partial_\mu\beta(x), \\
\tilde{W}_\mu(x) &\xrightarrow{G} U_L(x)\tilde{W}_\mu U_L^\dagger(x) - \frac{i}{g}\partial_\mu U_L(x)U_L^\dagger(x);
\end{aligned}
$$

with $U_L(x) := e^{i\frac{\sigma_i}{2}\alpha^i(x)}$.

Because of the symmetry groups used, there are similarities to the results in the previous subsections:

- The transformation B_μ is identical to the transformation obtained in QED for the photon.

- The $SU(2)_L$ W_μ^i fields transform analogously to the gluon fields in QCD.

The ψ_j couplings to B_μ are free, allowing the hypercharges to be arbitrary parameters. This does not apply to the W_μ^i, since the $SU(2)_L$ commutation relation is non-linear; we have only one $SU(2)_L$ coupling g.

The Lagrangian

$$
\mathcal{L} = \sum_{j=1}^{3} i\bar{\psi}_j(x)\gamma^\mu D_\mu \psi_j(x) \tag{2.14}
$$

has the property of being invariant under local G transformations. In order to have a gauge-invariant kinetic term for the gauge fields, field strengths will be introduced:

$$
\begin{aligned}
B_{\mu\nu} &:= \partial_\mu B_\nu - \partial_\nu B_\mu, \\
\tilde{W}_{\mu\nu} &:= \partial_\mu\tilde{W}_\nu - \partial_\nu\tilde{W}_\mu - ig[W_\mu, W_\nu],
\end{aligned}
$$

with $\tilde{W}_{\mu\nu} := \frac{\sigma_i}{2} W^i_{\mu\nu}$ and $W^i_{\mu\nu} = \partial_\mu W^i_\nu - \partial_\nu W^i_\mu + g\epsilon_{ijk} W^j_\mu W^k_\nu$. Under G transformations, $\tilde{W}_{\mu\nu}$ transforms covariantly, but $B_{\mu\nu}$ stays invariant. After proper normalization the kinetic Lagrangian is given by

$$\mathcal{L}_{kin} = -\frac{1}{4} B_{\mu\nu} B^{\mu\nu} - \frac{1}{2} \mathrm{tr}(\tilde{W}_{\mu\nu} \tilde{W}^{\mu\nu})) = -\frac{1}{4} B_{\mu\nu} B^{\mu\nu} - \frac{1}{4} W^i_{\mu\nu} W^{\mu\nu}_i. \qquad (2.15)$$

With the field strengths $W^i_{\mu\nu}$ having a quadratic term, $\mathcal{L}_{kin}$ contains terms for cubic and quartic self-interactions among the gauge fields. The strength is just the coupling g, as in the fermionic part of the Lagrangian.

Because of gauge symmetry, there is no mass term for the gauge bosons. Mass terms for fermions are not possible either, since they would allow communication between left- and right-handed fields, creating an explicit breaking of the gauge symmetry. So the Lagrangian only contains massless fields.

Interaction of Charged Currents

The Lagrangian given in equation (2.14) includes an interaction term of the fermion fields with the gauge bosons,

$$g\bar{\psi}_1 \gamma^\mu \tilde{W}_\mu \psi_1 + g' B_\mu \sum_{j=1}^{3} y_j \bar{\psi}_j \gamma^\mu \psi_j. \qquad (2.16)$$

Now the term containing $\tilde{W}_\mu$ gives rise to the charged-current interaction with the boson fields $W_\mu := (W^1_\mu + iW^2_\mu)/\sqrt{2}$ and $W^\dagger_\mu := (W^1_\mu - iW^2_\mu)/\sqrt{2}$. For one family of quarks and leptons the charged-current Lagrangian is

$$\mathcal{L}_{CC} = \frac{g}{2\sqrt{2}} \left(W^\dagger_\mu (\bar{u}\gamma^\mu(1-\gamma_5)d + \bar{\nu}_e \gamma^\mu(1-\gamma^5)e) + h.c. \right);$$

now the assumed gauge symmetry has the universality of the quark and lepton interactions as a direct consequence.

Interaction of Neutral Currents

In equation (2.16) there are terms representing interactions of the neutral gauge fields W^3_μ and B_μ. One would like to identify these fields with the Z boson and the photon γ. The photon cannot be identified with B_μ, since the photon has the same interaction with both fermion chiralities.

But one can make use of the fact that both fields are neutral by rotating them:

$$\begin{pmatrix} W^3_\mu \\ B_\mu \end{pmatrix} := \begin{pmatrix} \cos\Theta_W & \sin\Theta_W \\ -\sin\Theta_W & \cos\Theta_W \end{pmatrix} \begin{pmatrix} Z_\mu \\ A_\mu \end{pmatrix}.$$

	y_1	y_2	y_3
quarks	$\frac{1}{6}$	$\frac{2}{3}$	$-\frac{1}{3}$
leptons	$-\frac{1}{2}$	0	-1

Table 2.1: The hypercharges of quarks and leptons.

The mass of the Z boson will be discussed in subsection 2.1.4. When it comes to Z and γ, the neutral-current interaction is given by

$$\mathcal{L}_{NC} \;=\; \sum_j \bar{\psi}_j \gamma^\mu \left[A_\mu \left(g \frac{\sigma_3}{2} \sin \Theta_W + g' y_j \sin \Theta_W \right) + Z_\mu \left(g \frac{\sigma_3}{2} \cos \Theta_W - g' y_j \sin \Theta_W \right) \right] \psi_j.$$

The A_μ term in the Lagrangian gives QED, if the conditions

$$g \sin \Theta_W = g' \cos \Theta_W = e, \quad Y = Q - T_3 \tag{2.17}$$

are fulfilled; with

$$T_3 := \frac{\sigma_3}{2} \text{ and } Q_1 := \begin{pmatrix} Q_{u/\nu} & 0 \\ 0 & Q_{d/e} \end{pmatrix}, \; Q_2 = Q_{u/\nu}, \; Q_3 = Q_{d/e}.$$

The unification of electroweak interactions has been achieved, since the couplings of $SU(2)_L$ and $U(1)_Y$ are related to the electromagnetic coupling. Also, the fermion hypercharges (see Table 2.1) are given by their electric charges and weak isospins. A right-handed neutrino would have neither an electric charge nor a weak hypercharge, making it neutral to all interactions in our model.

Using equation (2.17), the neutral-current Lagrangian can be written in the following form:

$$\mathcal{L}_{NC} = \mathcal{L}_{QED} + \mathcal{L}_{NC}^Z.$$

$\mathcal{L}_{QED} = e A_\mu \sum_j \bar{\psi}_j \gamma^\mu q_j \psi_j =: e A_\mu J_{em}^\mu$ is the normal Lagrangian of QED, and

$$\mathcal{L}_{NC}^Z = \frac{e}{2 \sin \Theta_W \cos \Theta_W} J_Z^\mu Z_\mu$$

contains the interaction of Z with the neutral fermionic current

$$J_Z^\mu := J_3^\mu - 2 \sin^2 \Theta_W J_{em}^\mu.$$

It can also be given in terms of the fermion fields:

$$\mathcal{L}_{NC}^Z = \frac{e}{2 \sin \Theta_W \cos \Theta_W} Z_\mu \sum_f \bar{f} \gamma^\mu (v_f - a_f \gamma_5) f,$$

with $a_f = T_3^f$ and $v_f = T_3^f (1 - 4 |Q_f| \sin^2 \Theta_W)$.

The neutral-current couplings of the fermions are given in Table 2.2.

	u	d	ν_e	e
$2v_f$	$1 - \frac{8}{3}\sin^2\Theta_W$	$-1 + \frac{4}{3}\sin^2\Theta_W$	1	$-1 + 4\sin^2\Theta_W$
$2a_f$	1	-1	1	-1

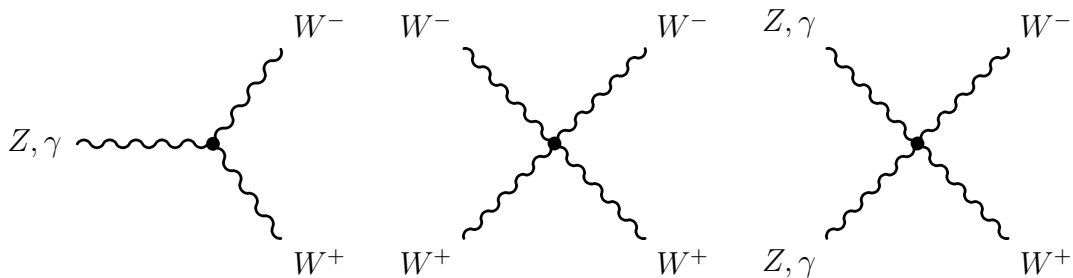Table 2.2: The neutral current couplings.

Figure 2.2: Self-interaction terms of the gauge bosons in electroweak interaction.

Self-Interactions among the Gauge Bosons

The kinetic Lagrangian (2.15) also contains cubic and quartic self-interaction terms among the gauge bosons (see Figure 2.2). There are no neutral vertices only with Z bosons and photons, since these are not generated by the $SU(2)_L$ algebra.

2.1.4   Higgs Mechanism

In the previous subsection, the electroweak unification has been derived under the assumption of massless gauge bosons, whereas $W^\pm$ and Z are heavy particles. Spontaneous symmetry breaking will be used in the following to introduce masses for the heavy gauge bosons.

A system is said to show spontaneous symmetry breaking, if the system is symmetric to a certain symmetry group, but also has a vacuum state that is not symmetric.

A very general and well-known result of symmetry breaking is the Goldstone theorem [Gold]:

- If a Lagrangian is invariant under a continuous symmetry group G, but the vacuum is only invariant under a subgroup $H \subset G$, then there must be as many massless spin-0 particles ('Goldstone bosons') as broken generators, i.e. generators of G which do not belong to H.

This theorem provides only massless bosons, but using local gauge symmetry, massive gauge bosons will be derived.

We start with an $SU(2)_L$ doublet of complex scalar fields

$$\phi(x) := \begin{pmatrix} \phi^{(+)}(x) \\ \phi^{(0)}(x) \end{pmatrix}$$

and the following Lagrangian :

$$\mathcal{L} = \partial_\mu \phi^\dagger \partial^\mu \phi - V(\phi), \quad V(\phi) = \mu^2 \phi^\dagger \phi + h(\phi^\dagger \phi)^2. \tag{2.18}$$

This leads to the scalar Lagrangian for our doublet:

$$\mathcal{L}_f = (D_\mu \phi)^\dagger D^\mu \phi - \mu^2 \phi^\dagger \phi - h(\phi^\dagger \phi)^2, \quad (h > 0, \mu^2 < 0),$$

$$D^\mu \phi = \left(\partial^\mu - ig\tilde{W}^\mu(x) - ig' y_\phi B^\mu \right) \phi, \quad y_\phi = Q_\phi - T_3 = \frac{1}{2}. \tag{2.19}$$

This Lagrangian is invariant under local $SU(2)_2 \otimes U(1)_Y$ transformations. The scalar hypercharge y_ϕ requires correct couplings between $\phi(x)$ and $A^\mu(x)$ and is fixed by this requirement; the photon does not couple to $\phi^{(0)}$.

The potential has an infinite number of degenerate states with minimum energy for $\mu^2 < 0$, fulfilling

$$\left| \langle 0 \left| \phi^{(0)} \right| 0 \rangle \right| = \sqrt{\frac{-\mu^2}{2h}} =: \frac{v}{\sqrt{2}}.$$

Thus the classical ground state is associated with the quantum vacuum. Only the neutral scalar field can acquire a vacuum expectation value, since the electric charge has to be conserved. By choosing a particular ground state, the symmetry of $SU(2)_L \otimes U(1)_Y$ gets broken to the electromagnetic subgroup $U(1)_{QED}$. The Goldstone theorem now requires 3 massless states.

Now we choose the parametrization

$$\phi(x) = \frac{1}{\sqrt{2}} e^{i\frac{\sigma_i}{2}\Theta_i(x)} \begin{pmatrix} 0 \\ v + H(x) \end{pmatrix}$$

of the scalar doublet, in which four real fields, $\Theta^i(x)$ and $H(x)$, are used. Because of the local $SU(2)_L$ invariance, the dependence on the angles, $\Theta_i(x)$, can be rotated away and the massless excitations become unphysical.

Taking the physical unitary gauge $\Theta^i(x) = 0$, the kinetic term of the scalar Lagrangian (2.18) has the following form:

$$(D_\mu \phi)^\dagger D^\mu \phi \overset{\Theta^i=0}{\rightarrow} \frac{1}{2}\partial_\mu H \partial^\mu H + (v + H)^2 \left\{ \frac{g^2}{4} W_\mu^\dagger W^\mu + \frac{g^2}{8\cos^2\Theta_W} Z_\mu Z^\mu \right\}.$$

So the vacuum expectation value of the neutral scalar has generated a quadratic term for the $W^\pm$ and the Z, thus giving mass to these gauge bosons and setting a relation between them:

$$M_Z \cos\Theta_W = M_W = \frac{1}{2}vg.$$

2.2 Properties of the W Boson and the Z Boson

The W boson and the Z boson were discovered in 1983 at the Super Proton Anti-Proton Synchrotron (Sp$\bar{\text{p}}$S) collider at CERN. Because of the great significance of their discovery, Carlo Rubbia and Simon van der Meer were awarded the Nobel Prize in physics in the following year.

2.2.1 W Mass and Width

Since its discovery, the measurement of the W mass properties has been significantly improved by the four LEP experiments and the two Tevatron experiments.

The latest W boson mass measurement was performed by the CDF collaboration [Aal] by applying template fits to transverse mass, transverse momentum and missing transverse energy for both electron decay channel and muon decay channel. These templates were calculated by fast Monte Carlo, taking physics and detector effects into account. The overall result is $M_W = 80413 \pm 34_{(stat)} \pm 34_{(syst)}$ MeV.

The Particle Data Group (PDG) world average for the W boson mass is 80.403 ± 0.029 GeV ([PDG]). The latest measurements are summarized in Figure 2.3.

For the W boson width, the PDG world average is 2.141 ± 0.041 GeV [PDG], the latest values given in Figure 2.4.

2.2.2 Z Mass and Width

The properties of the Z boson have been measured precisely by the four experiments at the LEP collider during the first run of the collider (1989-1995); thus world averages for mass and width in [PDG] are only calculated from the LEP-I data. The mass values of the four LEP experiments are given in Figure 2.5, together with the overall LEP value of 91.1875 ± 0.0021 GeV. The respective information on the Z width is given in Figure 2.6, with the world average being 2.4952 ± 0.0023 GeV.

2.3 Correlation between W Boson Mass, Top Quark Mass and Higgs Boson Mass

Taking into account 1-loop corrections (see Figure 2.7), the W mass can be written as

$$m_W^2 = \frac{\frac{\pi\alpha}{\sqrt{2}G_F}}{\sin^2\Theta_W(1-\Delta r)},$$

with $\sin^2\Theta_W := 1 - \frac{m_W^2}{m_Z^2}$, α being the fine structure constant and G_F being the Fermi coupling constant; Δr represents 1-loop corrections.
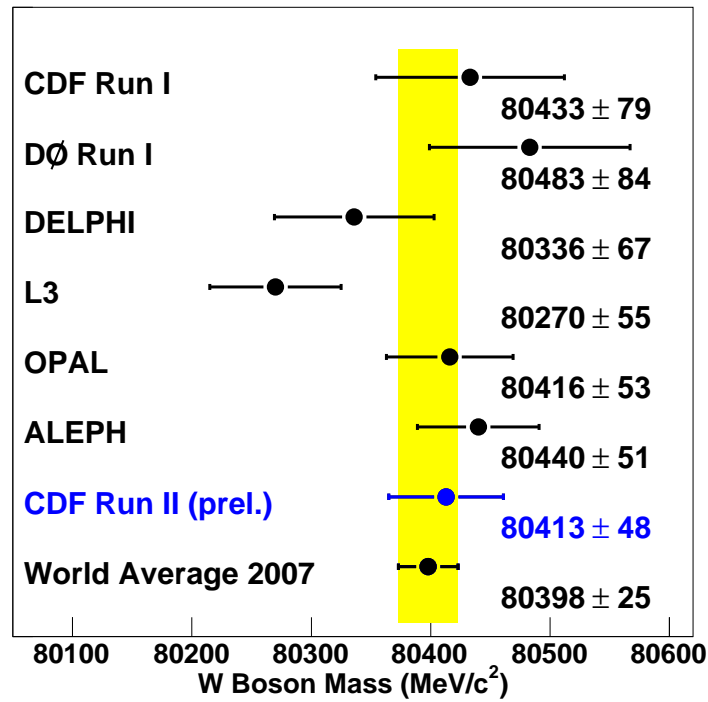
Figure 2.3: The W mass measured by the LEP and by the Tevatron experiments and the resulting combined value. [CDFEW]
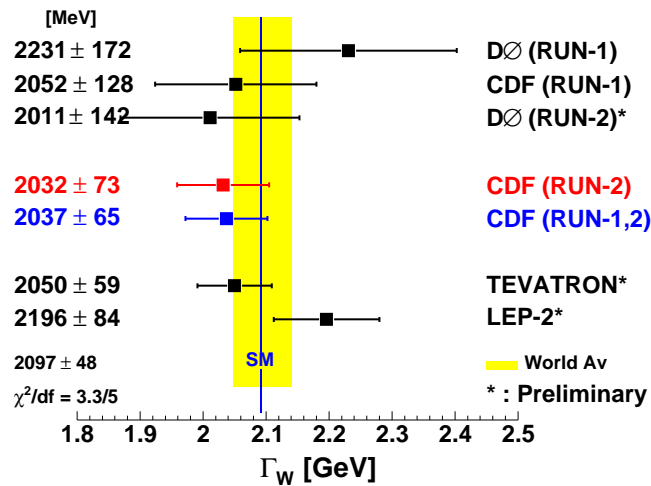

Figure 2.4: The W width measured by the LEP and by the Tevatron experiments and the combined value [CDFEW].
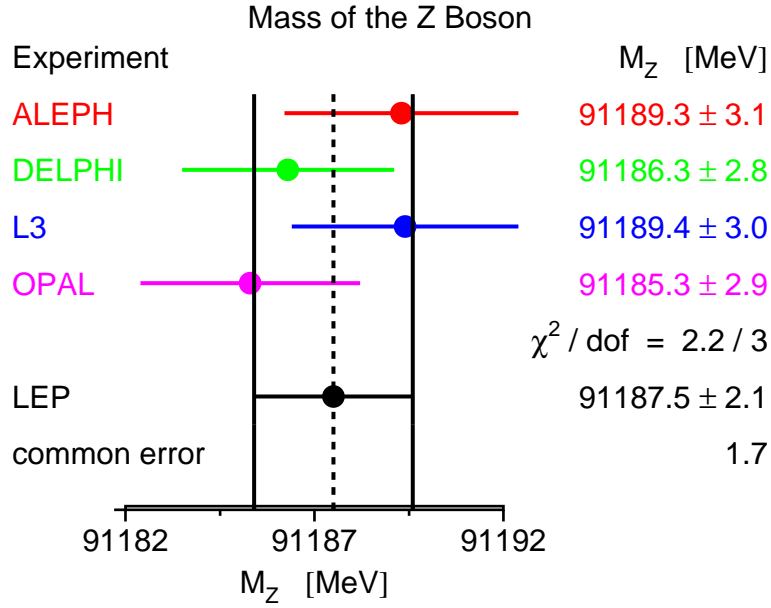
Figure 2.5: The Z boson mass measured by the LEP experiments [LEPEWWG].

Main contributions to the 1-loop corrections come from the top quark and the
Higgs boson (see Figure 2.7) because of their masses; they are [Wil]

$$(\Delta r)_{\text{top}} \approx -\frac{3\ G_F m_t^2}{8\sqrt{2}\pi^2} \frac{1}{\tan^2 \Theta_W}$$

and

$$(\Delta r)_{\text{Higgs}} \approx \frac{11 G_F M_Z^2 \cos^2 \Theta_W}{24\sqrt{2}\pi^2} \ln \frac{m_h^2}{m_Z^2},$$

where m_t is the top quark mass and m_H is the Higgs boson mass.

In Figure 2.8, the results of the indirect measurement of the W boson mass and
the top quark mass via radiative corrections at LEP1 and SLD are shown together
with the results of the direct measurement by LEP2 and the Tevatron experiments.
In addition, the Standard Model relationship for the masses as a function of the Higgs
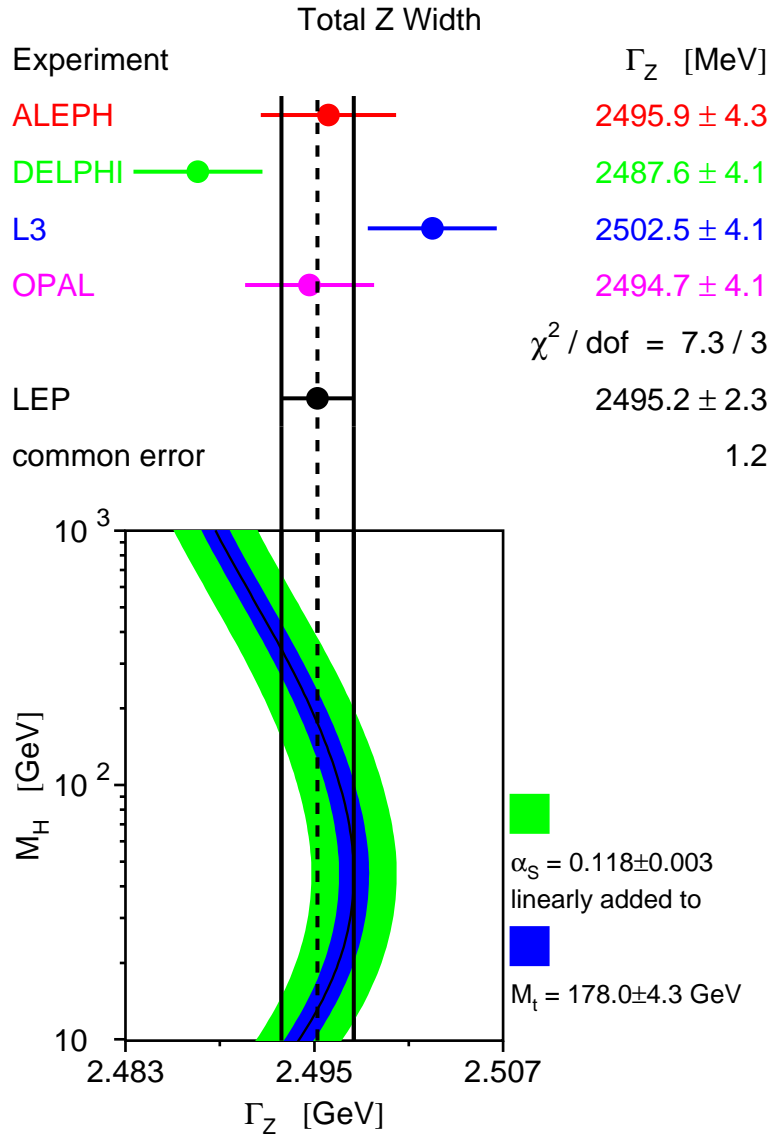boson mass is presented in this figure.

Figure 2.6: The Z width measured by the LEP experiments and the overall LEP value. The lower part shows the SM prediction for the Higgs mass depending on the Z width. [LEPEWWG].
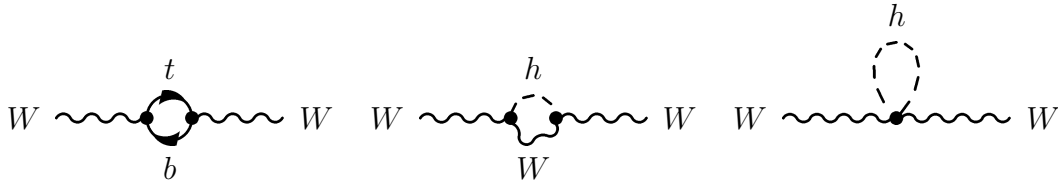
Figure 2.7: The Feynman diagrams for the most important 1-loop corrections to the W propagator.
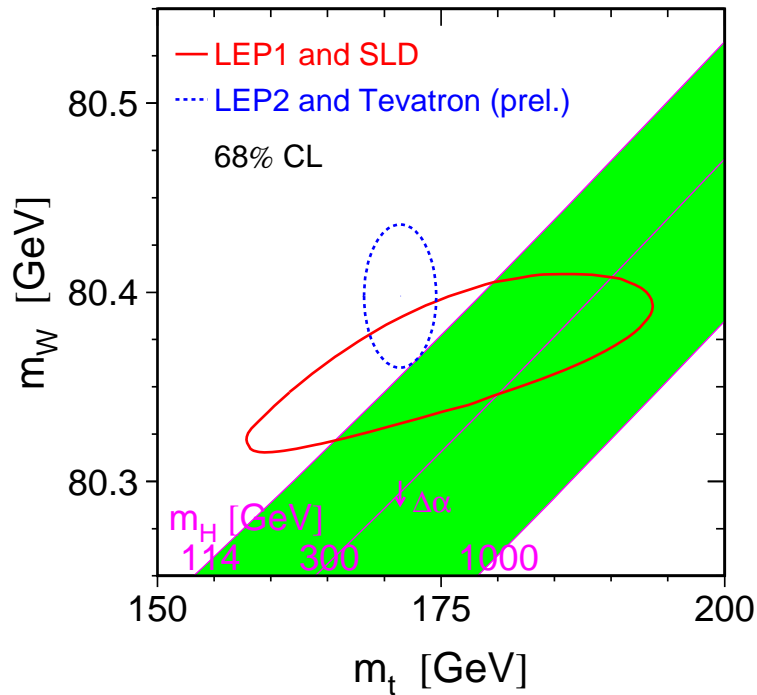
Figure 2.8: The red, solid contour shows the 68% confidence level for the W boson mass and the top quark mass acquired from indirect measurement by the LEP1 experiments and by SLD. For comparison, the blue, dashed contour represents the direct measurement by the Tevatron experiments and by the LEP2 experiments. The green band shows the Standard Model relationship for the masses as a function of the Higgs mass. The arrow labeled with $\Delta\alpha$ shows the shift of this band when $\alpha(m_Z)^2$ is shifted by one standard deviation. [LEPEWWG]

Figure 2.9: The Feynman diagram for the lowest order of the Drell-Yan process $u\bar{d} \rightarrow W^+ \rightarrow l^+\nu_l$.

2.4   Theory of W- and Z-Production at LHC

2.4.1   W Boson Production

At hadron colliders, the most important production process for electroweak gauge bosons is the annihilation of $q\bar{q}$ pairs; this so-called Drell-Yan process has a large cross section. At the Tevatron, both quark and anti-quark are in most cases valence quarks, while at the LHC the anti-quark is a sea quark.
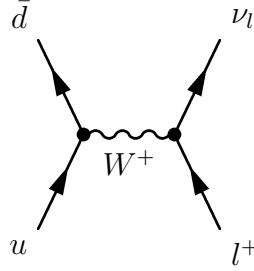
The lowest order Feynman diagram for the Drell-Yan production of W bosons (which then decay leptonically) is given in Figure 2.9. Only this Feynman graph contributes to the scattering amplitude of the process $u\bar{d} \rightarrow l\nu_l$ at the lowest order [Hay]:

$$\mathcal{M}_0 = \frac{e^2 V_{ud}^*}{2s_W^2} \left[\bar{u}_d \gamma^\nu P_L - u_u\right] \frac{1}{\hat{s} - M_W^2 + iM_W \Gamma_W(\hat{s})} \left[\bar{u}_{\nu_l} \gamma^\mu P_L - \nu_l\right].$$

Here $P_L = \frac{1}{2}(1 + \gamma^5)$ is the left-handed chirality projection-operator, u and d the up-type and down-type quarks (up and charm or down and strange, respectively). $\hat{s}$ denotes the center-of-mass-energy. s_W^2 is related to the weak mixing angle by $s_W^2 = 1 - \cos^2\Theta_W$.

This matrix element is used to calculate the differential cross section

$$\left(\frac{d\hat{\sigma}_0}{d\hat{\Omega}}\right) = \frac{1}{12}\frac{1}{64\pi^2\hat{s}}|\mathcal{M}_0|^2 = \frac{\alpha^2|V_{ud}|^2}{192s_w^4\hat{s}}\frac{\hat{u}^2}{|\hat{s} - M_W^2 + iM_W\Gamma_W(\hat{s})|^2}. \qquad (2.20)$$

In this formula, the variable $\hat{u}$ is defined as the squared momentum difference between the up-type quark and the lepton; this variable shows the angular dependency of the differential cross section:

$$\hat{u} = (p_u - p_l)^2 \sim 1 + \cos\Theta. \qquad (2.21)$$

The factor $\frac{1}{12}$ in (2.20) is a result of averaging over colors (three colors and three anti-colors) and quark spins (spin up and spin down). The angle between the up-type
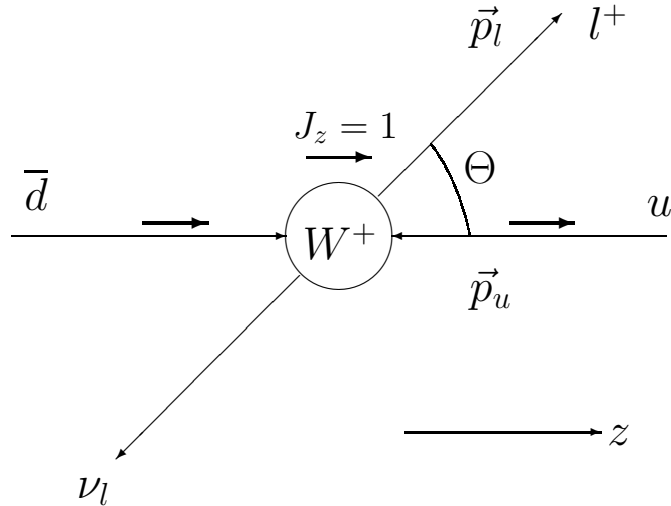
Figure 2.10: Kinematics of the process depicted in Figure 2.9. The W boson couples only to right-handed fermions; therefore, it is polarized.

quark and the outgoing lepton is represented by Θ. The value of α changes according to the energy scale; therefore, one calls $\alpha(Q^2)$ a running coupling constant. For low energies, α can be identified with the fine structure constant $\alpha(0)$. Equation (2.21) shows an angular dependency, which is due to the fact that the electroweak current couples only to left-handed fermions; thus polarized W^+ bosons are produced. The kinematics is depicted in Figure 2.10.

From helicity conservation and angular momentum conservation one can derive that a $J_Z = 1$ state decays with an amplitude proportional to $(1 + \cos\Theta)^2$; the angle Θ is the angle between the outgoing charged lepton and the beam axis in the Collins-Soper frame [ColSop]. The following steps have to be realized to transform from the laboratory frame to the Collins-Soper frame:

1. The system is Lorentz-boosted along the beam axis, which is defined as z-axis, so that the W boson will be in rest with respect to the beam axis.

2. Now the system is rotated in such a way that the transverse momentum of the W boson is aligned perpendicular to the x-axis.

3. Finally, the system is Lorentz-boosted along the x-axis, so that the W boson is at rest.

Integrating in (2.20) over the azimuthal angle φ and taking equation (2.21) into account, the differential cross section is

$$\left(\frac{d\hat{\sigma}_0}{d(\cos\Theta)}\right) = \frac{\pi\alpha^2|V_{ud}|^2}{24s_w^4}\frac{\hat{s}^2}{\left|\hat{s}-M_W^2+iM_W\Gamma_W(\hat{s})\right|^2}(1+\cos\Theta)^2. \qquad (2.22)$$

The asymmetry on Θ can be explained by the matrix element used for the derivation; the calculation starts with a quark from one proton and an anti-quark from the other proton. The process with quark and anti-quark interchanged can be taken into account by symmetrizing equation (2.22) via

$$\left(\frac{d\hat{\sigma}_0}{d(\cos\Theta)}\right) \sim (1+\cos\Theta)^2 + (1-\cos\Theta)^2.$$

Until now, only fusion of up and (anti-)down quarks was taken into account. But W boson production processes can also include a charm and/or a strange quark. The flavor decomposition of W cross sections is given in Figure 2.11; about 20% of the total cross section for LHC is contributed by the strange-charm scattering, with the cross sections of W^+ and W^- differing. For a $p\bar{p}$ collider like Tevatron, the cross sections for W^+ and W^- are of course the same for symmetry reasons.

Still, virtual 1-loop corrections and real-photonic bremsstrahlung effects on the cross section have not yet been considered. In [Hay], first order corrections of the lowest order cross section are discussed in detail.

Another effect that needs to be taken into account is the transverse momentum range of 0 GeV to about 100 GeV of the W boson; this is not described by leading order calculations. It stems from quark or gluon radiation in the initial state, altering the helicity of the W boson. In next-to-leading order QCD calculations the angular distribution can be given as

$$\frac{\mathrm{d}\sigma}{\mathrm{d}(\cos\theta)} \sim 1 + \alpha_1\cdot\cos\theta + \alpha_2\cdot\cos^2\theta,$$

with α_1 and α_2 being functions of the transverse momentum, P_T, of the boson [MirOhn].

After the inclusion of NNLO (next to next to leading order) corrections, the differential cross section is 20.3 ± 1.0 nb [Hay] (the lowest order calculation yields 17.9 nb).

2.4.2 Z Boson Production

While the W boson production (described in section 2.4.1) has a pure V-A structure, the Z boson also couples to right-handed components; therefore, there are interferences with the photon.

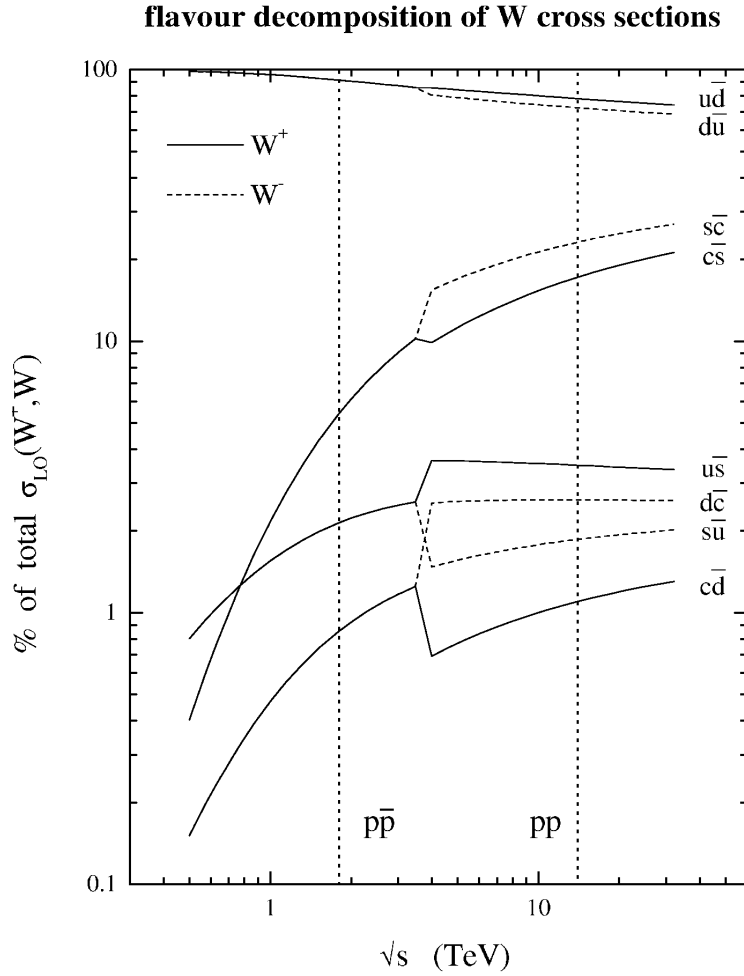**flavour decomposition of W cross sections**

Figure 2.11: Flavor decomposition for the W^+ and the W^- boson. In the range of $\sqrt{s} < 4$ GeV, the parton decomposition is given for $p\bar{p}$ colliders. For $\sqrt{s} > 4$ GeV, the parton decomposition is given for pp colliders; the solid line represents the decomposition for W^+ bosons, the dashed line shows the decomposition for W^- bosons. [Mart]

Starting with the lowest order process, the amplitude for quark anti-quark fusion is described by the exchange of a Z boson and a photon, respectively [Hay]:

$$q\bar{q} \rightarrow Z^0/\gamma^* \rightarrow l^+l^-. \tag{2.23}$$

In the effective Born approximation the cross section for (2.23) is derived as [Hay]

$$\frac{\mathrm{d}\hat{\sigma}}{\mathrm{d}\Omega} = \frac{1}{64\pi^2\hat{s}} \left[\mathcal{A}_0 \cdot (1 + \cos^2\theta) + \mathcal{A}_1 \cdot \cos\theta \right], \tag{2.24}$$

with θ being the scattering angle in the parton center-of-mass system. $\mathcal{A}_0$ and $\mathcal{A}_1$ are functions containing different higher order calculations, e.g. the effective electromagnetic charge taking the photon vacuum polarization into account; the Z propagator, the overall normalization factor, the neutral-current and the vector axial-vector coupling constants are included. The latter one is sensitive to the effective mixing angle.

For the cross section in equation (2.24), one can derive a forward-backward asymmetry, which can be expressed at parton level as

$$\hat{A}_{FB} = \frac{\hat{\sigma} - \hat{\sigma}_B}{\hat{\sigma} + \hat{\sigma}_B} = \frac{3}{8}\frac{\mathcal{A}_1}{\mathcal{A}_0}.$$

This quantity is sensitively dependent on the square of the effective mixing angle around the Z peak, therefore it is especially qualified for high precision measurements of this electroweak parameter.

Using only electroweak calculations, the lowest order cross section for the Z boson production at the LHC is 1.71 nb.

Taking also NNLO QCD calculations into account, the cross section rises to $1.87 \pm 0.0.9$ nb. The flavor decomposition is given in Figure 2.12.

2.5   Transverse Mass and Jacobian Edge

Neutrinos are not directly detectable in a high energy physics experiment, they do not interact with the detector material. Therefore, their kinematics are indirectly acquired via the missing energy in an event. At hadron colliders it is also impossible to measure the z-component of the missing energy, since the z-components of the initial quark and gluon momenta are unknown and since the proton remnants usually do not pass the acceptance region of the detector. So only the missing transverse energy, E^T_{miss}, can be accessed. The discussion of the transverse mass in this section mainly follows [Gor].

Therefore, a new quantity for W boson decays, the transverse energy E^T,

$$E^T = \frac{\sqrt{\hat{s}}}{2}\sin\Theta,$$

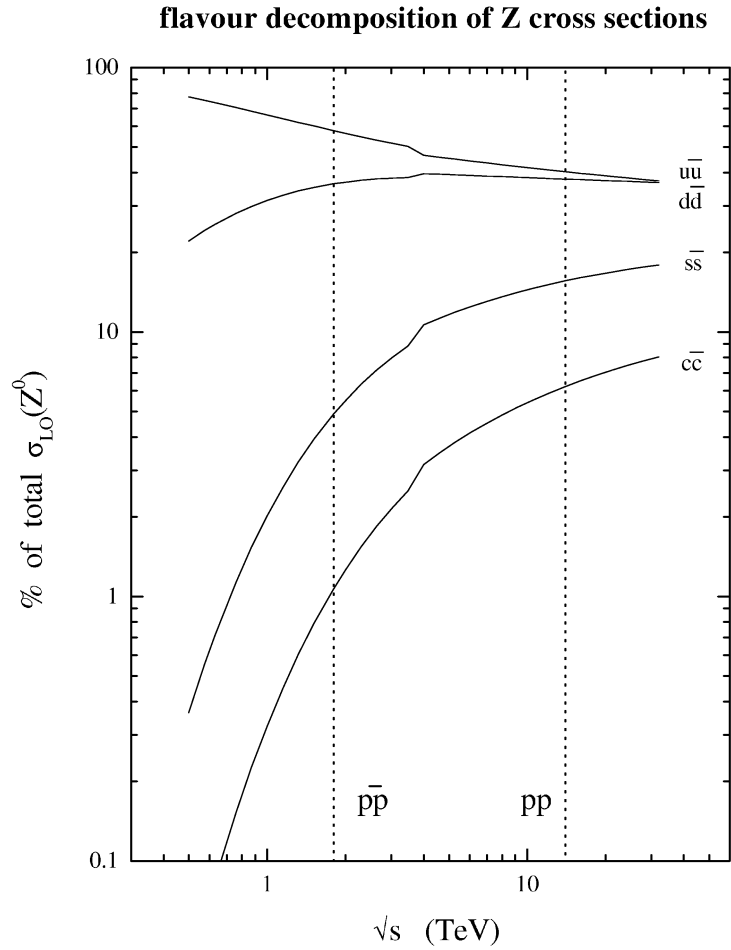**flavour decomposition of Z cross sections**

Figure 2.12: Flavor decomposition for the Z^0 boson. In the range of $\sqrt{s} < 4$ GeV, the parton decomposition is given for $p\bar{p}$ colliders. For $\sqrt{s} > 4$ GeV, the parton decomposition is given for pp colliders. Different contributions are displayed as the percentage of the total cross section at leading order. [Mart]

is defined; it is related to the center-of-mass energy and the scattering angle. One can now state the differential cross section with respect to the transverse energy:

$$\frac{d\sigma}{dE^T} = \frac{2}{\sqrt{\hat{s}}}\frac{d\sigma}{d(\sin\Theta)} = \frac{2}{\sqrt{\hat{s}}}\frac{\sin\Theta}{\cos\Theta}\frac{d\sigma}{d(\cos\theta)}.$$

Incorporating the lowest order differential cross section for W boson production,

$$\frac{d\sigma}{d(\cos\Theta)} = \sigma_0(\hat{s})(1 + \cos\Theta)^2,$$

the differential cross section can be given in the form

$$\frac{d\sigma}{dE^T} = \sigma_0(\hat{s})\frac{4E^T}{\hat{s}}\left(2 - \frac{4(E^T)^2}{\hat{s}} + 2\sqrt{1 - 4(E^T)^2/\hat{s}}\right)\frac{1}{\sqrt{1 - 4(E^T)^2/\hat{s}}}. \qquad (2.25)$$

Since E^T and $\hat{s}$ are invariant under Lorentz-transformations along the z axis, this differential cross section is independent of the longitudinal component of the W boson momentum. The singularity at $E^T = \sqrt{\hat{s}}/2$ is referred to as Jacobian edge.

The transverse mass of the W boson is given by

$$m_T = \sqrt{(E_l^T + E_\nu^T)^2 - (\vec{P_l^T} + \vec{P_\nu^T})^2} \approx \sqrt{(E_l^T + E_\nu^T)^2 - (\vec{E_l^T} + \vec{E_\nu^T})^2}. \qquad (2.26)$$

Expanding (2.26) in P_W^T/E_l^T shows the dependence of the transverse mass on the transverse momentum in first order. The transverse mass distribution also has a Jacobian edge (see Figure 2.13). Since m_T is only dependent on the transverse components of the final states, it can be written as

$$m_T = \sqrt{2E_l^T E_\nu^T (1 - \cos\Delta\Phi)}, \qquad (2.27)$$

with $\Delta\Phi$ being the azimuthal angle between the charged lepton and the neutrino. The position and the shape of the Jacobian edge depend on the mass and the width of the W boson.
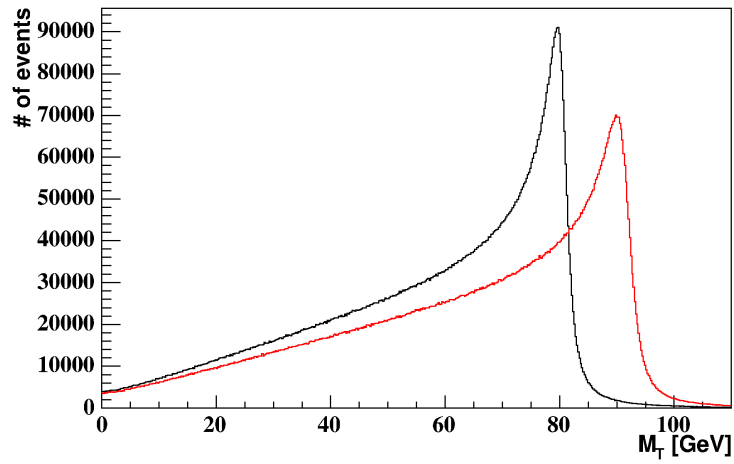
Figure 2.13: These transverse mass distributions of W and Z boson have been calculated from 10 million Monte Carlo generator level events for each boson. Both have their Jacobian edge around their respective mass, the shapes are slightly different because of their different widths. (taken from [Bue2])

Chapter 3

The Large Hadron Collider and the CMS Detector

The $\underline{L}$arge $\underline{H}$adron $\underline{C}$ollider (LHC, see Figure 3.1) is used mainly as a proton-proton collider, currently nearing its completion at CERN (Organisation Européenne pour la Recherche Nucléaire, formerly called $\underline{C}$onseil $\underline{E}$uropéen pour la $\underline{R}$echerche $\underline{N}$ucléaire) near Geneva, Switzerland. It is being installed in the former LEP ($\underline{L}$arge $\underline{E}$lectron $\underline{P}$ositron Collider) tunnel, which has a circumference of about 27 km.

Preceding hadron colliders, like the Super Proton Anti-Proton Synchrotron (Sp$\bar{\text{p}}$S) and the Tevatron, had landmark achievements, e.g. the discovery of the intermediate gauge bosons, W and Z, and of the top quark, respectively. The LHC has been designed to find the reason for the electroweak symmetry breaking and might discover physics beyond the Standard Model.

3.1 The Large Hadron Collider

Main properties of the LHC and its experiments will be described in the following subsections.

3.1.1 Accelerator and Collider

The LHC has a record center-of-mass energy of 14 TeV, which exceeds the center-of-mass energy of 1.96 TeV of the Tevatron collider at $\underline{F}$ermi $\underline{N}$ational $\underline{A}$ccelerator $\underline{L}$aboratory (FNAL, located in Batavia, Illinois, USA) by nearly one order of magnitude.

There will be about $3,000$ bunches of approximately 10^{11} protons in the collider ring. These bunches will be kept on track by magnetic fields of 8 Tesla and will collide at the four interaction points at a frequency of 40 MHz.
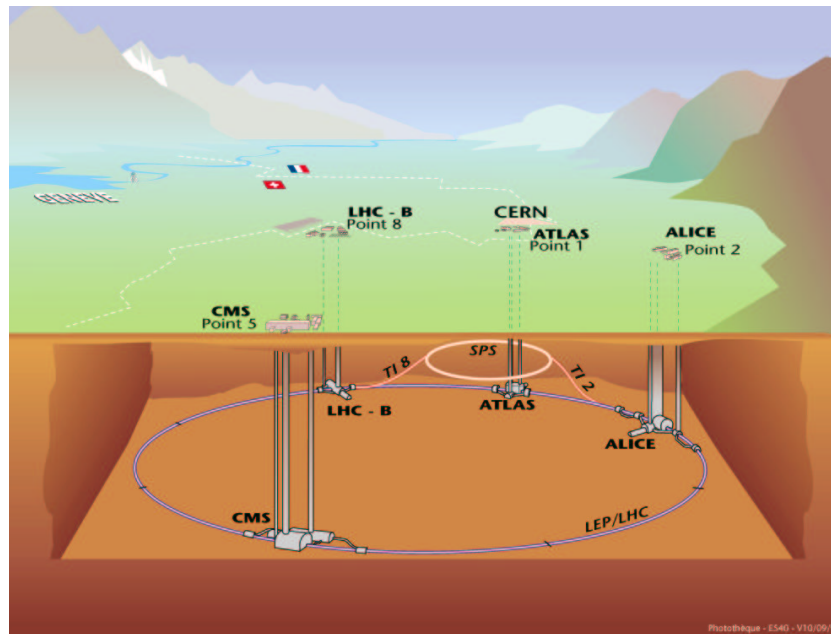
Figure 3.1: This schematic view of the LHC shows the four experiments at their respective interaction points and the pre-accelerator SPS. The LHC ring crosses the French-Swiss border in four places. [CMSO]

In the first three years of data taking, a luminosity of $\mathcal{L}_{low} = 2 \cdot 10^{33} \mathrm{cm}^{-2} \ \mathrm{s}^{-1}$ is expected to be achieved; this is often referred to as the *low luminosity phase*. After three years, the accelerators and the detectors will be upgraded and the design luminosity, also called *high luminosity*, of $\mathcal{L}_{high} = 10^{34} \ \mathrm{cm}^{-2}\mathrm{s}^{-1}$ will be reached.

In order to focus and to bend the proton beams, strong magnetic fields (up to 8.36 T) are used for the $1,232$ dipole magnets; these magnets are new types of superconducting niobium-titanium magnets, operating at liquid helium temperature (approximately 1.9 K).

3.1.2   LHC Experiments

There will be four experiments:

- **ATLAS** (A Toroidal LHC ApparatuS) and **CMS** (Compact Muon Solenoid):
  Both experiments are multi-purpose experiments; their main objectives are Standard Model measurements (e.g. Higgs boson, top quark mass, W boson mass, QCD in multi-jet events) and the search for physics beyond the Standard Model. A more precise description of the CMS detector will be given in section 3.2.

- **LHCb** (LHC beauty experiment):
  This experiment is a single-arm spectrometer and has been specifically designed for the study of b-physics; it has been designed to maximize the B meson acceptance. LHCb will measure CP violation and will perform precision measurements of the mixing parameters.

- **ALICE** (A Large Ion Collider Experiment):
  This detector has not been designed for measurements during pp runs, but for measurements during heavy ion runs; in Pb-Pb collisions, the nucleon-nucleon center-of-mass energy will reach 5.5 TeV (currently the world's highest nucleon collision energy is 200 GeV at RHIC (Relativistic Heavy Ion Collider) at the Brookhaven Laboratory in Upton, New York, USA). ALICE will measure the properties of quark-gluon plasma, which is believed to have existed in the first 30 microseconds after the Big Bang.

3.2   The Compact Muon Solenoid

The CMS detector is a multi-purpose detector (see Figure 3.2), which is the joint effort of an international collaboration consisting of about $2,700$ scientists and engineers from about 185 institutions in approximately 40 countries. Its name is derived from its compactness (mass of $12,500$ t, length of 21.5 m, diameter of 15 m), its optimization for tracking muons and its powerful solenoid magnet.

It consists of a main part called barrel and two endcaps, in which different subdetectors are installed.

3.2.1   The Tracking System

The tracking system is the innermost part of the CMS detector; it has two components, the silicon pixel detector and the silicon strip detector (see Figures 3.3 and 3.4), providing precise position measurements of charged particles.

The barrel consists of three pixel layers and silicon strip layers. Each endcap comprises two pixel layers, three inner and nine outer forward disks of silicon strip detectors. The tracking system has a total length of approximately 5.4 m, an inner radius of 0.2 m, and an outer radius of approximately 1.1 m.

The silicon pixel detectors cover pseudo-rapidities of $|\eta| < 2.5$, while the silicon strip detectors cover $|\eta| < 2.4$.

With its high position resolution of about $\approx 15~\mu$m, the pixel detector offers a very precise impact parameter determination and a very good vertex reconstruction; the vertex reconstruction is important for the measurement of secondary vertices of long-lived particles.

The active area of 170 m^2 of the whole silicon strip detector is being read out by about $10,000,000$ channels. The read out process is performed by a charge sensitive amplifier.

3.2.2   Calorimeters

Electromagnetic Calorimeter

The tracker is enclosed in the <u>E</u>lectromagnetic <u>C</u>alorimeter (ECAL, see Figure 3.5). It measures the energies of photons, electrons and positrons with high precision. Up to a range of $|\eta| = 3.0$, these particles, which travel at relativistic speeds, are stopped in the absorber material of the ECAL. They start electromagnetic showers in the crystals by bremsstrahlung, photo effect, Compton effect, and pair production. The resulting fluorescence light is a direct measure for the energy; it is measured by vacuum phototriodes in the endcaps and avalanche diodes in the barrel.

A detailed description of the ECAL is given in [ETDR].

The ECAL consists of about $80,000$ lead-tungstate (PbWO$_4$) crystals, which were chosen as the absorber material because of the following properties.

- Their high density of 8.28 $\frac{\text{g}}{\text{cm}^3}$ and the resulting small radiation length of $X_0 = 0.89$ cm; the length of a crystal of approximately 23 cm corresponds to about 26 X_0, therefore even high energy particles deposit almost all of their energy in the electromagnetic calorimeter.
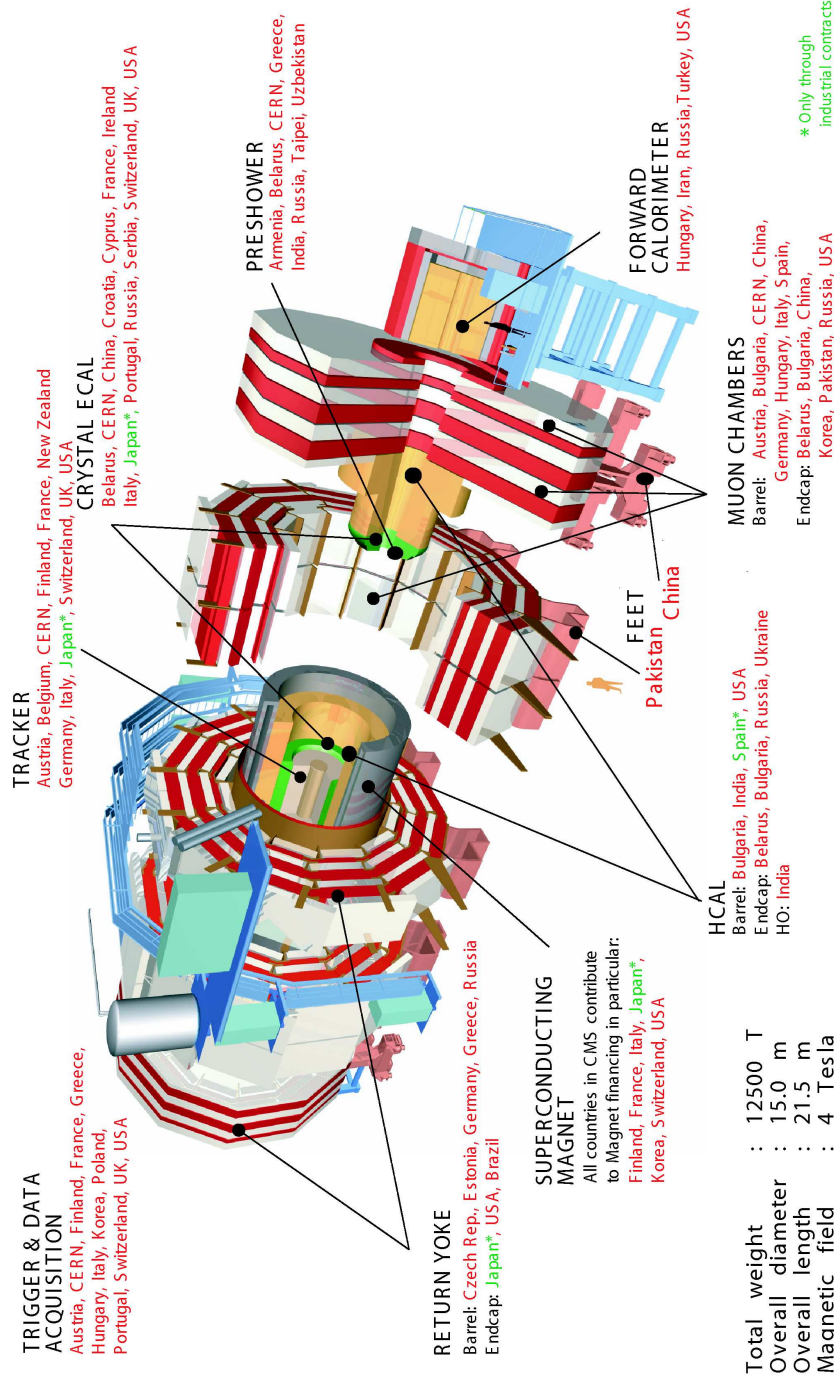
Figure 3.2: Overview of the subdetectors of the CMS detector with information on contributing countries. [CMSO]
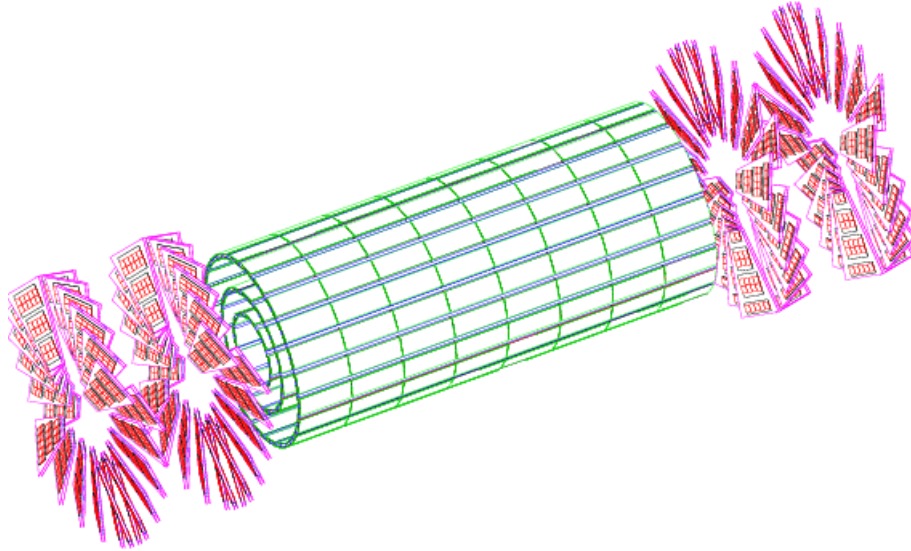
Figure 3.3: Layout of the CMS pixel detectors, consisting of 3 barrel layers with 2 endcap disks (taken from [PTDR1]).
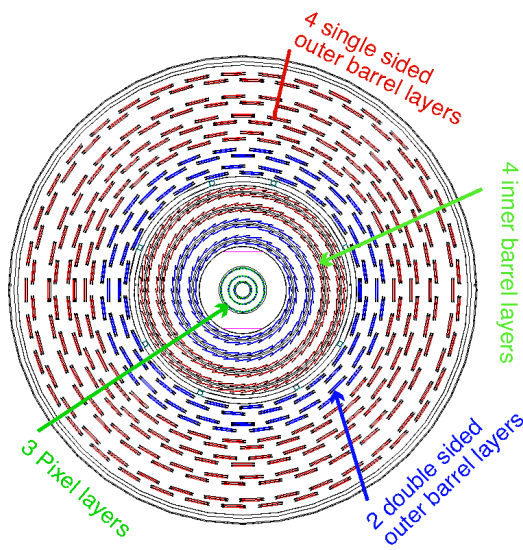

Figure 3.4: The profile shows the pixel layers and the silicon strip layers in the CMS barrel; in both inner and outer barrel the two innermost layers are double-sided (taken from [CO1]).
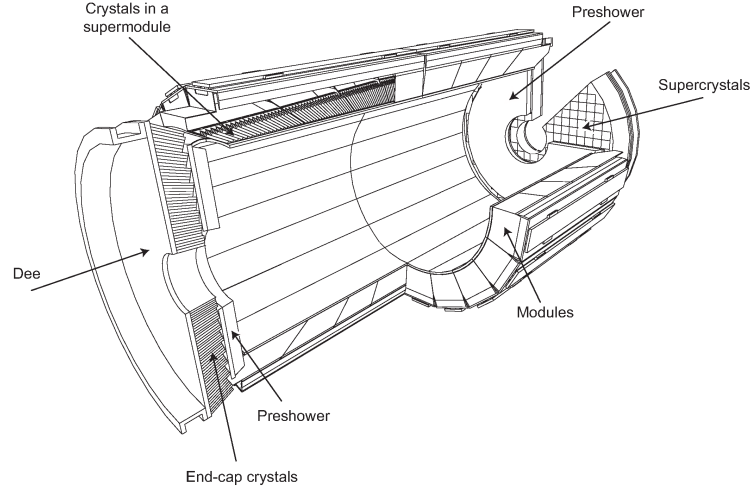
Figure 3.5: Schematic view of the electromagnetic calorimeter of the CMS detector. The ECAL measures the energies of photons, electrons and positrons. [CMS]

- The short Molière radius of 2.2 cm.

- Their ability to be used simultaneously as scintillators. The scintillating process is fast: within 20 ns, 80% of the light is emitted. This is important, since the bunch crossing time of LHC is 25 ns.

- Their radiation hardness of up to 10 Mrad.

The ECAL has a lateral granularity of $\Delta\eta \times \Delta\varphi = 0.0175 \times 0.0175$. The design energy resolution σ_E is parametrized via

$$\left(\frac{\sigma_E}{E}\right)^2 = \left(\frac{a}{\sqrt{E}}\right)^2 \oplus \left(\frac{b}{E}\right)^2 \oplus c.$$

The stochastic term a considers the fluctuation in the shower containment; it is 2.7% for the barrel and 5.0% for the endcaps. The noise contribution from readout electronics and pileup energy is summarized in term b and has a value from 205 to 245 MeV for the barrel and from 150 to 210 MeV for the endcaps, depending on the luminosity. The constant c includes contributions from inter-calibration errors, shower leakage and crystal uniformities.

Hadronic Calorimeter

After losing only a small fraction of their energy in the ECAL due to their long radiation length, hadrons are stopped in the Hadronic Calorimeter (HCAL). The hadrons

Figure 3.6: An HCAL half barrel in the assembly hall. [PTDR1]

cause hadronic showers due to interactions with the nuclei of the calorimeter material. Both ECAL and HCAL are jointly used to determine the energy of the hadrons.

The CMS HCAL (see Figure 3.6) is a copper alloy calorimeter covering the $|\eta|$ range up to 3.0. Copper absorber plates are 5 cm thick and are interleaved with plastic scintillators and wavelength shifting optical fibers. The HCAL consists of a barrel part ($|\eta| < 1.3$), two endcaps ($1.3 < |\eta| < 3$), and the Very Forward Calorimeters (VFCAL) at both ends of the detectors, which increase the pseudo-rapidity range up to $|\eta| < 5.0$.

The HCAL measures the energy and the direction of the jets, from which the quarks and gluons can be reconstructed. Since neutrinos do not interact with the detector, the calorimeters measure them via the missing transverse energy.

Figure 3.7: The yoke of the CMS detector at an early stage of magnet assembly. [CMS]

3.2.3   The Magnet System

One of the most prominent features of the CMS detector is its magnet, which is the largest super-conducting solenoid in the world. It surrounds the calorimeters and the tracker. The solenoid is 13 m long and 5.9 m in diameter; its mass is about 500 t. All charged particles are bent by the magnetic field of 4 T within the solenoid. The return yoke (see Figure 3.7) is 1.5 m thick and has a mass of $7,000$ t. Inside of it, the magnetic field strength is 2 T. At full current, the stored energy in the magnetic field is 2.66 GJ.

3.2.4   The Muon Chambers

The muon system consists of four muon stations interleaved with the return iron yoke plates of the magnet; these plates can only be traversed by muons and neutrinos; the total thickness of the absorber in front of the last muon station is about 16 interaction lengths. Three types of detectors are used for detecting and measuring the muons (see Figure 3.8):

- $\underline{d}$rift $\underline{t}$ubes (DT) in the barrel region ($|\eta| < 1.2$),

- $\underline{c}$athode $\underline{s}$trip $\underline{c}$hambers (CSC) in the endcap region ($0.9 < |\eta| < 2.4$),
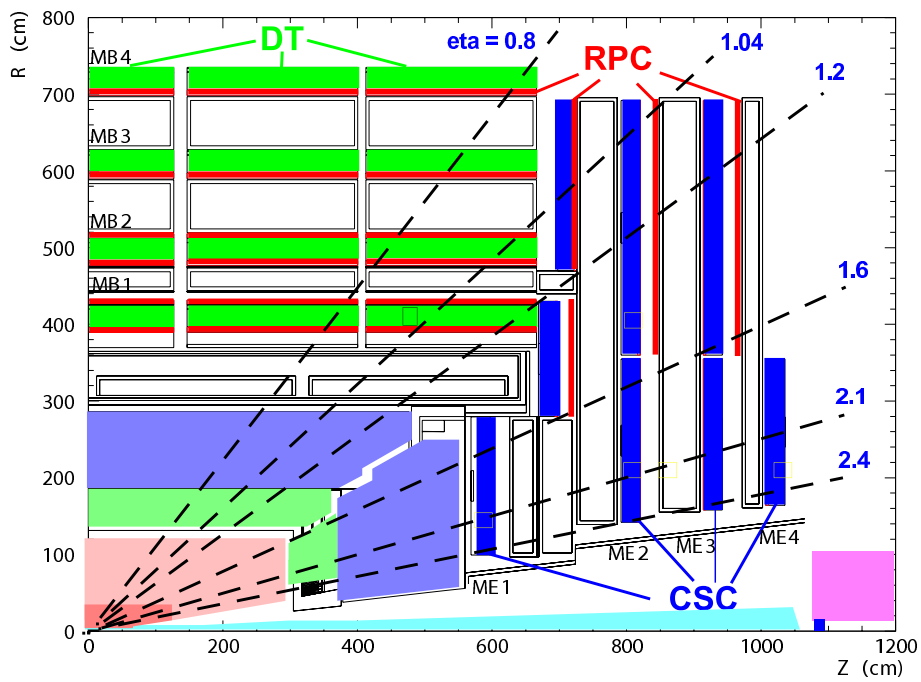
Figure 3.8: Sketch of the CMS muon system for one quarter of the detector: drift tubes (DT) in the barrel region, resistive plate chambers (RPC) in the barrel and the endcap region and cathode strip chambers (CSC) in the endcap region (taken from [PTDR1]).
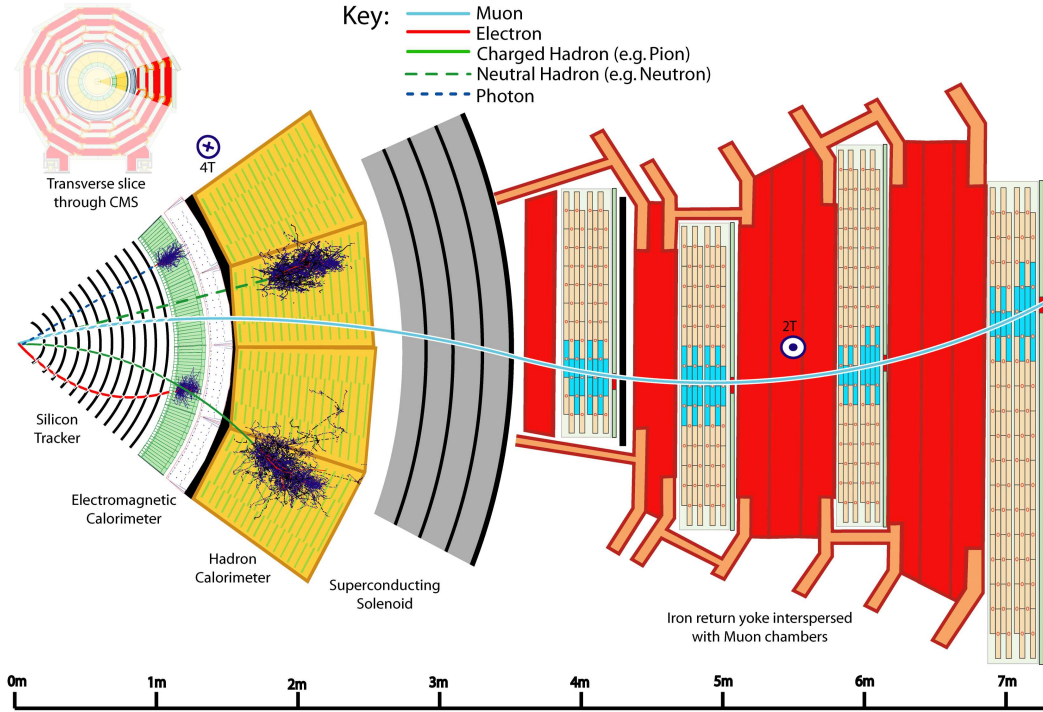
Figure 3.9: This section through the CMS detector shows tracks of different particles. Electrons and photons deposit their energy in the electromagnetic calorimeter and are stopped; electrons also leave tracks in the silicon tracker. Hadrons pass through the ECAL losing only a small fraction of energy, but are stopped in the hadronic calorimeter. Muons pass both ECAL and HCAL and are finally detected in the muon chambers. [CO2]

- resistive plate chambers (RPC) in both the barrel and the endcap regions ($|\eta| <$ 1.6).

The RPCs are very fast (time resolution $\approx$ 2-3 ns) and will be used for the first level trigger system (see subsection 3.2.5), but have a low spatial resolution. DTs and CSCs offer high precision measurements of position and momentum, which can be improved by using tracker information. The full muon system covers pseudo-rapidities up to $|\eta < 2.4|$, with the range of $|\eta < 2.1|$ used for triggering.

The trajectories and the energy deposits of particles with different detector components are graphically summarized in Figure 3.9.

3.2.5   Triggering and Data Acquisition

At the LHC, the crossing frequency of the proton bunches will be 40 MHz. In the low luminosity phase, $\mathcal{L}_{low}$, there will be approximately five inelastic collisions on average per bunch crossing; this number corresponds to $160,000,000$ inelastic collisions per second. In the high luminosity phase, $\mathcal{L}_{high}$, the average number of inelastic collisions per bunch crossing will be raised to approximately 20 inelastic collisions, corresponding to $800,000,000$ inelastic collisions per second. Since the event size is about 1.5 megabytes, it is only possible to process and save a small fraction of these events; therefore a dedicated selection system is used, looking for the events of new and interesting physics.

This selection process, called triggering, is a multi-level process (described extensively in [TTDR1]). At first, the Level-1 Trigger (L1) selects about $100,000$ events per second; this number is determined by the speed of the electronics of the detector.

The L1 has three subsystems:

- L1 calorimeter trigger: for electrons, photons, τ candidates, jets, and missing transverse energy;

- L1 muon trigger: muon candidates either detected by both RPC and DT/CSC subsystems or only detected by one subsystem with high quality;

- L1 global trigger: logically combines trigger data from L1 calorimeter trigger and L1 muon trigger.

The events chosen by the L1 are taken as seeds for the second stage of triggering, the High Level Trigger (HLT). It incorporates the Level-2 (L2) and Level-3 (L3) triggers. Combining data from different components of the detector, the event rates are reduced to 5 kHz at the L2 and 150 Hz at the L3. The data output is still large (the event rate of 150 Hz and the event size of 1.5 MB correspond to roughly one CD-ROM per three seconds) and poses a challenge to processing, data analysis and data storage.

The structure of the triggering system is summarized in Figure 3.10.

COMMUNICATION

PROCESSING

16 Million channels

40 MHz COLLISION RATE

3 Gigacell
buffers

100 KHz LEVEL-1 TRIGGER

1,5 Megabyte EVENT DATA

1 Terabit/s

(50000 DATA
CHANNELS)

200 Gigabyte BUFFERS

500 Readout memories

500
Gigabit/s

SWITCH NETWORK

EVENT BUILDER.

150 Hz FILTERED EVENT

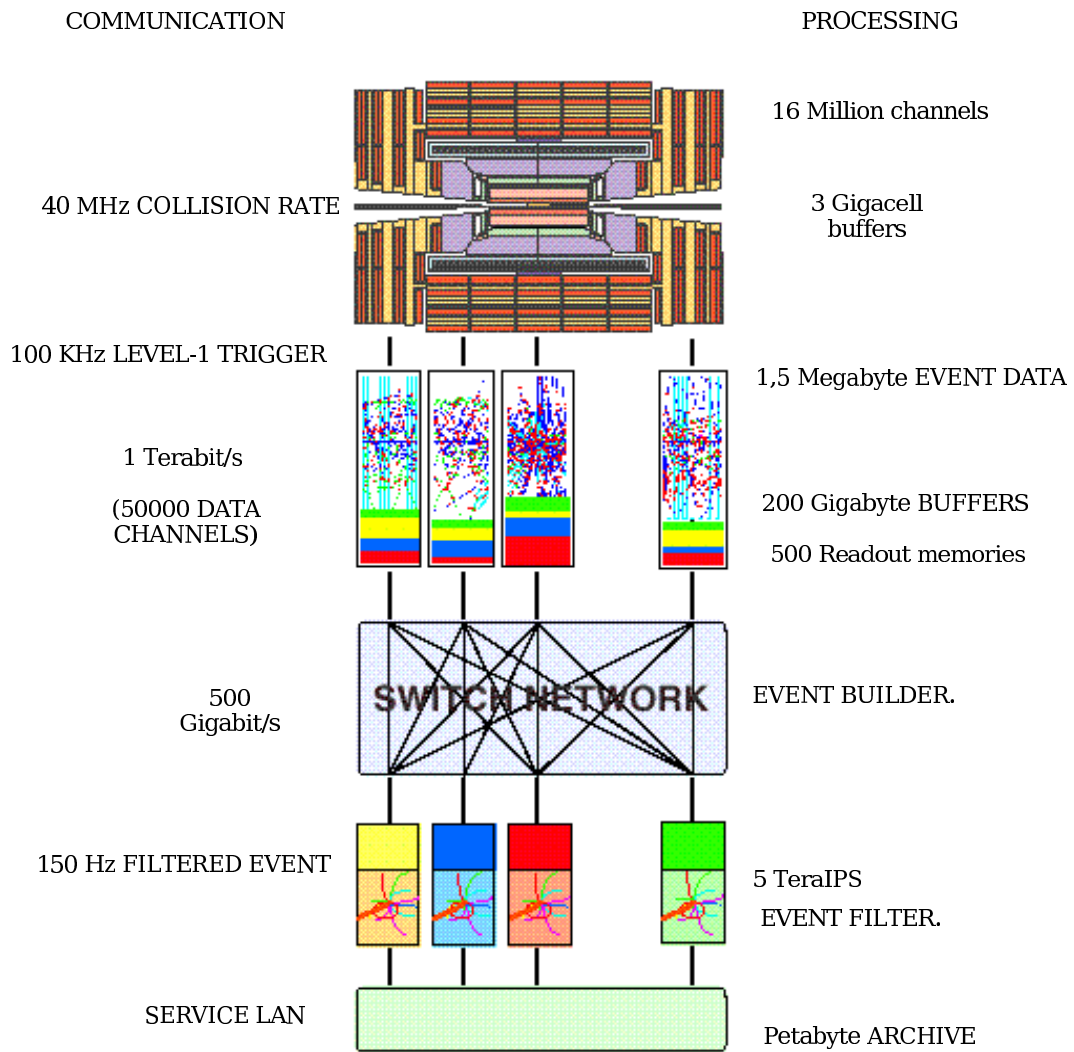5 TeraIPS

EVENT FILTER.

SERVICE LAN

Petabyte ARCHIVE

Figure 3.10: Schematic overview of the triggering and data acquisition system of the CMS experiment. The Level-1 trigger reduces the rate from 40 MHz to 100 kHz, the High Level Trigger reduces the rate further to 150 Hz. (taken from [Bue2])

Chapter 4

Grid Computing for LHC

The LHC experiments use new technologies in different areas, such as detector design, detector technologies, and data acquisition. High data rates recorded by the experiments also require new technologies to meet the data challenge.

Therefore, LHC experiments adapted *grid computing* for their purpose. Grid computing and the LHC specific adaptations are discussed in this chapter.

4.1   Data-centric Approach of High Energy Physics

A collaboration in high energy physics usually evolves in the context of an experiment, which is jointly built and run. The recorded data is evaluated by the geographically distributed collaborators. With one source of data, it is a natural approach to store the data recorded in one data center in proximity of the experiment. This data center can be accessed by the collaborators for data analysis.

Because of the large data streams from the LHC experiments (see section 3.2.5) and the growing network bandwidth, a new way of uniform data access has been chosen: grid computing.

Grid computing allows collaborators to perform their research independently of their geographical location, to use the distributed resources like one homogeneous, large cluster, to share data access with other researchers in their collaboration, to balance the load of resources, to have data redundancy, and to collaborate with colleagues around the world.

4.2   Definition of Grid Computing

There are two approaches to the term *grid*:

1. In grid computing, computing and storage resources can be as easily accessed as

the electric power grid [FK].

2. In the W̲orld W̲ide W̲eb (WWW), users share information by making it available on *home pages*. On the grid, both computing and storage resources are shared. So the connection is stronger than in the WWW and the term grid is more appropriate.

Grid computing is usually defined as follows [FKT], [Fos]:

- "Coordinated resource sharing and problem solving in dynamic, multi-institutional virtual organizations."

- "Grid is a system that coordinates resources that are not subject to centralized control using standard, open, general-purpose protocols and interfaces to deliver nontrivial qualities of service."

Some terms used in these two quotes need further explanation.

Resources refer to computing (i.e. CPU) resources, storage (disk, tape) resources, software installations, and licenses.

V̲irtual o̲rganizations (VO) are communities of individuals and institutions sharing a common goal, trusting each other, and willing to share their resources to achieve their common goal (more information is given in section 4.3).

Dynamic implies that the structure of virtual organizations is subject to continuous change, not only with members joining and leaving virtual organizations but also with resources of a virtual organization being added to or taken from the grid.

Multi-institutional means that a grid incorporates resources located at different participating computing sites.

Not subject to centralized control points out that resources and users live within different control domains, e.g. different institutes or companies.

Standard, open protocols and interfaces guarantee interoperability and are accessible to everyone.

Nontrivial qualities of service means that a grid coordinates its resources in such a way that the utility of the combined system is significantly greater than that of the sum of its parts.

Grid computing methods have been established in different sciences and, to a smaller degree, in the industry. Due to the existence of different grid projects and initiatives, there are a few implementations of the grid.

Project/initiative	Description
EGEE-2	European grid project supporting different sciences; development of middleware and creation of resources in production quality.
D-Grid	Construction of a sustainable grid infrastructure in Germany, establishment of e-science as a framework for science in Germany.
Open Science Grid	Distributed computing infrastructure for scientific research in the US, South America, and Asia.
NorduGrid	Grid research and development collaboration in Scandinavian and other European countries.

Table 4.1: Selection of current grid infrastructure projects with relevance to high energy physics. ([EGEE], [D-Grid], [OSG], [Nordu]).

4.3   Virtual Organizations

The concept of virtual organizations is one of the cornerstones in grid computing, as they describe the relationship between grid resources and grid users. A virtual organization consists of individuals and institutions sharing their resources in order to achieve a certain common goal. In science, virtual organizations are usually scientific collaborations or subsets of these.

The rules for the use of the shared resources are given in the Acceptable Use Policies (AUP) of the VO, which also describe the purpose of the VO and the security guidelines agreed on for the VO.

The IEKP at University of Karlsruhe supports the following virtual organizations:

- CMS: the VO of the CMS collaboration;

- DECH: it comprises the members of the German/Swiss federation in the EGEE project;

- OPS: the VO used for testing the functionality of grid sites.

In order to use resources available on the grid, a potential grid user has to be a member of one or several VOs. Before applying for a membership in a virtual organization, the potential grid user has to apply for a grid certificate from a Certification Authority (CA), e.g. the GridKa CA [GridKa]. A certificate is a public/private key

pair allowing asymmetric cryptography, with the public key being signed by a certification authority (CA). In order to be given his/her certificate, the user has to prove one's identity to the CA. The certificate is then used to authenticate on the grid.

4.4   Grid Middleware and Grid Components

Middleware resembles a software layer between the operating system and the application software. It has a role similar to an operating system, which grants users access to functionality on different brands of computers by using the same set of commands.

For a user, different grid sites ideally "look" the same despite different underlying operating systems, because they are using services provided by the middleware, which takes care of the interaction with the operating system.

In grid computing, there are not only various projects and initiatives (see Table 4.1) but also several kinds of grid middleware systems, often coming along with these projects.

Different machines host different services and provide different functionalities. To have a clear structure for these functionalities, middleware implements services as *grid components*. These components will be explained for the gLite middleware [gLite], which is used for the LHC experiments, in detail:

User Interface (UI): Any computer that can be used for submission of computing jobs, retrieval of computing job outputs, and transfer of data to or from the grid is called a User Interface. User Interfaces do not need a special set-up, since the UI functionality can be installed using software that is in most part independent from the operating system.

A user identifies onself to the grid using a proxy, which is a certificate with a limited duration ($\mathcal{O}(\text{day})$) that does not require a password for authentication and delegation to execute commands on the grid on behalf of the user.

Site wide services: These services need to run at any computing site that wants to offer disk/tape space and computing power on the grid.

Computing Element (CE): This is the gateway service responsible for the distribution of computing jobs arriving at a site to the local computing cluster of Worker Nodes (see below). The choice of the name for this element is misleading, since there is no actual computation done on this machine.

Storage Element (SE): This gateway service manages data transfers from and to the local storage space. The storage space can be on disk, or on tape, or on a combination of both, depending on the system locally used.

Smaller grid sites use disk only systems, while larger sites prefer more complex systems that combine disk and tape space, such as Castor [Castor] or dCache [dCache].

Worker Node (WN): A worker node is a computing node where the user's computing job actually runs. It is installed with all the protocols and software used for communication with the grid, as well as the execution environment for grid tasks. A worker node is usually integrated into a local resource management system, distributing multiple jobs over multiple WNs and scheduling the jobs.

Monitoring Box (MonBox): Each grid site needs to run a Monitoring Box, which is responsible for collecting information on the jobs running at the grid site.

Central grid services: These services are provided centrally by the VO itself.

VO Management Service (VOMS): While users authenticate using proxies, their authorization and, therefore, access to grid resources is managed by this service. This authorization is carried together with the identification in proxy over the different grid services.

LHC Computing Grid File Catalog (LFC): This service is the central service for data management. It is responsible for the association between the logical file names and the physical locations of the files.

Each file has a global unique identifier (GUID), which is the same for all replicas of this single file on the grid, and may have one or various logical file names (LFN) for a single GUID. In addition, each replica has a physical file name (PFN), which includes the site name and the local file name at this site.

The LFC namespace offers a directory structure and an access control list structure similar to the ones used in the Linux operating system.

Resource Broker (RB): The Resource Broker is the service matching the requirements of the jobs submitted by the users to the resources available and sends the jobs to the related sites. It collects information on available services from the Information System and submits a job to the matching site via the Job Submission Service (JSS). The status of a job is recorded by the Logging and Book-keeping Service (LB); it can be queried by grid users and grid services. When a grid job is finished, its output is transferred to the RB used for sending the job to the grid.

Despite its central role in job matching and submission, the Resource Broker is not a single point of failure in the grid, since each VO can have several

Resource Brokers running in parallel; these RBs can also send their jobs to the same resources. Also, a RB can offer its services to more than just one VO.

Information Service: The information on available services is collected by a hierarchical system of information services:

Grid Resource Information Service (GRIS): The most basic service of the hierarchy runs on CE and SE of the grid site, gathering locally the information on available resources and publishing them using the GLUE (Grid Laboratory for a Uniform Environment) schema.

Grid Information Index Server (GIIS): At each grid site, one instance of this service is running. It collects resource information from the local GRIS.

Berkeley Database Information Index (BDII): This grid wide service, of which several instances can run in parallel, collects the resource information from individual grid sites' GIIS services. Its information is queried by the RB for matching jobs and resources.

The workflow for a user job in the gLite middleware is depicted in Figure 4.1.

Since LHC will have large data rates and thousands of researchers analyzing the data, the grid must offer reliable services. Therefore, a formal structure with different resources and different kinds of responsibilities is needed; this structure will be explained in the next section.

4.5   The Structure of WLCG

The World Wide LHC Computing Grid (WLCG, [WLCG]) provides the infrastructure for storing and analyzing data taken by the LHC experiments. The distribution of WLCG participants in Europe is depicted in Figure 4.3.

In order to ensure data accessibility and to guarantee service availability, a multi-layered structure (see Figure 4.2) has been introduced for WLCG. The roles of the participating computing centers are defined by their resources, their services, their problem response times, and their tasks (e.g. Monte Carlo simulations, data reprocessing).

These roles are explained in greater detail in the following paragraphs:

Tier-0 center: In WLCG, there is exactly one Tier-0 center. It is located at CERN, where the LHC will be running. Its main tasks are the initial reconstruction and storage of raw events (of each event recorded at LHC there will be a copy of it on tape at the Tier-0 center) and distribution of copies of the events to Tier-1 centers.
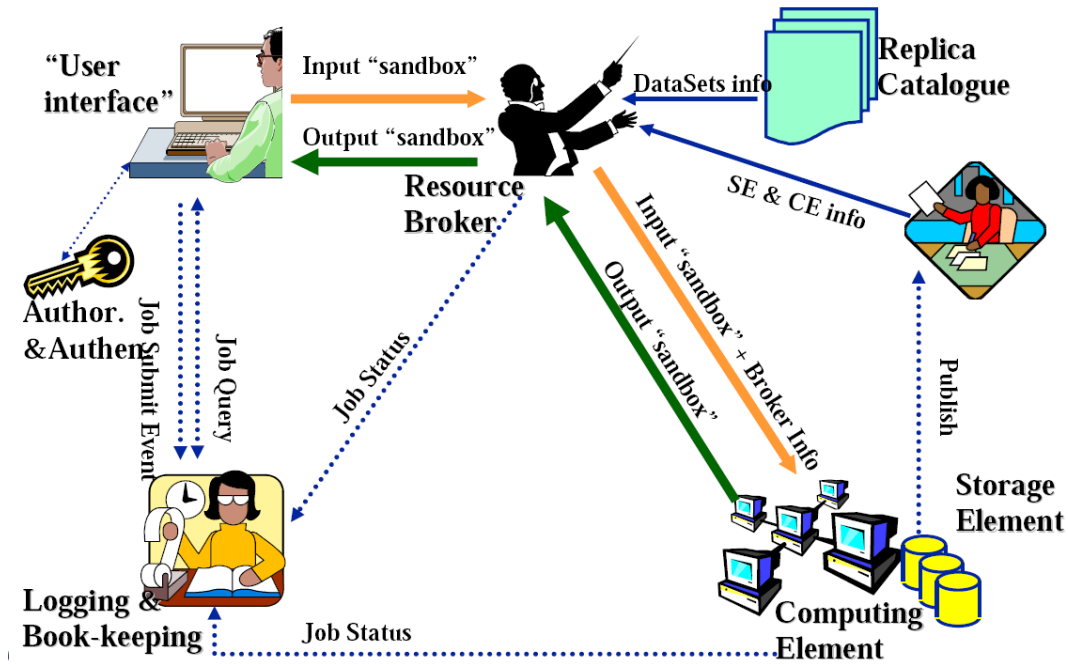
Figure 4.1: On a local User Interface, the user creates a grid job and authenticates to the grid by initializing a proxy certificate, which allows the jobs to act on behalf of the user and with user's credentials. The user sends the job consisting of the job description (see appendix A) and the input sandbox to the Resource Broker. This service matches the job requirements to the resources available on the grid and transfers the job to a suitable site. The job runs at this site; in the end its output (placed in an *output sandbox*) is transferred to the Resource Broker. Now the user can retrieve the output of the job from the Resource Broker. From the job submission to the retrieval of the output sandbox by the user, all status information is logged by the Logging and Book-keeping services. This enables the user to examine the current job status. [EGEE].
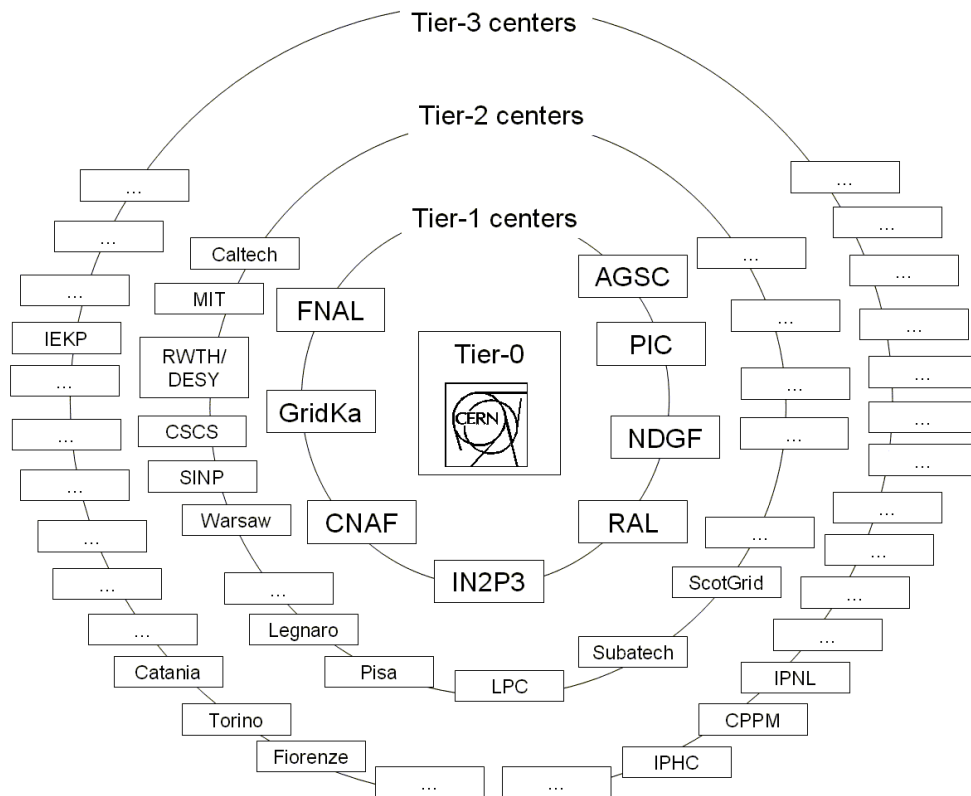
Figure 4.2: The Worldwide LHC Computing Grid is organized in a hierarchical structure. This schematic overview of the multi-Tier structure for CMS shows all Tier-1 centers, a selection of Tier-2 centers and a small selection of Tier-3 centers. In Germany, the Tier-1 center is GridKa at Forschungszentrum Karlsruhe, while the federated Tier-2 center is jointly hosted by RWTH Aachen and DESY Hamburg.
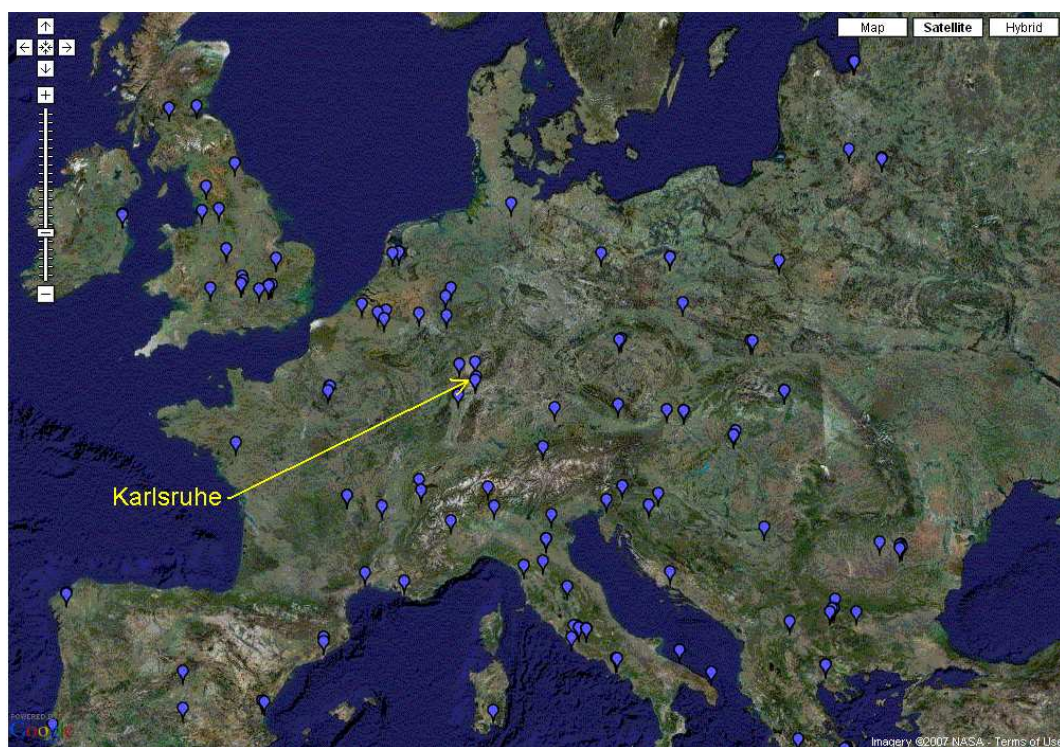
Figure 4.3: This map of Europe, which uses Google Maps [GMaps], shows European grid sites in the WLCG (each balloon represents a grid site, independent of its size). There are two grid sites in Karlsruhe: GridKa and IEKP. (taken from [SFTGM])

Tier-1 centers: About ten Tier-1 centers are distributed over the world, e.g. at
the GridKa [GridKa] computing center of the Forschungszentrum Karlsruhe,
Germany. Some of these Tier-1 centers support all LHC experiments, while
others support only one or two experiments.

Main tasks of Tier-1 centers in CMS are data-centric analyses, the reprocessing
of data, local storage of copies of the events from the Tier-0 center (each event
should be in storage at two different Tier-1 centers), data transfer to Tier-2
centers, and regional support for smaller grid centers. Tier-1 centers, just like
the Tier-0, have very short problem response times.

Tier-2 centers: Tier-2 centers take part in the simulation of events, offer disk space
to analysis groups, store copies of events that are needed for their users' analyses,
and provide their users with computing resources for the final stage analysis.

Most countries participating in LHC experiments have a national Tier-2 center;
overall there are about 35 of these centers supporting the CMS experiment. The
German Tier-2 center for CMS is jointly hosted by DESY Hamburg and RWTH
Aachen.

Tier-3 centers: Universities and institutes being part of one or several LHC collab-
orations run their own Tier-3 centers. These centers have no dedicated respon-
sibilities for the collaboration(s), but they still provide free computing time via
grid mechanisms to other members of their respective collaboration(s). In the
CMS collaboration, Monte Carlo simulation at Tier-3 centers is planned on a
best effort basis.

A Tier-3 center can be a dedicated cluster or, which is more likely, a local cluster
shared by several experiments, like the cluster of the Institut für Experimentelle
Kernphysik at the University of Karlsruhe.

Tier-4: The term Tier-4 does not describe a computer center but a local PC; the
term has become part of a general grid nomenclature and is listed here only for
the sake of completeness.

4.6   Installation and Administration of a local Grid Cluster

In the following section, the installation and administration of a local grid cluster will
be described, focusing on the compute cluster at IEKP.

4.6.1 The IEKP Linux Computing Cluster

The IEKP Linux Computing Cluster (referred to as EKPplus in the following text) can be accessed via a private network and a public network. Grid services have been installed on the cluster for the first time in spring of 2004; since then IEKP resources have been available to the grid.

Detailed information on the set-up of the EKPplus is summarized in [IEKPCluster] and [Kemp]; operating experience in grid computing on the cluster is described in greater detail in [IEKPGrid] and [Bue1].

In the private network of the EKPplus, there are machines and services which cannot and must not be accessed directly from the internet for reasons of security and data safety.

The machines in the EKPplus are:

Computing nodes: The users' jobs (local and grid jobs) run on these machines; they are called *ekpplusXXX*, where XXX stands for a three digit number.

File servers: Their disk space is exported to store datasets; they are referred to as *ekpfsX*, where X is a one digit number.

Dedicated control machine: It hosts the user account management system and the batch system and provides the root file system for the computing nodes. It is called *ekpplusctl*.

Dedicated grid machines: They host the site wide gLite services but for the Worker Nodes. They are called *ekp-lcg-ce*, *ekp-lcg-se*, etc.

The public network offers a portal consisting of six machines for the AMS, CDF, and CMS experimental groups. These machines can be accessed from the public world (mainly by users of the IEKP desktop cluster) and host specific software for the respective experiment. Furthermore, they offer access to the file servers and to the batch system.

The gLite machines *ekp-lcg-ce* and *ekp-lcg-se* are in the private network and in the public network; the former one forwards incoming grid jobs to the batch system of *ekpplusctl*, the latter one hosts the VO software directories and re-exports grid dedicated file space from the file servers. The only grid component with no connection to the private network is *ekp-lcg-mon*, which serves only gLite specific monitoring purposes. The computing nodes also serve as gLite Worker Nodes.

In order to minimize the risk of attacks coming from the internet, the EKPplus as well as the IEKP Desktop Cluster are protected by a *bridged firewall*. To enable outbound connection of the computing nodes, a Network Address Translation (NAT) is in place.

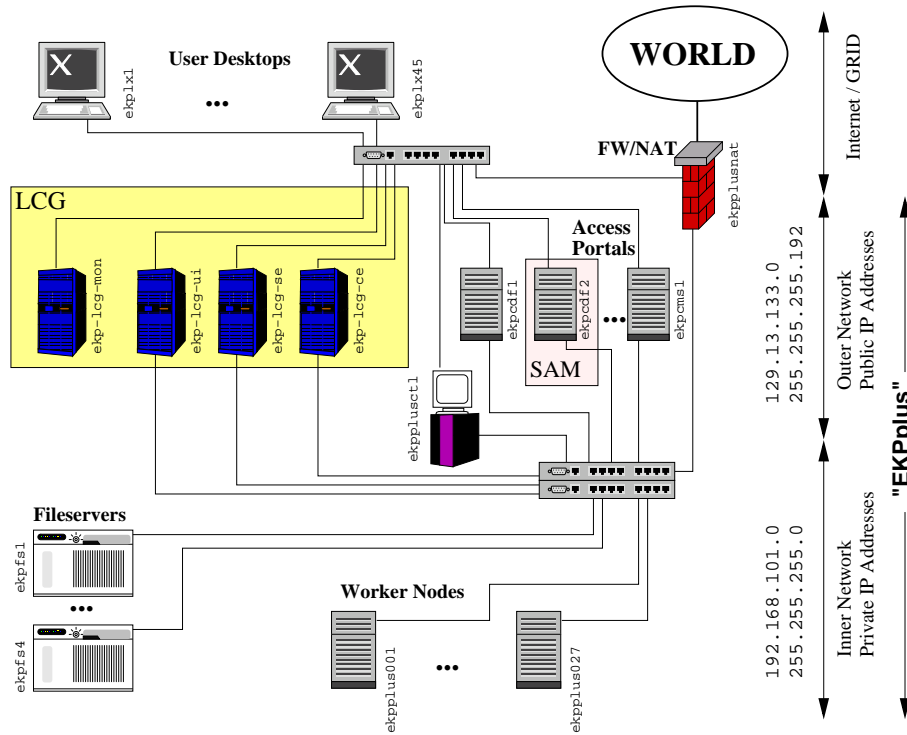The structure of the EKPplus cluster is shown in Figure 4.4.

Figure 4.4: The schematic overview of the EKPplus cluster shows different local services (access portals and file servers), grid services and their connection to the desktop cluster and to the internet. Taken from [Bue1].

4.6.2   Installation of a Tier-2/3 Center Prototype

The Institut für Experimentelle Kernphysik at the University of Karlsruhe was one of the first prototype Tier-2/3 centers in Germany. The main challenge for the site administrators installing grid middleware has been the integration of the grid middleware into the running, existing computer cluster of the institute.

1. **Early Installation Methods**
   Until spring of 2004, the gLite middleware, at that time called LCG middleware, required the use of a special installation system called LCFGng. This system installed grid components, including the operating system (at that time RedHat 7.3), without any customization. This was only acceptable for the portal services CE and SE, but not for the WNs (MonBox did not exist at that time). The challenge was solved by the paradigm shift to *manual installation*, which forced the administrator to do many changes by hand, but relieved them from using LCFGng. This method allowed for the first time to fully integrate the EKPplus computing nodes into the grid.

2. **Generic Installation**
   The generic installation is the most recent method offered for the LCG/gLite middleware installation. It has been offered since the end of 2004 and is well suited for sites of small or medium size. In the following, a short overview on the installation of gLite is given; for extensive information [IEKPGrid] is recommended.

   YAIM: YAIM (<u>Y</u>AIM <u>A</u>in't an <u>I</u>nstallation <u>M</u>anager, [YAIM]) is a configuration manager providing a simple installation and configuration method for setting up a grid site. At IEKP, YAIM is used for installing all grid services but the Worker Nodes (on the WNs, the grid software components are installed using the manual installation). Major sites use installation servers like Quattor or ROCKS, which are appropriate for their size; these systems sometimes trigger a YAIM installation nevertheless.

   Site configuration file: Basically all the information on the set-up of the grid site is stored in this file. It is read out by the configuration software when configuring the respective grid components.
   The information specified in the site configuration file contains:
   - names of all the local grid components,
   - external grid services used (e.g. RB, proxy server),
   - certification authority server,
   - supported VOs, their respective local batch queues and file storage directories, and their VOMS servers.

   Set-up of the local grid components: For each grid component there is a YAIM command, which starts the installation of the component according to the configuration specified in the site configuration file.

   Regular updates of Certification Authority information: Information on trusted CAs is installed on the grid components during the YAIM procedure. This information is crucial for grid security and needs to be up-to-date all the time. A cron job, running preferably a few times a day, fetches and installs the latest CA upgrades.

   Certificate installation: Grid components with portal functionalities, i.e. CE and SE, need host certificates signed by the respective Certification Authority.

   Firewall adjustments: Several grid software components need dedicated ports to be opened for communication, especially the Globus services [Globus] require a large number of ports to be opened. This issue needs to be addressed in the upcoming versions of the grid middleware.

Grid node specific steps: YAIM takes care of most aspects of the configuration of the grid components. Still, a few steps and adjustments need to be done by hand, e.g. synchronizing the time of all grid machines with a time server.

Testing: Any installation needs to be concluded by extensive testing of the services, mainly by test jobs sent to the grid site.

4.6.3   Administrative Tasks

The main administrative task is to operate a reliable and fully functional grid site with a very short problem response time. Especially for Tier-3 sites, restrictions arise from the man-power required.

Basic Linux services and grid middleware components constantly need to be kept up-to-date, predominantly to solve security issues, and thus regularly upgraded. Since this can result in functionality flaws of the grid services, site administrators have to perform basic checks of the grid service with every patch and update.

The local grid administration team offers support and training for local users. The topics range from obtaining certificates to debugging of malfunctions emerging in grid jobs.

Apart from large production VOs like CMS, sites also support smaller VOs like OPS, mainly for testing and training purposes. Experience shows that a major administrative effort is needed for the inclusion of a new VO into a site, since this requires changes in the set-up and allocation of additional resources.

In the past few years, several grid projects have started to offer more user support. Most user support systems are connected to the <u>G</u>lobal <u>G</u>rid <u>U</u>ser <u>S</u>upport (GGUS, [GGUS]). GGUS uses a trouble ticket system to forward the users' problem description to the responsible units, e.g. specific sites or VOs. Having received such a ticket, site administrators fix the problem and close the ticket. In everyday work, tickets are rarely assigned by users; the majority originates from the automatic grid site testing mechanism SAM (<u>S</u>ervice <u>A</u>vailabilty <u>M</u>onitor, [SAM]), which checks the basic functionalities of each grid site a few times a day (more information on grid monitoring tools is given in appendix B).

Smaller computer clusters, mainly at Tier-3 centers, cannot offer dedicated hardware, but still share their local resources in the grid. The main task for administrators is to ensure that resources are accessible to both groups, local users and grid users, although these groups might have completely different requirements.

Several smaller grid sites, including the IEKP, have gained much experience in the installation and administration of grid services, and are planning to transfer their grid services to the computing center of their respective institution.

4.7 Practical Experience of Grid Use

This section summarizes practical experience of grid use gained in the set-up of training infrastructure and in physics simulation and analysis.

4.7.1 Setting up Training Infrastructure

The term *test bed* describes a pool of grid sites supporting a certain VO for testing or training purposes.

Production grids require high availability, reliable services and sufficient resources on a long-term basis. Test beds used for training or demonstration purposes also require sufficient resources, but must guarantee 100% reliability and availability during the time of the training event or the demonstration.

As an example, the experience of setting up training test beds for several GridKa Schools [GridKa] will be given.

The GridKa School [GridKa] is the largest grid training event in Germany. Since 2004, it has been offering hands-on grid tutorials. While in 2004 grid training courses were only a beginner's introduction and a middleware installation course, advanced user courses on grid-enabled applications and analysis on the grid were offered in the following years.

All these courses needed a training test bed to run. With grid evolving in different projects, GridKa School has been using different test beds. When starting to offer hands-on grid tutorials in 2004, there was a need to set up nearly all central grid services specifically for the school. In the following years, several grid projects evolved and existing structures from these projects were used, e.g. the regional test bed of the German/Swiss EGEE federation "dech" was used in 2007.

In order to provide full functionality during the hands-on course at the school, a set of tests is performed every year on the respective test bed. These tests include:

- basic test of the installation of the Globus middleware, which is the basis of LCG/gLite middleware, on each participating grid site;

- tests of the job submission and the integration of the local batch systems into the grid sites by simple so-called "hello world jobs";

- verification of more demanding set-up properties, e.g. of the VO specific software directory at the grid sites;

- extensive testing of data storage services, including file catalog system.

Since 2004, more than 400 participants of GridKa School used training test beds and gained first positive experience on the grid or expanded their knowledge.

4.7.2   Physics Simulation and Analysis

The physics analysis presented in this thesis required a large number of simulated particle collisions, so-called events. The local computing resources at the institute were not sufficient for this task; instead resources available on the grid were used.

For the large scale event simulation, private tools for the job submission, monitoring and output retrieval were used.

The grid job success rate was about 80%; the main reason for grid job failure were local problems at the grid sites, e.g. network problems and scheduling problems, and changes in the set-up of the grid sites, e.g. names of environmental variables relevant to the grid jobs. Overall, about ten grid sites were used for the simulation, with most of the grid jobs being processed at GridKa, CERN and Rutherford Appleton Laboratory (RAL).

For this thesis, the CMS specific tool CRAB (CMS Remote Analysis Builder, [CRAB]) was used to gain access to official CMS data samples of simulated events and to analyze these data sets; CRAB has been designed to offer easy access to physics samples stored on the grid. Yet simulation and analysis were performed by private specialized tools, which had been adjusted for this particular analysis.

Overall, grid computing proved to be an indispensable tool for large scale physics simulation and analysis; it was essential for this analysis.

Chapter 5

Analysis Prerequisites

In high energy physics analyses, data taken with the detector is used to reconstruct the physics events. The complexity of the detector and of the physics necessitates the usage of diverse software tools.

A high energy physics analysis usually consists of several steps. At first, interesting data is collected by so-called "skimming jobs" from the grid (see chapter 4). Furthermore, analysis software runs over the events in the respective dataset, writing out the information for the analysis in a fast accessible format. Final analysis routines process this data, providing histograms and measured values.

In the phase before the actual start-up of a collider, physics events need to be simulated completely. Of course simulation tools will also be needed after the start-up of the detector, e.g. for better understanding of the detector and for analyses based on comparison with simulated events. At first, a physics event is generated in the vacuum (event generation), then the interaction with the detector is computed (detector simulation), then the digital detector response is calculated (digitization), and finally the reconstruction algorithms run. All these steps are explained in this chapter.

In addition, "fast simulation" software can combine the steps from detector simulation to reconstruction; it is used for simulating a large number of events, and uses fast simulation algorithms and parametrization for simulating the interactions.

The CMS analysis tools described in this section are all based around the "ORCA" framework (see subsection 5.3.3). Since 2006, the CMS collaboration has gradually been introducing a new analysis software package called CMSSW (CMS software); the algorithms have been ported from the ORCA software package and are expected to be the same. In CMSSW, the fast simulation was not ready at the time of writing this thesis.

5.1   Event Generation

5.1.1   Pythia

For the generation of high energy physics events, Pythia ([PYTHIA], [Gui]) is one of the most widely used software packages.

In Pythia, hard parton level interactions are calculated by using standard perturbative matrix elements and parton showers. Jet calculations are based on the principle of jet universality, i.e. fragmentation is fundamentally the same for pp and e^+e^- events. The sole difference is that parton-level processes are taken into account.

For fragmentation, Pythia uses a phenomenological model of string fragmentation known as the 'Lund' model.

The emission of strongly interacting particles from gluons and quarks is rich. One parton from the initial state can produce a whole bunch of particles in the final state. Also, photo emission can cause considerable effects.

A perturbative approach is used for describing short distance interactions between leptons, quarks and gauge bosons. The branching ratios for decays of fundamental resonances $(Z,W^{\pm})$ are calculated dynamically. Matrix elements, if available, are used for the calculation of non-isotropic decays.

The calculation of the final state particles is performed according to the following steps:

1. One shower initiator from each beam starts off a sequence of branchings, building up an initial shower.

2. One incoming parton from each of these two showers enters the process, in which the outgoing partons are produced.

3. The outgoing partons branch, building up final-state showers.

4. Having taken the shower initiator out of a beam particle, the beam-remnant is left behind. QCD confinement mechanisms guarantee the non-observability of the outgoing quarks and gluons.

5. Gluons and quarks fragment to color-neutral hadrons.

6. Remaining instable particles decay.

5.1.2   CMKIN

Several Monte Carlo generators are used in the CMS experiment. In order to allow users to access all generators in a similar way, the CMKIN package has been developed.
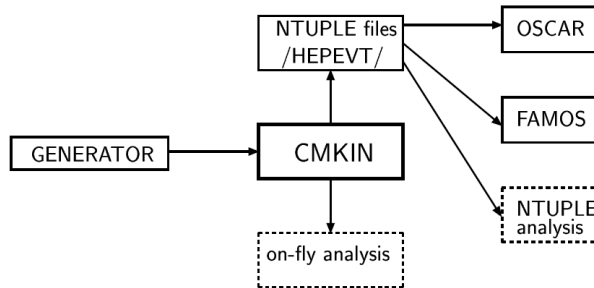
Figure 5.1: Sketch of the interaction of the CMS-specific wrapper program CMKIN with generator programs and detector simulation packages (taken from [PTDR2]).

It is a CMS-specific wrapper for several generators, e.g. for Herwig [HERWIG], Pythia, and Isajet [ISAJET].

CMKIN offers a standard way to interface generators with the detector simulation for the CMS detector (see Figure 5.1). For this purpose, a standardized common block format for high energy physics events called HEPEVT is used. This HEPEVT block is converted to the HBOOK n-tuple format at the end of the event generation process.

5.2 Full Detector Simulation

Event generators describe only particle collisions as they would happen in vacuum. The interactions of the particles with the detector material are simulated by dedicated software, the full detector simulation. The CMS software package used for this task is called OSCAR (Object-oriented Simulation for CMS Analysis and Reconstruction), which uses the toolkit GEANT 4 ([Geant1], [Geant2]).

5.2.1 GEANT 4

GEANT is a multi-purpose software toolkit for simulating the passage of particles through matter. It covers energy ranges from a few hundred eV to the scale of TeV. The applications range from high energy physics to astronautics, biological and medical sciences.

The object-oriented GEANT 4 is the successor of GEANT 3, which had been written in FORTRAN.

For high energy physics, it is important that GEANT can handle complex geometries, as detectors and their materials, and that it simulates the passage of particles through the detector with energy deposition.

5.2.2   OSCAR

The CMS full detector simulation OSCAR ([Oscar1], [Oscar2]) is based on GEANT 4 and on the CMS software framework, which will be described in section 5.3. The complete detector geometry has been described for simulation in OSCAR. This is a very complex simulation with more than $1,000,000$ geometrical volumes.

5.3   Digitization and Reconstruction Software

5.3.1   CMS Object-Oriented Software Architecture

The CMS object-oriented software architecture is implemented in COBRA (Coherent Object-oriented Base for Reconstruction, Analysis and simulation) package. It was the general framework of the CMS software until the emergence of CMSSW.

The COBRA subsystems include:

- CARF (CMS Analysis and Reconstruction Framework),

- DDD (Detector Description Database).

In its object-oriented structure, two main implementation principles are of importance:

- Event driven notification: so-called observers are notified when a new event arrives; the observers react appropriately, e.g. by starting an analysis.

- Action on demand: Objects are only reconstructed if necessary and only once, in order to save CPU time. For example, tracks are only reconstructed if a method or a function requests them.

5.3.2   Digitization

After the simulation of the hits of the event particles in the detector by OSCAR, the electronic readout by the detector and the data acquisition (DAQ) systems is simulated. The digitization process starts from simulated hit positions and simulated energy deposits in the various subsystems of the detector.

5.3.3   Reconstruction

The reconstruction is the process of calculating physical quantities from the raw data collected by the experiment or simulated by the respective software. For the CMS experiment, this is done by the ORCA (Object-oriented Reconstruction for CMS Analysis) software, which is based on the COBRA framework.

The reconstruction is performed in three steps:

1. Data emanating from the digitization process, so-called digis, are used for a local reconstruction within the individual detector module; the output is called 'RecHits'.

2. The RecHits from the individual detector modules of a subdetector are combined to reconstructed objects.

3. In the final step the reconstructed objects of the subdetectors are combined to produce so-called higher level objects.

A scheme of the reconstruction of a muon is given in Figure 5.2.

5.4   Fast Simulation

For large numbers of events a full simulation of all of them takes too much computing time. In this case, a fast simulation tool is used. For the CMS detector this tool is called FAMOS (FAst MOnte Carlo Simulation). It is described in detail in [PTDR1]; in the following paragraphs a short description is given.

FAMOS takes particle lists from event generators as input. The (quasi-)stable particles from these lists are propagated in the magnetic field of the detector through different layers of the subdetectors. During this propagation, the quasi-stable particles are allowed to decay according to the information from the event generator. Interaction with the detector layers can result in further particles, which are also included into the particle list and are propagated/decayed in the same way. FAMOS also overlays pile-up interactions in the same bunch crossing as the original event by adding these events from pre-generated files and treating these particles like any other particle in the event.

FAMOS simulates the following interactions:

- electron Bremsstrahlung;

- photon conversion;

- energy loss of charged particles by ionization;

- multiple scattering of charged particle;

- electron, photon and hadron showering.

The muon simulation is based on a parametrization of resolutions and efficiencies.

A comparison of the full simulation chain and of the fast simulation is given in Figure 5.3.
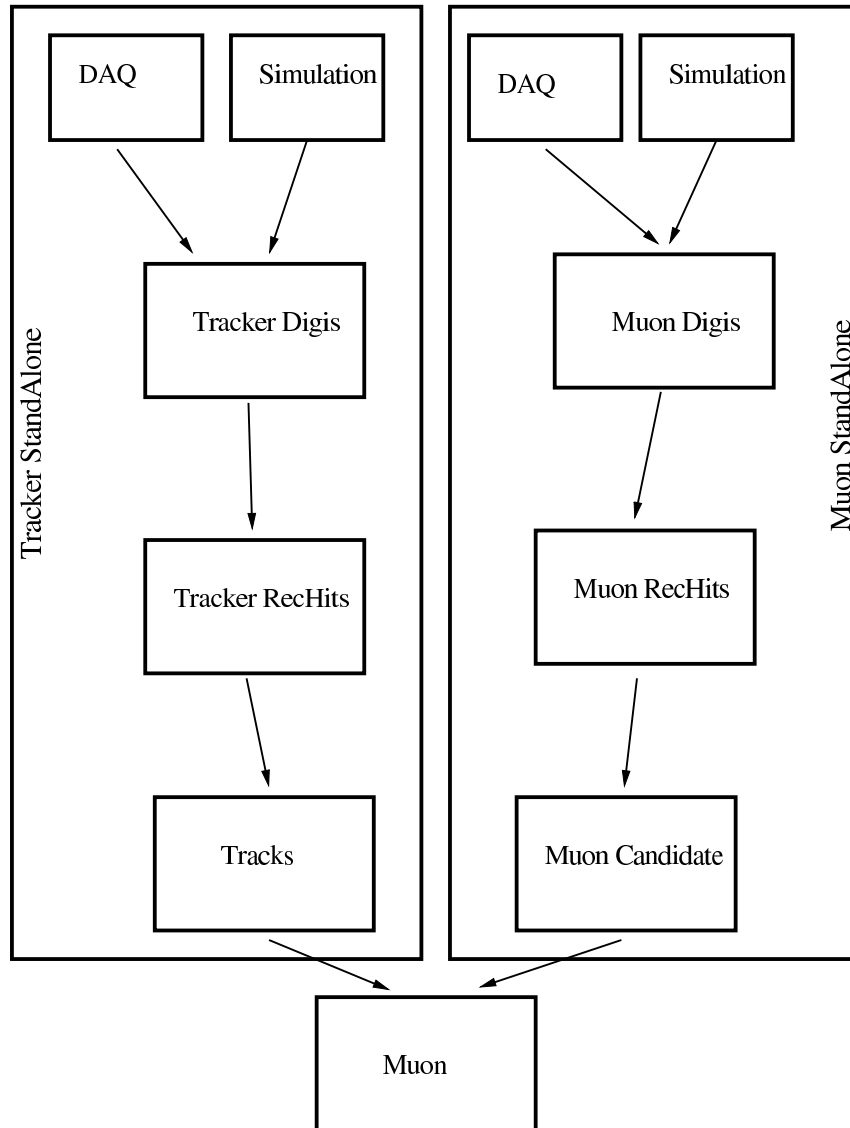
Figure 5.2: The tracks and the muon candidates are reconstructed in parallel in the tracker and in the muon subsystem. Finally, the tracks and the muon candidates are combined to reconstructed muons. [PTDR1]
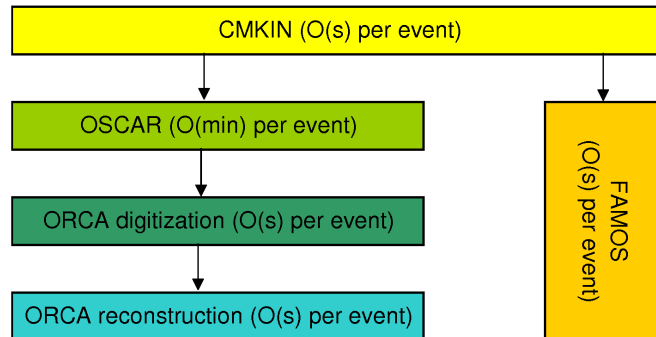
Figure 5.3: Comparison of the full simulation chain and the fast simulation. The fast simulation is significantly quicker and, therefore, better suited for simulating a large number of events.

5.5   Experiment Independent Data Analysis Software

For a long time PAW (Physics Analysis Workstation, [PAW]) has been the most widely used analysis framework in High Energy Physics. With PAW being written in Fortran, the advance of object-oriented programming, especially in C++, created interest in a new framework based on OO principles. The work on ROOT[1] [ROOT] began in 1995, led by Rene Brun and Fons Rademakers at CERN. Today ROOT is a powerful analysis framework; its most important properties are:

- object-oriented framework (with the possibility of interactive analysis by using the CINT interpreter),

- minimization methods,

- creation of histograms and graphics,

- storage methods for fast data manipulation and input/output.

---

[1]ROOT is not an acronym.

Chapter 6

Analysis

Two methods for measuring the W boson mass with the CMS detector are presented in this chapter. Their statistical and systematic uncertainties for an integrated luminosity of one inverse femtobarn of collision data are investigated. Both methods are based on similarities between W boson and Z boson decays and exploit the measurement of Z boson events with a high statistical precision.

The first method, called the morphing method, analytically "transforms" Z boson events into W boson events; the second method, called the scaling method, scales both W boson and Z boson observables with the mass of W boson and Z boson, respectively.

The CMS collaboration presents its physics discovery reach in Volume 2 of its Physics Technical Design Report [PTDR2], in which the following study on the measurement of the W boson mass is mostly included. The results are also available as a CMS note and are published in the Physics Journal G [PhysJG].

At first, both methods are explained, then different simulation methods (described in chapter 5) are compared with respect to the observables relevant to this analysis. Thereafter, the event selection and the physical backgrounds are elucidated, and finally, the W boson measurement with both methods is presented, including the systematic effects.

6.1 Methods for W Boson Mass Measurement

In W boson events, the longitudinal momentum of the W boson is not known at production, since longitudinal momenta of the quarks it is produced from are not known either. The decay modes most suited for the measurement of the W boson mass are $W \rightarrow e\nu_e$ and $W \rightarrow \mu\nu_\mu$, because of their clear signal of the charged lepton. Since the neutrino is only interacting weakly, it does not deposit any energy in the detector. The detector does not cover the whole space angle, so only the missing transverse energy can be calculated as a measure for the transverse momentum of the

neutrino. As described in section 2.2, the standard approach for measuring the W boson mass is to perform template fits to the transverse mass distribution and other distributions.

In the following, two concepts for measuring the W boson are presented. Both methods use similarities between W and Z boson decays and the high statistics of Z boson events at the LHC.

6.1.1   The Concept of the Morphing Method

Introduced in [Sch], the morphing method is motivated by the fact that leptonic W boson decays and Z boson decays mainly differ because of the mass of the respective boson and in the decay products. The idea is to analytically transform a Z boson event into a W boson event; such an event will be called a morphed event in the following.

Since there are differences in the selection of the events, in the distributions of the pseudo-rapidity, η, and the transverse momentum, P^T, of the bosons, a reweighting of the events has to be performed. After the reweighting process, the transverse mass (see section 2.5) distribution of the morphed events can be compared with the transverse mass distribution obtained from the measured W events.

In this thesis, the decays $W \to \mu\nu$ and $Z \to \mu\mu$ are considered. The transformation procedure is performed in the following way:

1. If an event passes the selection cuts for a Z event, the Z boson is reconstructed from the reconstructed muons. Then both muons are transferred into the rest frame of the boson via a Lorentz boost.

2. The mass of the reconstructed Z boson, M_Z^{rec}, is reduced to a value M_Z^{morph}, assuming a W boson test mass, M_W^{test}, and taking into account different widths of the Breit-Wigner distributions of W and Z bosons, Γ_W and Γ_Z:

$$M_Z^{morph}(M_W^{test}) = \left(M_Z^{rec} - M_Z^{PDG}\right) \frac{\Gamma_W^{PDG}}{\Gamma_Z^{PDG}} + M_W^{test}, \qquad (6.1)$$

   where M_Z^{PDG}, Γ_W^{PDG}, and Γ_Z^{PDG} are the world averages for Z boson mass, W boson width, and Z boson, respectively, already quoted in section 2.2.

3. In order to change the momenta of the final state according to the new mass M_Z^{morph} of the Z boson, a two body decay of the mass-reduced boson into a muon and a neutrino is calculated. The directions in the final state, which are back-to-back in the boson's rest frame, are not changed.

4. The system is transferred back into the detector frame via an inverse Lorentz boost, with the assumption that the boson has the identical momentum as before the transformation.

5. Known differences in production and decay of W and Z boson as well as different selection cuts are taken into account by reweighting the modified Z boson events.

6.1.2 The Concept of the Scaling Method

In [GiKe], a method of predicting W boson observables by using a combination of Z boson observables and perturbative QCD is given. The method uses scaled observables

$$X^V = \frac{O^V}{M_V},$$

with O being an observable and M_V being the mass of the vector boson V. The ratio $R(X)$ between the differential cross sections in terms of the scaled variables,

$$R(X) = \frac{d\sigma^W}{dX^W}/\frac{d\sigma^Z}{dX^Z}, \tag{6.2}$$

is obtained from theoretical calculations and gives a prediction for the cross section of the W boson:

$$\left.\frac{d\sigma^W}{dO^W}\right|_{predicted} = \frac{M_Z}{M_W} \cdot R(X) \cdot \left.\frac{d\sigma^Z}{dO^Z}\right|_{measured},$$

with O_Z being

$$O_Z = \frac{M_Z}{M_W}O^W.$$

By comparing this prediction for the observable to the distribution obtained from measured W boson events and Z boson events, the W boson mass, M_W, can be obtained.

When applying this method, the acceptance for W and Z events and the experimental resolution are included as additional corrections into $R(X)$ defined in 6.2. Of the two muons reconstructed in Z boson events, only one is randomly chosen, while the other one is ignored for the respective event.

6.2 Comparison of Full and Fast Detector Simulation

As described in chapter 2, there are two approaches used in simulating the response of the CMS detector to hypothetical physics events: the full detector simulation (using OSCAR and ORCA software packages) and the fast simulation (using FAMOS software package).

The methods presented in this work are studied for a statistics corresponding to an integrated luminosity of one inverse femtobarn (this corresponds to about $20,000,000$

	version
FAMOS	1.3.2
OSCAR	3.6.5
ORCA	8.7.13

Table 6.1: Software versions used for producing the data sets.

$W \to \mu^+\mu^-$ events). A fully simulated analysis cannot be performed due to its need of enormous CPU time and storage space. In order to ensure that the results of the fast simulation give good estimates with respect to the full detector simulation, the results are compared for several variables in the following.

6.2.1   Events

For performing the comparison, the response of the CMS detector to events of the $W \to \mu\nu$ channel has been simulated. Different detector simulations (for software versions see Table 6.1) have been used; the events with full detector simulation have been taken from an official CMS data sample. Only events with exactly one reconstructed muon with a transverse momentum larger than 20 GeV have been used for this study. With this selection criterion, there are about $2,500,000$ fast simulated and about $80,000$ fully simulated events (for the resolution of the missing transverse momentum, there were only about $65,000$ fully simulated events available). Despite the difference in numbers, the fully simulated events still needed more time to be simulated than the fast simulated ones.

6.2.2   Spatial Resolution of the Muon Reconstruction

Relative resolution of the azimuthal angle φ for both fast and full detector simulation is given in Figure 6.1. The OSCAR/ORCA distribution has a mean of $5.739 \cdot 10^{-7}$ with an uncertainty of $8.013 \cdot 10^{-7}$, while the FAMOS distribution has a mean of $1.855 \cdot 10^{-7}$ with an uncertainty of $1.667 \cdot 10^{-7}$; both mean values are statistically compatible with each other. The RMS for FAMOS simulated events is 18.6% larger than the one for ORCA simulated events.

The comparison of the relative resolutions of pseudo-rapidity η in Figure 6.2 shows a mean value of $-4.307 \cdot 10^{-6}$ with an uncertainty of $1.843 \cdot 10^{-6}$ for the FAMOS simulation and a mean of $-7.964 \cdot 10^{-9}$ with an uncertainty of $3.578 \cdot 10^{-7}$ for the ORCA simulation. Only the mean value of the fast simulation is compatible with 0. The RMS for the fast simulation is 10.7% larger than the one for the full simulation.
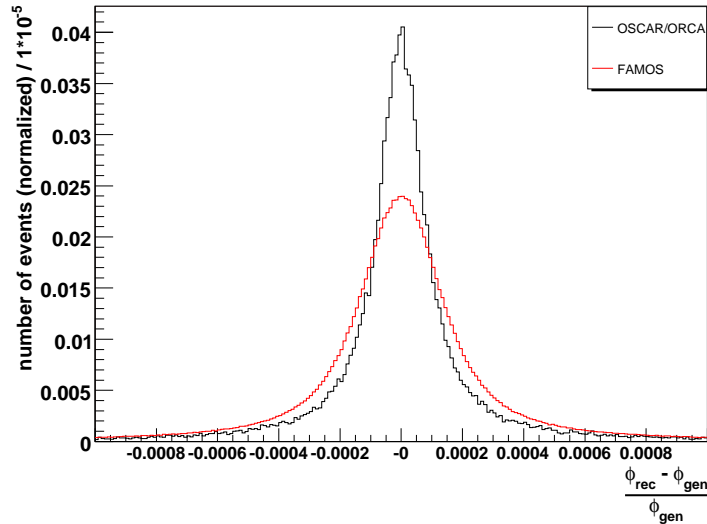
Figure 6.1: Relative resolution of the azimuthal angle φ. The result from the fast simulated events is given by the red distribution, which has a mean of $1.855 \cdot 10^{-7}$ and an RMS of $2.653 \cdot 10^{-4}$. The black curve shows the result from the full detector simulation, has a mean of $5.739 \cdot 10^{-7}$ and an RMS of $2.236 \cdot 10^{-4}$.

6.2.3 Transverse Muon Momentum

The comparison of the transverse momentum of the muon in the $W \rightarrow \mu\nu$ for the Monte Carlo generator Pythia, the fast simulation FAMOS and the full detector simulation OSCAR/ORCA is given in Figure 6.3. The distributions are in good agreement.

The transverse momentum of a charged particle in a homogeneous magnetic field is calculated using the measured curvature of the trajectory, which is inversely proportional to the transverse momentum. Therefore, it is important to compare the resolutions of the inverse muon momenta for the fast and the full detector simulation. These resolutions are given in Figure 6.4; both distributions are slightly asymmetric and prefer larger reconstructed radii.

For comparison, the absolute and relative resolutions of the transverse muon momentum for FAMOS and OSCAR/ORCA simulations are shown in Figure 6.5 and Figure 6.6, respectively. Both simulation programs tend to reconstruct larger transverse momenta compared to the Monte Carlo generator data. The mean of the relative resolution is $(2.804 \pm 0.002) \cdot 10^{-3}$ for the fast simulation and $(3.925 \pm 0.014) \cdot 10^{-3}$ for the full detector simulation.

The resolution of the muon momentum worsens for P^T intervals of the same length for higher values of the muon momentum, because the curvature of the track is measured in the detector. This effect is shown with a study on events simulated with
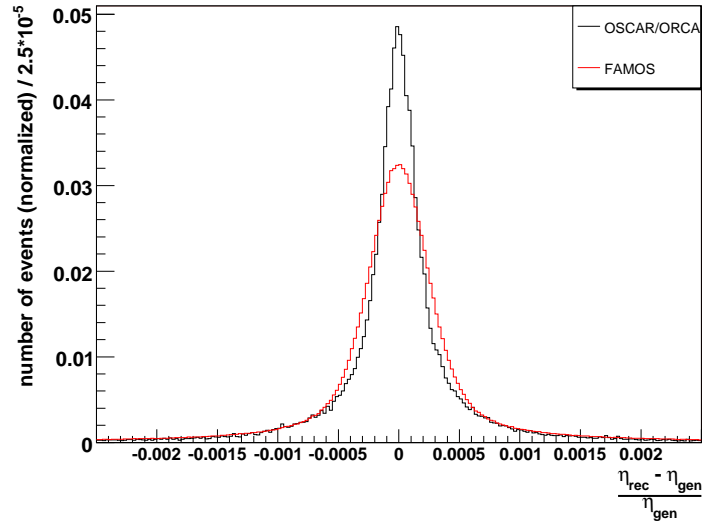
Figure 6.2: Relative resolution of the pseudo-rapidity η for the fast and the full detector simulation. The results from the OSCAR/ORCA simulation are shown in black, with a mean of $-7.964 \cdot 10^{-9}$ and an RMS of $5.693 \cdot 10^{-4}$. The distribution of the relative resolution for the FAMOS simulation is shown in red; it has a mean of $-4.307 \cdot 10^{-6}$ and an RMS of $5.141 \cdot 10^{-4}$.
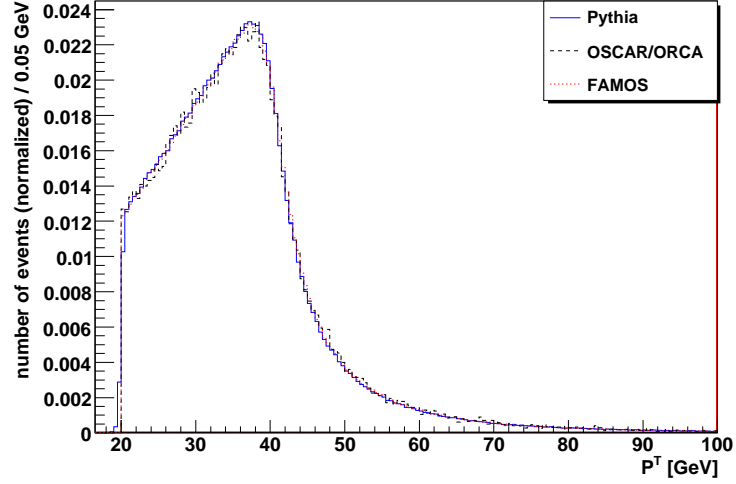
Figure 6.3: Comparison of the transverse muon momenta for the Monte Carlo generator, the fast simulation and the full detector simulation. The distribution of the muon momentum for the Monte Carlo generator Pythia is shown in blue (solid line); the curves from the fast and the full detector simulation are given in red (dotted line) and black (dashed line). All distributions are in good agreement.
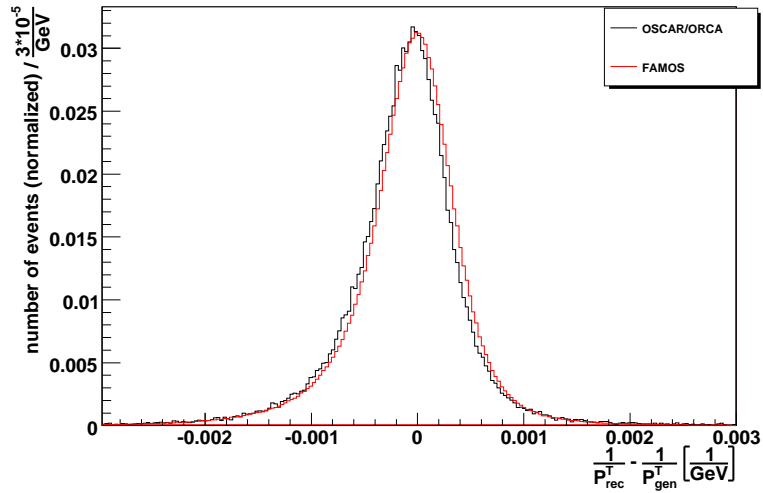
Figure 6.4: Absolute resolution of the inverse muon momentum. The distribution in black shows the results of the full detector simulation, with a mean of $-1.16 \cdot 10^{-4}$ GeV^{-1} and an RMS of $5.556 \cdot 10^{-4}$ GeV^{-1}. The red curve depicts the distribution from the fast detector simulation; its mean is $-7.78 \cdot 10^{-5}$ GeV^{-1}, its RMS is $5.333 \cdot 10^{-4}$ GeV^{-1}.
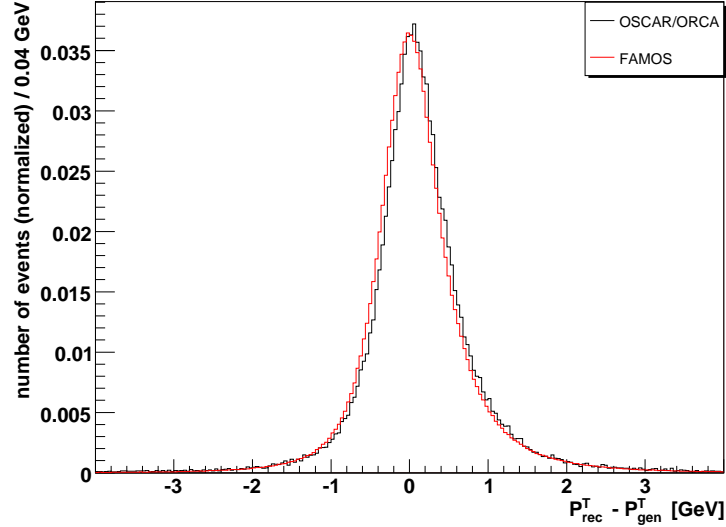
Figure 6.5: Absolute resolution of the transverse muon momentum. The FAMOS distribution is given in red color; it has a mean of 0.09545 GeV and an RMS of 0.6808 GeV. In black, the OSCAR/ORCA results are shown, having a mean of 0.1351 GeV and an RMS of 0.715 GeV.
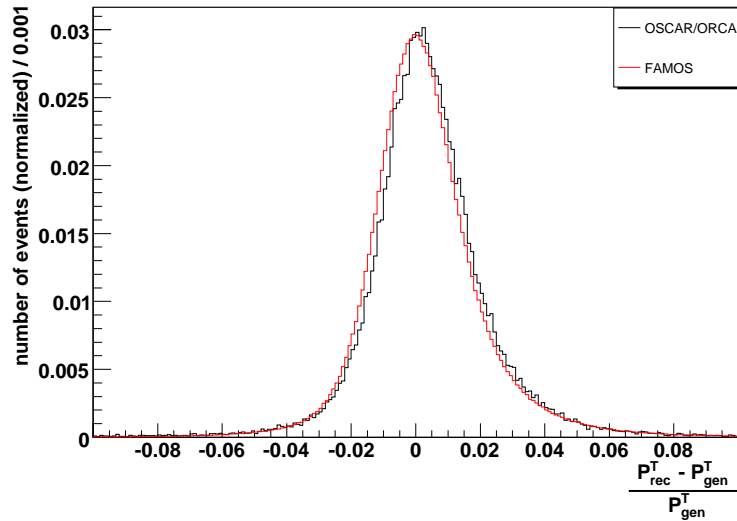
Figure 6.6: Relative resolution of the transverse muon momentum for the fast and the full detector simulation. For the former, the distribution is given in red. It has a mean of $2.80 \cdot 10^{-3}$ and an RMS of $18.02 \cdot 10^{-3}$. The latter is represented by the black curve; its mean is $3.93 \cdot 10^{-3}$ and its RMS is $18.7 \cdot 10^{-3}$.

FAMOS (the statistics of the fully simulated events is not sufficient for such a study) in Figure 6.7.

6.2.4   Missing Transverse Momentum

Since the neutrino is only interacting weakly, it cannot be measured directly by the detector. Instead, the missing transverse energy is measured. The relative resolution for the missing transverse momentum reconstruction is given for both fast and full detector in Figure 6.8. As expected, the relative resolution is much lower than for the muon transverse momentum for both distributions. The mean value for the OS-CAR/ORCA resolution is 0.137 ± 0.002, while for the FAMOS simulation it is 0.108 with a negligible statistical uncertainty. The parametrization used in the FAMOS simulation is clearly visible.

6.2.5   Conclusion

The comparison of the decay of a W boson into a muon and its according neutrino for the fast simulation with FAMOS and the full detector simulation with ORCA shows that angular observables have symmetric distributions, but differ in relative resolutions; the relative resolutions in FAMOS are worse and, therefore, can only be used as conservative approximations.

The transverse muon momentum is reproduced less precisely than angular observables. The relative resolution is not symmetric; both simulations have a tendency of slightly overestimating P^T.

Since it is being measured only indirectly, the resolution of the neutrino is much lower than the resolutions of the other observables discussed in this subsection. The FAMOS parametrization results in a better resolution than the resolution of the fully simulated events.

The study performed in this thesis can only be performed with FAMOS due to the amount of computing time needed. Simulating all events with FAMOS takes roughly 1.5 CPU years, while a full detector simulation of all events would increase this amount of time by a factor of about 100.

During data taking at LHC, it will be necessary that the differences between measured data and simulation are smaller than the differences between the simulations with FAMOS and OSCAR/ORCA shown in this section.
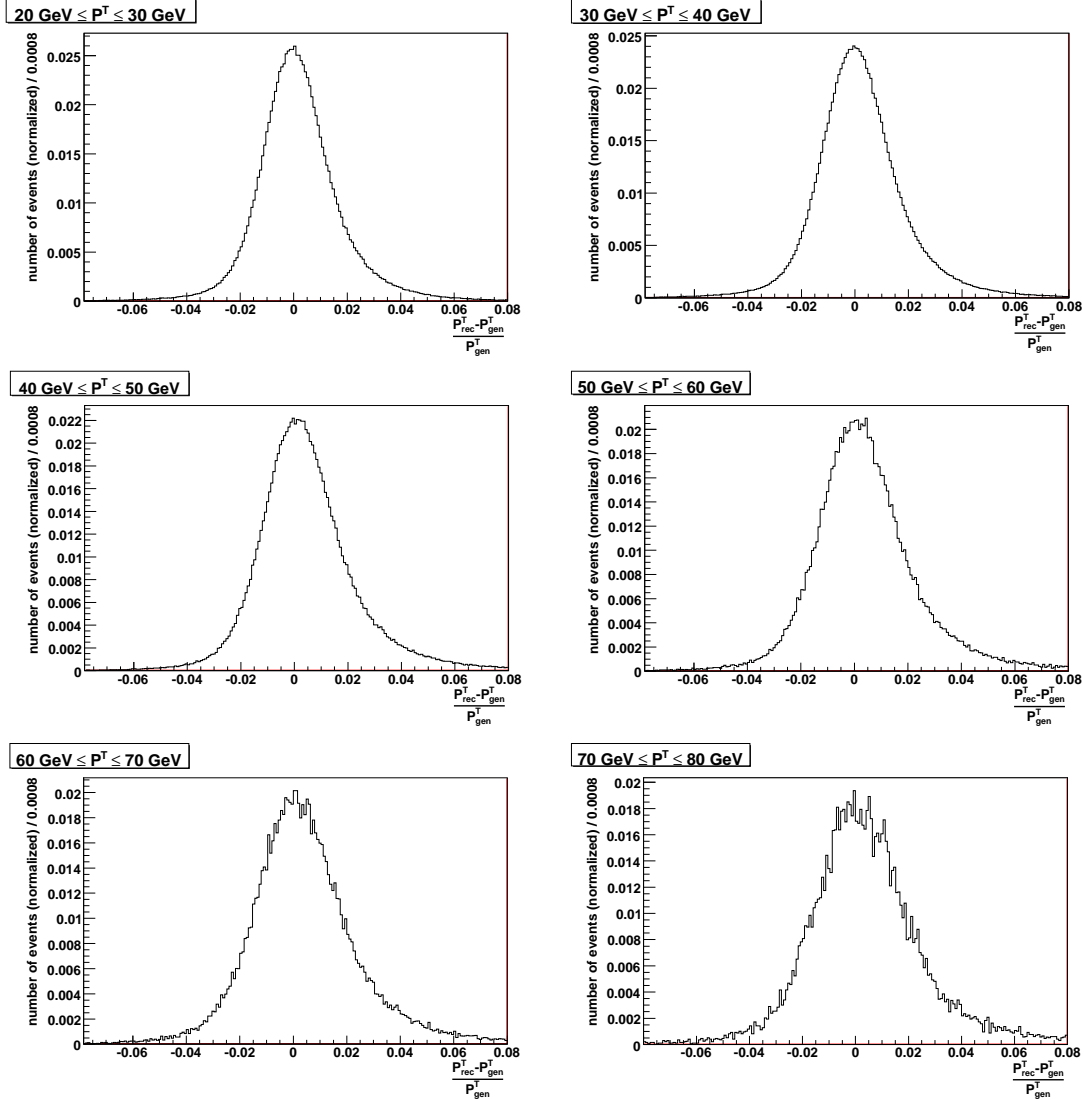
$P^T \in$	mean	RMS	number of events
[20 GeV, 30 GeV]	$1.94 \cdot 10^{-3}$	$16.16 \cdot 10^{-3}$	$775,513$
[30 GeV, 40 GeV]	$2.06 \cdot 10^{-3}$	$17.01 \cdot 10^{-3}$	$1,077,457$
[40 GeV, 50 GeV]	$4.44 \cdot 10^{-3}$	$18.36 \cdot 10^{-3}$	$475,957$
[50 GeV, 60 GeV]	$4.08 \cdot 10^{-3}$	$19.30 \cdot 10^{-3}$	$111,903$
[60 GeV, 70 GeV]	$3.89 \cdot 10^{-3}$	$20.13 \cdot 10^{-3}$	$43,338$
[70 GeV, 80 GeV]	$3.76 \cdot 10^{-3}$	$21.35 \cdot 10^{-3}$	$19,964$

Figure 6.7: The relative resolution of the transverse muon momentum is shown in different P^T intervals for the fast detector simulation. Since the transverse muon is measured via the curvature of the track, the uncertainty increases with growing P^T.
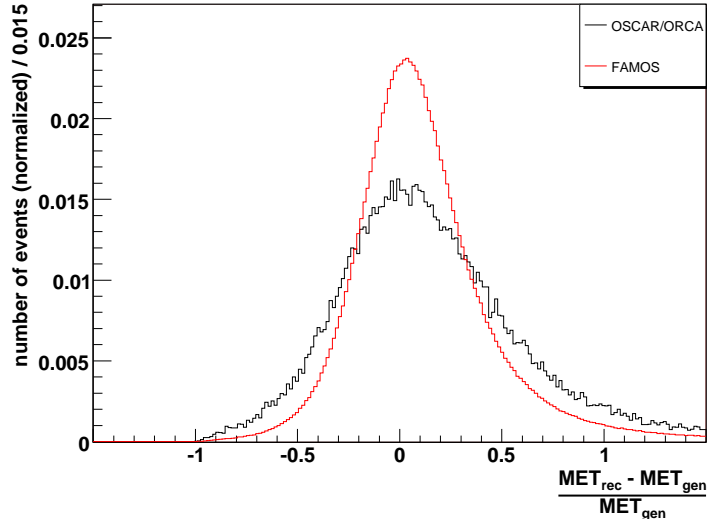
Figure 6.8: The results of the full detector simulation are given in black, with a mean of 0.137 and an RMS of 0.429. The distribution in red depicts the relative MET resolution for the fast simulation; its mean is 0.108 and its RMS is 0.328.

	single muon events	di-muon events
Level-1 trigger	14 GeV	3 GeV & 3 GeV
High Level trigger	19 GeV	7 GeV & 7 GeV

Table 6.2: Level-1 and High Level trigger thresholds for selecting single muon and di-muon events.

6.3   Event Selection

6.3.1   Detector Acceptance and Trigger System

In the triggering system of CMS, single muon events are only accepted if their transverse momentum is larger than 14 GeV and 19 GeV for the Level-1 trigger and the High Level trigger, respectively. For di-muon events, these thresholds are lowered to 3 GeV and 7 GeV required for each muon, respectively (see Table 6.2).

Since an effective muon reconstruction is only possible in the barrel regions and the endcaps of the detector (which cover the pseudo-rapidity range up to $|\eta| \leq 2.4$), the selection cuts are chosen tighter, $|\eta| < 2.3$, to avoid edge and threshold effects.

selection cut	efficiency
exactly 1 μ reconstructed	58.2%
$P^T(\mu) \geq 25$ GeV	40.8%
$E^T_{miss} \geq 25$ GeV	35.9%
$|\eta^\mu| \leq 2.3$	34.6%
$|\vec{u}| \leq 20$ GeV & # jets≤ 1, $P^T_{jet} \leq 30$ GeV	23.7%

Table 6.3: This table lists the efficiencies of the selection cuts consecutively applied to the $W \to \mu\nu$ events. The transverse momentum of the hadronic recoil is denoted by $|\vec{u}|$. The events were simulated by the FAMOS software package.

6.3.2   Selection Cuts and Backgrounds for W Boson Events

Selection Cuts

A W boson decaying into a muon and a neutrino is visible in the detector as a reconstructed muon and missing transverse energy. The latter is used as an indirect measurement of the neutrino, since neutrinos are only weakly interacting and therefore do not dispose any energy in the calorimeters.

In this analysis, we require exactly one muon with a transverse momentum exceeding 25 GeV to be reconstructed, which is well in the acceptance region of the muon detector, $|\eta| < 2.3$. For the missing transverse energy, E^T_{miss}, the threshold is $E^T_{miss} > 25$ GeV. The threshold for the hadronic recoil $\vec{u}$, which balances the transverse momentum of the W boson and is measured in muonically decaying W events via the missing transverse energy in the calorimeter, $E^T_{miss,calo}$, is $|\vec{u}| < 20$ GeV. Finally, events with two jets or one jet with a transverse momentum of $P^T_{jet} > 20$ GeV are rejected. The two last selection cuts discard W event candidates with a high reconstructed transverse momentum. The efficiencies of the consecutively applied selection cuts are summarized in Table 6.3; the reconstruction algorithms are listed in Table 6.4.

Backgrounds

Processes with event topologies in the reconstructed final state similar to the signal are called background. There are physical backgrounds, which have a similar event topology already in the physics process, and detector backgrounds, which are due to reconstruction inefficiencies, false reconstruction and the limited spatial coverage of the detector.

The most important contribution for the background of the W events is a detector

object	CMS reconstruction algorithm
muon	global muon reconstructor
MET	MET from CaloRecHits
jets	iterative cone (radius 0.5) calibrated (JetPlusTrack)

Table 6.4: The reconstruction algorithms used for muons, MET and jets. For the jets, an energy threshold of 10 GeV is used. The algorithms are described in detail in [PTDR1].

background: it is the background coming from $Z \to \mu^+\mu^-$ events, in which one muon is not in the acceptance range of the muon detectors or is not reconstructed. There are possibilities for reducing the contributions of the background to a certain extent; for events with muons not reconstructed, an additional selection on muon hits in the muon chamber can reduce the number of events; for muons not in the acceptance range of the detector, a selection criterion can be testing if the direction of the missing transverse energy points into the acceptance region for muons. This can be done by using a W mass constraint; unfortunately, the resolution of the longitudinal component of MET is insufficient for doing so. As can be seen in Figure 6.9, for the transverse masses and the scaled muon momentum this background is fortunately rather flattish, but unfortunately sitting in the region of the Jacobian edge. This has been confirmed by the D0 collaboration, which shows such a background at a similar level [Leone].

Another background arises from the $W \to \tau\nu \to \tau\nu\mu\nu\nu$ events; it has been estimated in [Hay] to amount to about 1.3%. This background can be suppressed by the selection cut on the momentum of the muon, since neutrinos carry a large fraction of the momentum in these events. This background mainly contributes to reconstructed transverse masses up to 75 GeV and scaled muon momenta up to 0.95, i.e. below the Jacobian edge (see again Figure 6.9). This result is also confirmed by results of the D0 collaboration [Leone].

A further possible source for physical background events comes from the process $pp \to bb \to \mu + X$, which can provide signatures in the detector similar to the ones of the W signal by faking signal events. A large number of fully simulated events is needed for studying this decay. This background can be reduced, e.g. by using b-tagging. It is expected to be small, and is not studied in this work.
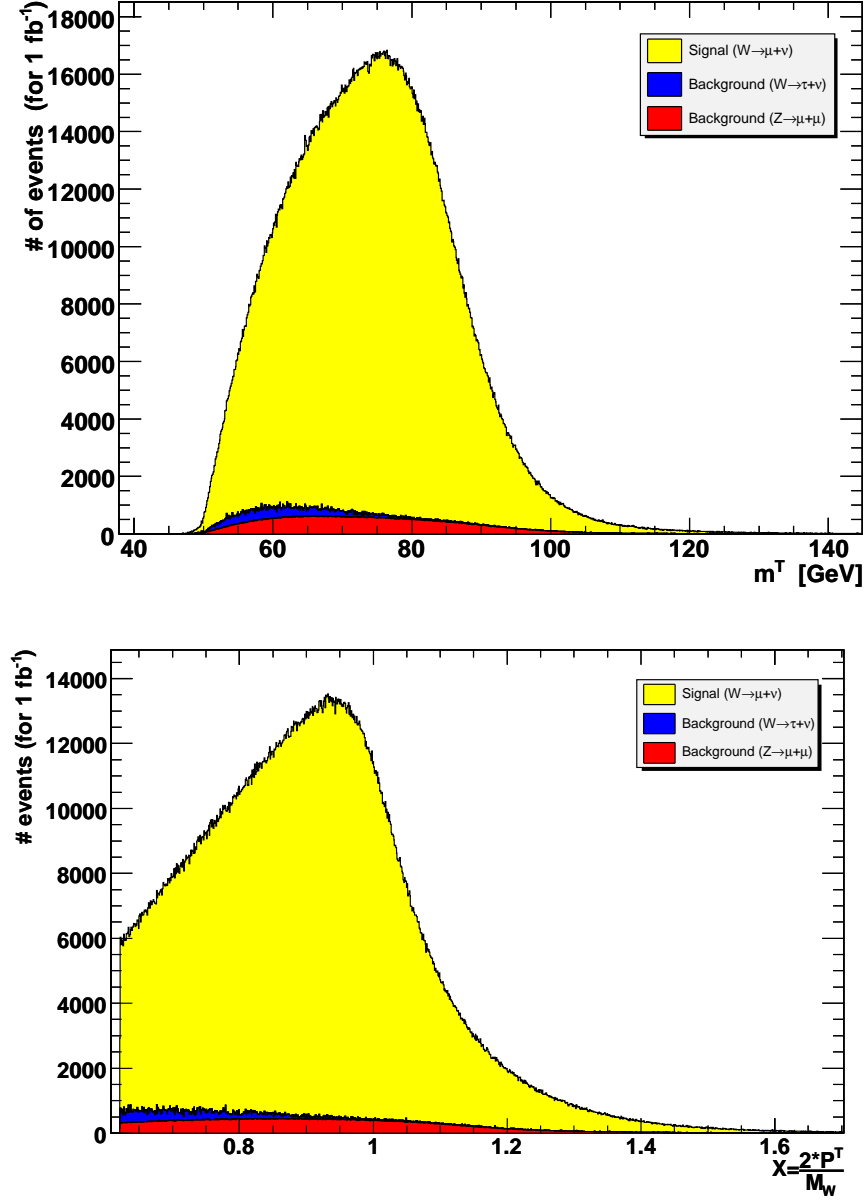
Figure 6.9: FAMOS simulated distributions of the reconstructed W event candidates with contribution by the background processes; transverse mass above (bin width 0.1 GeV), scaled muon transverse momentum below (bin width $5 \cdot 10^{-4}$). The yellow area represents the W signal, the blue area represents the background coming from $W \to \tau\nu$ events (this background has only small effects in the area of the Jacobian edge), and the red area shows the largest background process coming from $pp \to Z/\gamma^* \to \mu^+\mu^-$ events. This background is in the area of the Jacobian edge in both histograms. All distributions have been scaled to an integrated luminosity of 1 fb^{-1}.

selection cut	efficiency
exactly 2 μs with different charge reconstructed	40.9%
$P^T(\mu) \geq \frac{M_Z}{M_W} \cdot 25$ GeV	28.3%
$|\eta^\mu| \leq 2.3$	27.1%
$|\vec{u}| \leq 20$ GeV & # jets≤ 1, $P^T_{jet} \leq 30$ GeV	16.6%

Table 6.5: Sequentially applied cuts for fast simulated events of the $Z \rightarrow \mu^+\mu^-$ channel, with the percentages of the remaining events given in the right column. The transverse momentum of the hadronic recoil is given by $|\vec{u}|$.

6.3.3   Selection Cuts and Backgrounds for Z Boson Events

Selection Cuts

For Z event candidates, the most important requirement is that exactly two muons of opposite charge are reconstructed. For Z event candidates, we require transverse momenta of $P^T \geq \frac{M_Z}{M_W} \cdot 25$ GeV for both reconstructed muons, which is the same cut as for the muon from W event candidates (see subsection 6.3.2; only scaled by the ratio of the boson masses). Also, reconstructed muons need to have a pseudo-rapidity in the range of $|\eta| < 2.3$. For the recoil, $\vec{u}$, which balances the transverse momentum of the Z boson, the selection cut is $|\vec{u}| \leq 20$ GeV; the recoil is measured by the missing transverse energy in the calorimeter. In order to suppress QCD background events, only events with no reconstructed jets or exactly one reconstructed jet with $P^T_{jet} \leq 30$ GeV are selected. These selection cuts are summarized in Table 6.5, along with the fraction of Z events passing the respective cuts.

Backgrounds

The selection cuts listed in the previous subsection provide a very clear sample of Z events. The irreducible background of γ^*/Z interference events produced via a virtual photon remains, but is well understood. The Tevatron experiments CDF and D0 do not see any significant background contributions in their Z signals [Leone].

In [Bue2], backgrounds from the processes $b\bar{b} \rightarrow \mu^+\mu^- + X$, $c\bar{c} \rightarrow \mu^+\mu^- + X$ and $s\bar{s} \rightarrow \mu^+\mu^- + X$ were investigated with the Monte Carlo generator Pythia only. They are summarized in the following paragraphs.

For the Monte Carlo generator, a preselection criterion of at least two muons of transverse momenta larger than 25 GeV within the pseudo-rapidity range of $|\eta| < 2.4$ was used. In addition, a selection cut requiring two muons of different charge was applied; then the combination with the highest invariant mass was chosen.

For $Z \rightarrow \mu^+ \mu^-$ events, 32.3% of the events passed preselection and selection criteria.

- $b\bar{b} \rightarrow \mu^+ \mu^- + X$:
  In $pp \rightarrow b\bar{b} \rightarrow \mu^+ \mu^- X$ processes, muons of high energy can be produced. The cross section is large; it is 0.71 mb and, thereby, about six orders of magnitude larger than the cross section of the signal $pp \rightarrow Z \rightarrow \mu^- \mu^+$. A data sample of 2007 nb^{-1} was produced with Pythia. Six events passed preselection and selection cuts. Using Poisson statistics [BL], the maximum number of background events can be calculated; the number of background events is limited to 1,658 events, corresponding to 1.07% of the signal, at the 95% confidence level.

- $s\bar{s} \rightarrow \mu^+ \mu^- + X$ and $c\bar{c} \rightarrow \mu^- \mu^+ + X$:
  While these processes do not qualify for producing highly energetic muons, their cross sections are larger by about seven magnitudes than the signal cross section and therefore still need to be considered. The simulated Monte Carlo events correspond to integrated luminosities of 485 nb^{-1} and 496 nb^{-1} for the $s\bar{s}$ and the $c\bar{c}$ sample, respectively. With no events passing the preselection cuts for both processes, the signal limits are 1.15% for $s\bar{s}$ and 1.12% for $c\bar{c}$ events, both at the 95% confidence level.

6.4   Reconstruction of W Boson Mass with the Morphing Method

6.4.1   The Resolution of MET and of the Recoil

As mentioned in subsection 3.2.5, there are approximately five inelastic collisions on average per bunch crossing during the low luminosity phase of LHC. These pileup events bias the missing transverse energy in the calorimeter, since they have missing transverse energy themselves; this contribution is investigated for W boson and Z boson events in this subsection.

For $W \rightarrow \mu\nu$ and $Z \rightarrow \mu\mu$ events, the missing transverse energy, E_{miss}^T, is measured via the missing transverse energy in the calorimeters, $E_{miss,calo}^T$, and the momentum/momenta of the reconstructed muon(s). For W boson events, $E_{miss,calo}^T$ corresponds to the transverse momentum of the W boson and, thereby, to the hadronic recoil. In Z events, $E_{miss,calo}^T$ corresponds to the reconstructed transverse momentum of Z boson and, thereby, to the hadronic recoil; for these events, there is also another possibility for determining the transverse momentum of the boson. It can be reconstructed rather precisely from the transverse momenta of the reconstructed muons.
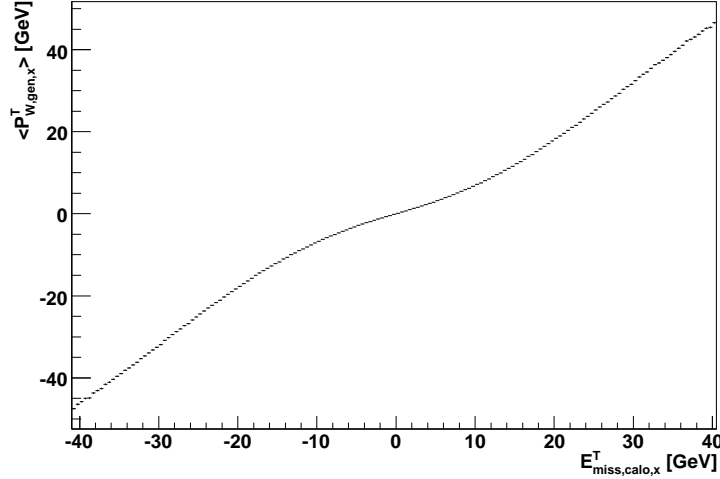
Figure 6.10: This profile plot depicts the average generator value of the x-component of the W boson transverse momentum against the measured x-component of the calorimeter MET. The slope in the region around 0 GeV is smaller than for $|E^T_{miss,calo,x}| > 20$ GeV. The bin width for $E^T_{miss,calo,x}$ is 0.25 GeV.

For simulated W boson events, one expects the x-component of the missing transverse energy in the calorimeter and the x-component of the hadronic recoil of the event to be linearly correlated, ideally to be directly proportional (because of symmetry, this also applies to any transverse component). For Figure 6.10, all W events with exactly one reconstructed muon have been used. In the profile plot, the average generator value of the x-component of the W boson transverse momentum, $< P^T_{W,gen,x} >$, is given against the measured x-component of the calorimeter MET, $|E^T_{miss,calo,x}| > 20$ GeV. As can be seen, the slope around 0 GeV is smaller than the slope for $|E^T_{miss,calo,x}| > 20$ GeV. To investigate this further, a scatter plot and a contour plot of $P^T_{W,gen,x}$ versus $E^T_{miss,calo,x}$ are given in Figure 6.11. The scatter plot shows a distribution, which has a shape of a parallelogram; the contour plot suggests that two superposing ellipses might be the reason for the parallelogram shape, with one having its principal axis on $P^T_{W,gen,x} = 0$ GeV.

Taking a closer look at the distributions of the generated values of $P^T_{W,gen,x}$ for different intervals of $E^T_{miss,calo,x}$ in Figure 6.12, one can clearly see a second peak around 0 GeV for the distributions of $P^T_{W,gen,x}$ in the intervals of $[-20\,\text{GeV}, -19.5\,\text{GeV}]$ and $[25\,\text{GeV}, 25.5\,\text{GeV}]$. This second peak originates from the pileup contribution uniformly distributed around 0 GeV. This is the reason for the parallelogram shape in the scatter plot in Figure 6.11; i.e. the pileup events result in an independent random component added to the transverse missing energy in the calorimeter. This
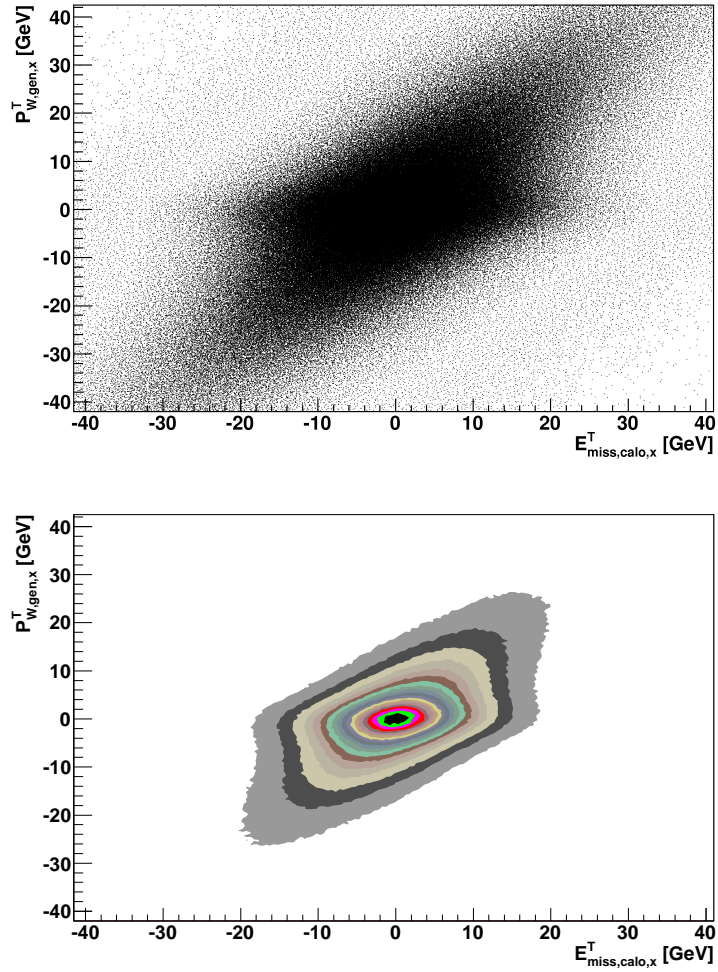
Figure 6.11: Both the scatter plot and the contour plot show the variables $P^T_{W,gen,x}$ and $E^T_{miss,calo,x}$. The distribution in the scatter plot shows a shape resembling a parallelogram; the contour plot suggests two independent contributions, one from the MET of the signal event and one from the MET from the pileup events.

random component dominantly affects lower values of missing transverse energy in the signal event.

For a similar investigation of the Z boson events one does not need to use Monte Carlo data, since the boson's transverse momentum can be reconstructed by both $E^T_{miss,calo}$ and the transverse momenta of the reconstructed muons. Similar to Figure 6.10, Figure 6.13 is a profile plot showing the average generator value of the x-component of the reconstructed muons, $< P^T_{muons\ added,x} >$, against the measured x-component of the calorimeter MET, $E^T_{miss,calo,x}$. For this plot, only Z boson events with exactly two reconstructed muons were used. The distribution shows the same features as the one in Figure 6.10; the pileup contribution is responsible for this effect, just like it is for the W boson events.

The data obtained from the Z events can be used as a calibration for $E^T_{miss,calo}$ in the W boson events. This calibration is given in Figure 6.14; on average, it provides a good measure of the W boson transverse momentum. Performing a linear fit one obtains a slope of 0.986. The slope will be used in subsection 6.4.3 as the systematic scale uncertainty of $E^T_{miss,calo}$.

6.4.2   At the Working Point

In this subsection, the principle of the reconstruction of the W boson mass with morphing method is demonstrated. The whole study has been performed with fast simulated events.

The selection cuts discussed in subsection 6.3.1 define the working point of the analysis that is used for determining the systematic uncertainties.

Weighting factors

The kinematic manipulation described in subsection 6.1.1 does not sufficiently predict the transverse W mass distribution from Z events, because there are additional differences between W and Z boson events:

- only in Z boson events both leptons can be reconstructed directly; in W boson events the only information available on neutrino is MET;

- a requirement for events in the Z sample is that both muons have to be reconstructed, while for W events this requirement only applies to one muon;

- a slight difference in the η and P^T distributions of the produced W and Z events;

- an irreducible contribution of Drell-Yan events produced via virtual photon exchange to the Z events;
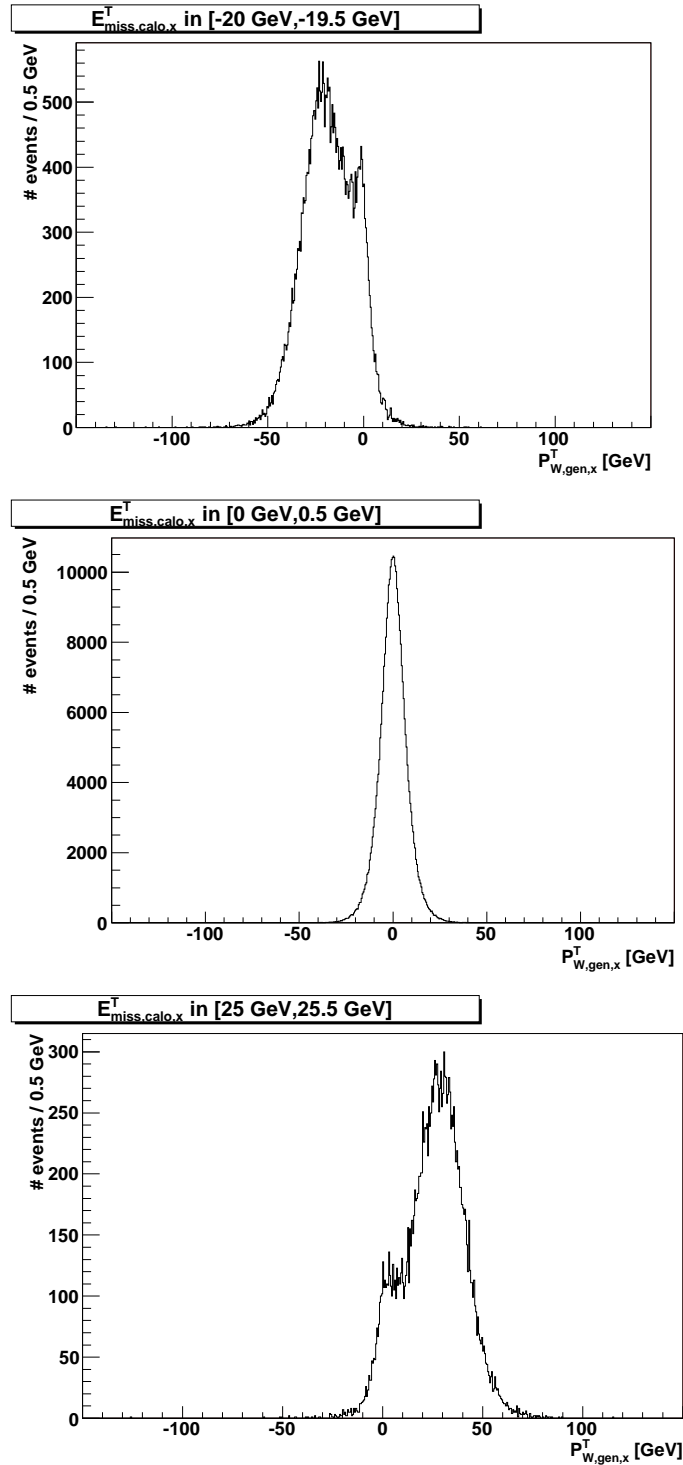
Figure 6.12: In the exemplary $E_{miss,calo,x}^T$ intervals of $[-20 \text{ GeV}, -19.5 \text{ GeV}]$, $[0 \text{ GeV}, 0.5 \text{ GeV}]$ and $[25 \text{ GeV}, 25.5 \text{ GeV}]$ the $P_{W,gen,x}^T$ distributions show peaks around the respective interval values; in addition, the distributions for $[-20 \text{ GeV}, -19.5 \text{ GeV}]$ and $[25 \text{ GeV}, 25.5 \text{ GeV}]$ have a second peak around 0 GeV. For the $[0 \text{ GeV}, 0.5 \text{ GeV}]$ interval the peaks overlap.
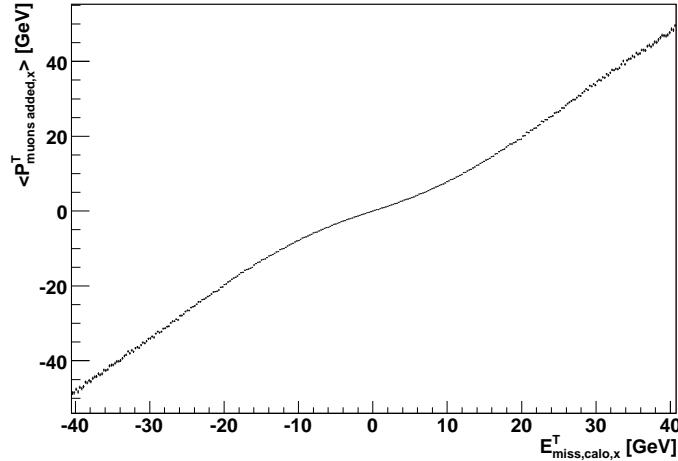
Figure 6.13: In this profile plot, the average x-component of the reconstructed muon momenta against the measured x-component of the calorimeter MET is given. Analog to 6.10, the slope in the region around 0 GeV is smaller than for $|E^T_{miss,calo,x}| > 20$ GeV. The bin width for $E^T_{miss,calo,x}$ is 0.25 GeV.

- a difference in final state radiation: both leptons can radiate in Z events, while in W events only the muon can.

Figure 6.15 shows the ratio of reconstructed distributions for transverse mass for transformed Z and W boson; the distributions have been normalized with respect to the number of events. Only the kinematic manipulations outlined in subsection 6.1.1 are used for the transformation; no additional reweighting is performed. A sequence of selection cuts is applied: selection cuts on momentum P^T, pseudo-rapidity η of the muon(s), recoil $|\vec{u}|$ for events generated with Pythia, and finally, all selection cuts (also including the selection cut on jets) for events simulated with the FAMOS software package. The most sensitive region for determining the mass is the area of the Jacobian edge; for low values the cuts have large effects, for high values (> 90 GeV) the statistics is rather low. Around the Jacobian edge, the normalized distributions differ up to 20% for the events simulated with the FAMOS software package with all selection cuts applied.

The transverse mass distributions of W events and morphed Z events are presented in Figure 6.16, both for events generated by Pythia (only requiring exactly one or two muons being reconstructed, respectively) and for events simulated with the fast detector simulation after all selection cuts. It is clearly visible how the use of the reconstructed MET smears out the Jacobian edge.
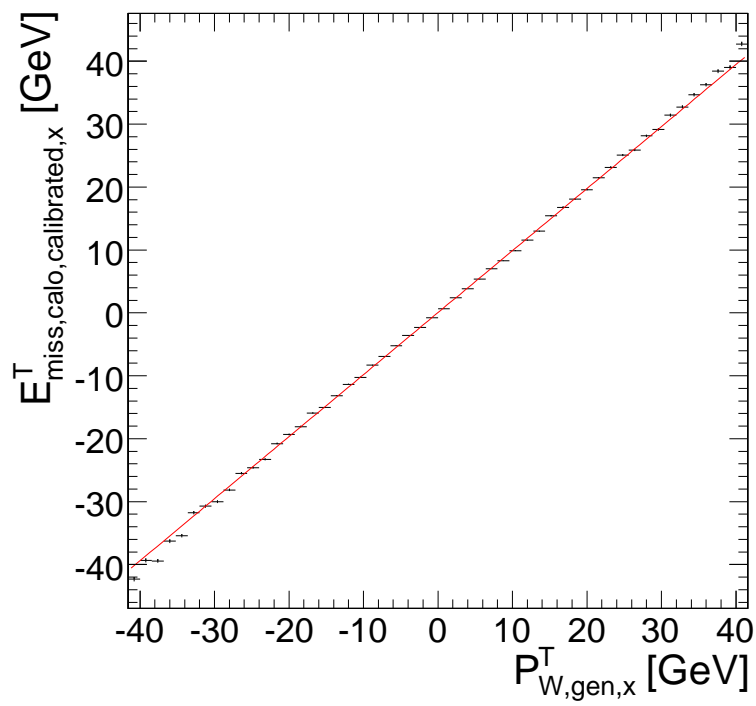
Figure 6.14: The calibrated x-component of the calorimeter MET as a function of the x-component of the W boson transverse momentum on the generator level shows a nearly linear correlation; the slope of the fitted line is 0.986, y-intercept is 0.0405 GeV.
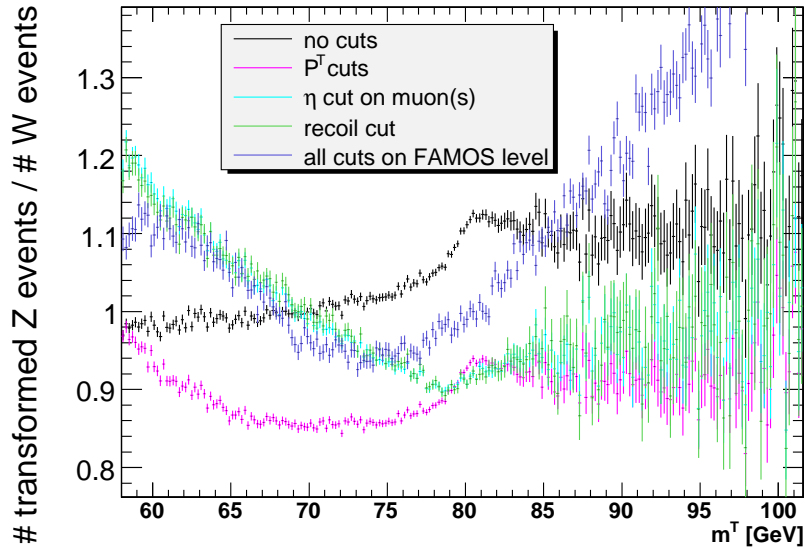
Figure 6.15: The ratios of normalized distributions in the transverse mass of W bosons and transformed Z bosons with sequential application of different cuts. The ratios were obtained by dividing the transverse mass distribution of morphed Z boson events by the transverse mass of the W boson events.
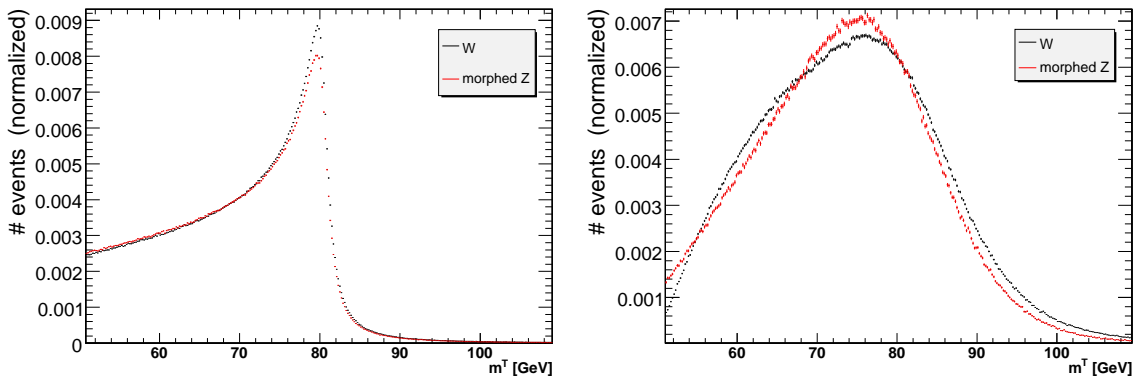
Figure 6.16: The left-hand distributions show the transverse mass of W events generated with Pythia (in black) and corresponding morphed Z bosons events (in red); only the selection cut on the number of muons has been applied. The right-hand distributions show the transverse masses of W events and morphed Z events, simulated with FAMOS and with all selection cuts applied.

Performing the mass fit

The ratios of the transverse mass distributions, simulated with the fast detector simulation software after applying selection cuts (see Figure 6.15), are used to obtain the re-weighting function, $w(m^T)$, that can be applied to the morphed Z events. The weight function incorporates all effects beyond the analytical transformations that are described in subsection 6.1.1. The coefficients are obtained from a fit of a fifth order polynomial to the calculated ratio of the transverse distributions.

The application of the weights gained from the re-weighting functions results in the transverse mass distributions of morphed Z boson events and W boson events.

In the following, the application of the morphing method is demonstrated and the statistical precision of the W mass measurement is determined. Therefore, Z boson events are morphed to different test masses M_W^{test}, using steps of 10 MeV for the mass. The weights obtained from the weight function $w(m^T)$ are applied to the morphed Z events. This transverse mass distribution is compared to the transverse mass distribution of the W boson events. A χ^2 criterion is used to determine the best fit value; hereby the compatibility of the two distributions is characterized. The χ^2 criterion is given by

$$\chi^2 = \sum_i \frac{(N_i^W - N_i^Z)^2}{\sigma_{i,W}^2 + \sigma_{i,Z}^2},$$

with i being the index for the bin number, N_i being the number of entries in the nth bin, and σ_i being the uncertainty of N_i.

As expected, the χ^2 values lie on a parabola; from this parabola the best-fit value is determined from its minimum, and the statistical precision is determined from its curvature at the minimum.

In Figure 6.17, χ^2 is shown versus the difference between M_W^{test} and the W boson mass in the Monte Carlo generator software, M_W, for the full Monte Carlo statistics. For each histogram bin, number of events and errors have been scaled to an integrated luminosity of 1 fb^{-1}. The χ^2 values of three neighboring histograms have been averaged.

Without re-scaling the integrated luminosity to 1 fb^{-1}, the absolute χ^2 value at the minimum is about the number of degrees of freedom.

With the minimum being at -4 MeV, the self-consistency of the morphing method has been demonstrated. The statistical resolution determined from the parabola is 39 MeV.

6.4.3   Systematic Uncertainties

In the following, several systematic uncertainties, such as muon momentum scale, background modelling, and angular offsets, are determined by varying the correspond-
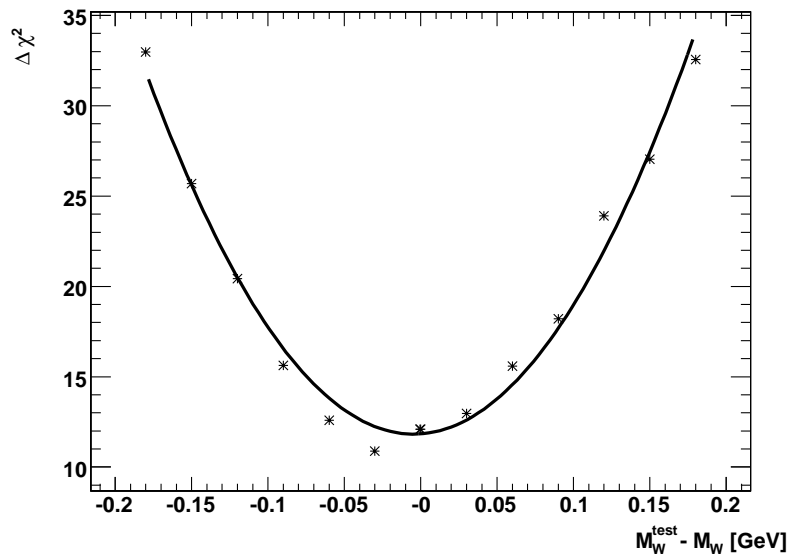
Figure 6.17: The $\Delta\chi^2$ distribution is computed by comparing the transverse distributions from morphed Z boson events and W boson events. M_W^{test} is the W boson test mass, M_W is the generator mass value for the W boson mass; the statistics has been scaled to an integrated luminosity of 1 fb^{-1}. The W boson mass determined with the method is 4 MeV lower than the actual W boson mass used in the simulation; the resolution is 39.0 MeV.
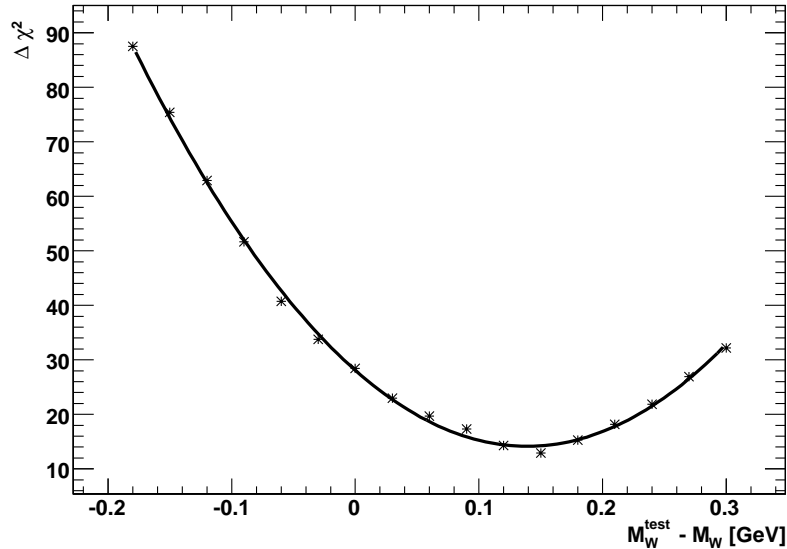
Figure 6.18: The χ^2 comparison for the muon P^T decreased by 1% has a best-fit value of 140 MeV.

ing observables around the working point and re-calculating the W boson mass. The systematic uncertainties are determined by following the guidelines established by the CMS collaboration; the guidelines are based on results given in [PTDR1].

Muon Momentum Scale and Resolution

The precision of the magnetic field mapping determines the muon momentum scale; the transverse mass is directly dependent on this scale. If the transverse momenta of the reconstructed muons are changed by the large value of $\pm 1\%$, the best-fit value is determined from the χ^2 parabola shifts by -136 MeV and 144 MeV (see Figure 6.18), respectively. This corresponds on average to 0.174% of the W mass and shows how effects between Z and W data samples are mainly canceled out by the morphing method.

For a realistic precision of 0.1%, the systematic uncertainty is only 14 MeV.

In addition, the dependency of the W mass reconstruction on the description of the muon momentum resolution has to be determined. For this, an additional Gaussian smearing of $7.4 \cdot 10^{-5} \frac{1}{\text{GeV}}$, which corresponds to 10% of the RMS resolution, is applied to the inverse reconstructed muon momenta. This results in an uncertainty of 30 MeV.

Angular Offsets And Resolution

The spatial muon reconstruction resolution, which also affects the quality of the W mass measurement, can be studied by systematic shifts of the reconstructed values of the angle θ and the pseudo-rapidity η of the muons.

At first, the muon θ resolution, with an RMS of $\sigma_\theta = 4 \cdot 10^{-4}$, is increased by 10% for all reconstructed muons by applying an additional smearing. This only leads to a small effect of 3 MeV for the reconstructed W mass.

Displacements of the luminous region of the beams with respect to the center of the detector could cause a systematic shift of the reconstructed θ. Therefore, a systematic shift of θ by one σ_θ is used, which leads to an effect of 19 MeV for the reconstructed W mass.

For the pseudo-rapidity η, a shift in the boundaries of the acceptance region by the resolution of η, $\sigma_\eta = 6 \cdot 10^{-3}$, results in an uncertainty of the W mass of 19 MeV. The expansion or reduction of the η acceptance region by σ_η results in an uncertainty of 17 GeV.

Nonlinearities in the momentum scale

Nonlinearities in the momentum or in the energy scale belong to the group of systematic uncertainties that do not cancel out in the morphing and scaling methods.

Using the Z boson sample, the lepton momentum scale can be fixed very well at $\frac{M_Z}{2}$. Studying samples with special decay topologies makes it possible to check the momentum scale at low momenta.

A simple parametrization for the nonlinearity in the energy scale about the Jacobian edge is given by

$$E^{T\prime} = E^T \left(1 + \epsilon(E^T - \frac{M_z}{2}) \right),$$

as it was used for electrons in [PhysJG]. With a nonlinearity parameter of $\epsilon = 2 \cdot 10^{-5} \frac{1}{\text{GeV}}$, the effect on the W mass in the electronic decay channel is about 10 MeV.

As the transverse mass mainly depends on the track measurement of the muons, which is proportional to $1/P^T$ in the magnetic field of the detector, nonlinearities in the momentum scale for muons are expected to be insignificantly small.

Calorimeter MET Scale and Resolution

In Figure 6.14, it is shown that the calibration of the missing transverse energy provides on average a good measurement of the transverse momentum of the W boson. The fitted slope of 0.986 differs from the perfect case of 1.0 by 1.4%. Based on this, a conservative estimate of 2% as the systematic scale uncertainty of $E^T_{miss,calo}$ is used.

By changing $E^T_{miss,calo}$ by $\pm2\%$, the sensitivity of the method to the calorimeter MET scale is tested; it was found that the χ^2 minimum is shifted by ±38 MeV. Because of the cut on the hadronic recoil, the effect on the M_W is small in comparison to the scale uncertainty. The selection cut makes sure that the transverse mass is mainly affected by the muon transverse momentum; this can be seen when formula (2.27) is rewritten as

$$m^T = \sqrt{2P^T_\mu(E^T_{miss,calo} - P^T_\mu)(1 - \cos(P^T_\mu, E^T_{miss}))}.$$

The modelling of the resolution in $E^T_{miss,calo}$ is expected to have significant effects. The resolution of $E^T_{miss,calo}$ can be obtained by comparing the measured $E^T_{miss,calo}$ with the sum of reconstructed muons; this is illustrated in Figure 6.19. It differs by about 6% from the resolution of $E^T_{miss,calo}$ in W boson events. This difference is due to W boson decays with the transverse energy of the radiated photon(s) from the muon being measured in the calorimeter. Most of this difference is likely be understood, so a systematic error of 5% on the modelling of the resolution in $E^T_{miss,calo}$ can be seen as a conservative approximation. By increasing the difference between reconstructed $E^T_{miss,calo}$ and true $E^T_{miss,calo}$ for both x and y components, the reconstructed W mass is shifted by 30 MeV.

W Boson Width

The W width is a parameter used in the morphing method (see step 2 in the description of the method in subsection 6.1.1). In order to test the dependency of the method on the uncertainty of the W boson width Γ_W, the width in the morphing method is increased/decreased by its experimental uncertainty [PDG]. The result is an effect of ±10 MeV on the reconstructed W mass.

Background Modelling

The most important background to the W boson events comes from Z boson events with only one reconstructed muon. The effects of over- and underestimation of the background can be estimated by varying the number of background events from this background without the weights being changed. Both background over- and underestimation result in 4 MeV shifts of the best fit value in the χ^2 parabola for the W mass.

Alignment of the Early Detector

During the first phase of data taking, the alignment of the detector is significantly less understood than in later phases; this leads to a resolution in the transverse momentum
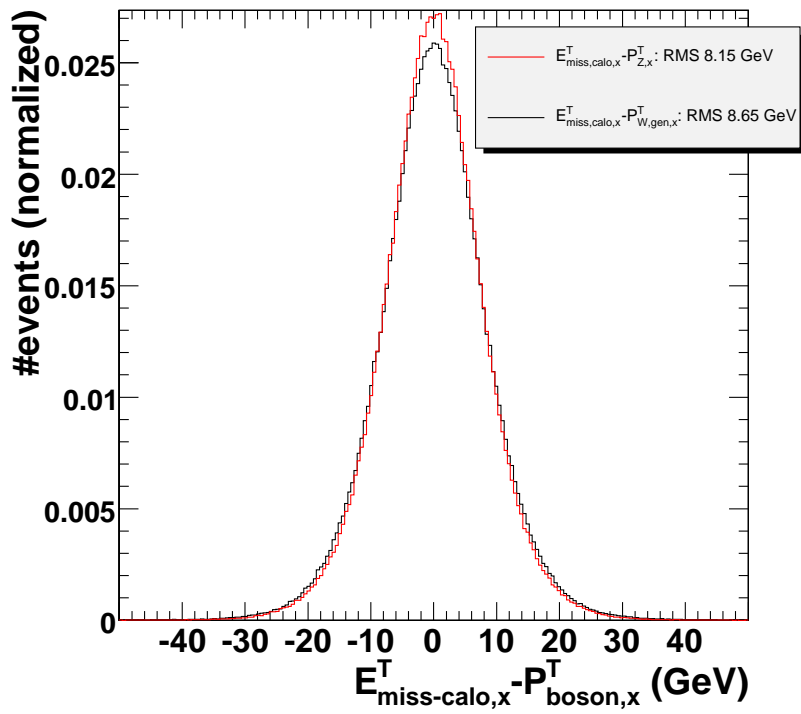
Figure 6.19: Distributions of $E^T_{miss,calo,x} - P^T_{Z,x}$ (P^T_Z reconstructed from the muons) for Z boson events and $E^T_{miss,calo,x} - P^T_{W,gen,x}$ for W boson events after all selection cuts. The width for Z boson events is 6.1% smaller than the width for W boson events.

which is two times worse (see Figure 9.12 in [PTDR1]) in comparison to the "perfectly aligned detector" used by the fast simulation software. The effect of the large uncertainties with the early detector is simulated by applying an additional smearing to $1/P^T$ of the muons of all W and Z events in the fast simulated sample. This leads to a W boson mass resolution for the early detector of 40.8 MeV, instead of 39.0 MeV for the perfectly aligned detector. Thereby, the additional uncertainty of the W boson mass due to the alignment uncertainties is estimated to be 12 MeV.

Parton Distribution Functions

<u>P</u>arton <u>d</u>istribution <u>f</u>unctions (PDF) describe the probability density for finding a parton in a hadron as a function of the fraction x of the proton's momentum carried by this parton. The knowledge on the PDFs is limited, resulting in an uncertainty for the distributions of the observables and on the acceptance of the events.

The CTEQ61 [Pum] set of PDFs has a central set ($s_i = 0$) and forty PDF members, $F^{\pm} = F(x, Q^2; s_i^{\pm})$) ($i = 1, \ldots, 20$), with Q^2 being the momentum transfer. The later represent the PDF set with the i-th independent parameter of the set being changed by $\pm 1\sigma$. The effect of the PDF uncertainties is investigated by changing the PDF subset used for determining the reweighting function.

The effect on the W mass is calculated by the "master equation" [Nad], given by

$$\Delta m_W^+ = \sqrt{\sum_{i=1}^{20} \left[\max\left(m_W(s_i^+) - m_W(0), m_W(s_i^-) - m_W(0), 0\right)\right]^2},$$

$$\Delta m_W^- = \sqrt{\sum_{i=1}^{20} \left[\max\left(m_W(0) - m_W(s_i^+), m_W(0) - m_W(s_i^-), 0\right)\right]^2},$$

with $m_W(s_i^{\pm})$ being the best fit value for the W mass using the PDF set with i-th parameter changed by $\pm 1\sigma$.

The resulting uncertainty is

$$\begin{aligned} \Delta m_W^+ &= 26 \text{ MeV}, \\ \Delta m_W^- &= 21 \text{ MeV}. \end{aligned}$$

Summary

The systematic effects discussed in this subsection are summarized in Table 6.6. The statistical uncertainty of the morphing method is

$$\Delta m_W^{stat} = 39 \text{ MeV},$$

the systematic uncertainty calculated from the effects discussed in this section is

$$\Delta m_W^{sys} = 73 \text{ MeV}.$$

There will be further necessary theoretical and experimental studies on the systematic uncertainties, e.g. on the influence of higher order radiative effects, since Pythia uses first-order photon radiation only; for example, a more in-depth simulation of photon radiation is incorporated in Photos [Photos].

The remaining effects can be most likely brought under control.

source of effect and size variation	shift of reconstructed W mass	10 MeV effect on m_W
background change by 10%	4 MeV	25%
muon momentum scale by 0.1%	14 MeV	0.07%
muon $1/P^T$ resolution smeared by 10%	30 MeV	3%
nonlinearities in muon momentum scale	expected to be negligible	-
muon θ resolution smeared by 10%	3 MeV	30%
systematic shift in muon $\theta \pm$ resolution	19 MeV	$0.5\sigma_\theta$
systematic shift in muon $\eta \pm$ resolution	19 MeV	$0.5\ \sigma_\eta$
expansion of η acceptance $\pm$ resolution	17 MeV	$0.6\ \sigma_\eta$
calorimeter MET scale by 2%	38 MeV	0.5%
calorimeter MET resolution by 5%	30 MeV	1.7%
W width $\pm 1\sigma_{\Gamma_W}$	10 MeV	$1\sigma_{\Gamma_W}$
detector alignment for 1 fb^{-1}	12 MeV	
PDF errors	24 MeV	
systematic uncertainty	**73 MeV**	
statistical uncertainty	**39 MeV**	

Table 6.6: This table summarizes the effects of the systematic uncertainties of the morphing method studied for an integrated luminosity of 1 fb^{-1}; the last column lists the precision needed for restricting the respective systematic uncertainty on the W mass to ± 10 MeV. The last two lines summarize the statistical and the systematic uncertainty.

6.5 Reconstruction of W Boson Mass with the Scaling Method

6.5.1 Dependence of R(X) on Cuts

In the scaling method (its concept has been explained in subsection 6.1.2), the variable R(X) scales the differences in the theory of W and Z boson decays. In the analysis of experimental data, further differences occur because of the restricted resolution of the detector.

In Figure 6.20, the ratio R(X) is presented for different selection criteria for the events on the generator level. If events are only required to have one or two reconstructed muons, R(X) is within 5% of 1.0. The pseudo-rapidity requirement for the reconstructed muon(s) shows the largest effect, since there is no η requirement for the missing transverse energy.

6.5.2 At the Working Point

After applying all selection cuts, the ratios of the scaled muon transverse momentum distributions on FAMOS level are used for calculating R(X) (see Figure 6.21); to cancel out statistical effects, a fifth order polynomial is fitted to the R(X) distribution. Then, the R(X) distributions are calculated from the scaled muon transverse momentum distributions for different W boson mass test values, M_W^{test}. These distributions are compared to the original R(X) distribution (see Figure 6.22). Like in the scaling method, a χ^2 criterion is used in order to determine the best fit value.

In Figure 6.23, the difference in χ^2 is given versus the difference between M_W^{test} and the W boson mass on the generator level, M_W, for the full available Monte Carlo statistics; number of events and errors have been scaled to an integrated luminosity of 1 fb^{-1} (without this scaling, the absolute χ^2 value at the minimum is approximately equaling the number of degrees of freedom). The χ^2 values of three neighboring histograms have been averaged for this distribution. The minimum is situated at +1 MeV, the statistical resolution is $\pm$29 MeV.

6.5.3 Systematic Uncertainties

Muon Momentum Scale and Resolution

By changing the transverse momenta of the reconstructed muons by 0.1%, over- and underreconstruction of the transverse momentum of the muon are studied. The resulting uncertainty is 10 MeV.

The dependency of the reconstructed W boson mass on the muon momentum resolution is tested by adding an additional smearing of 10% of the RMS resolution
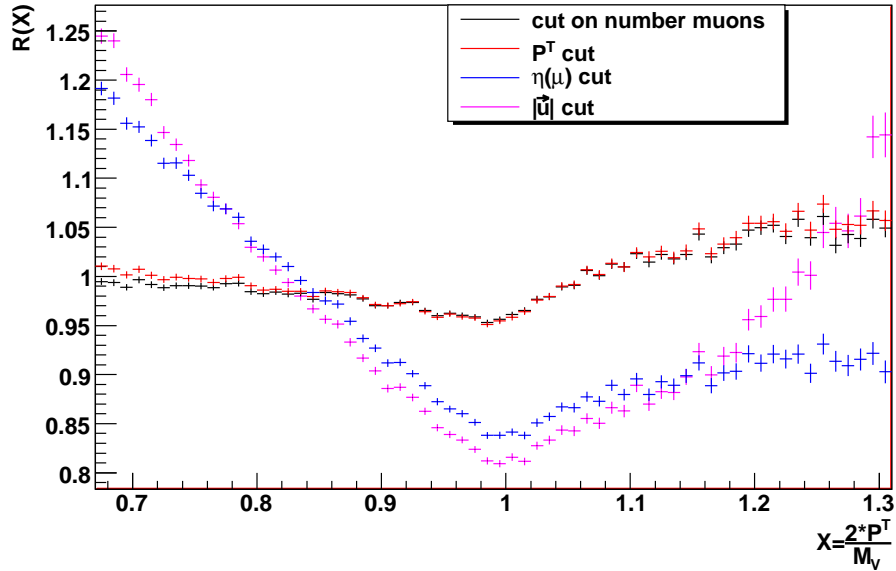
Figure 6.20: The ratios of the scaled transverse muon momentum for W and Z boson events (M_V is the respective vector boson mass). If only the selection cut on the number of muons is applied, the ratio is very close to 1.0 for the scaled variable in the range from 0.7 to 1.3. The selection cuts on the transverse momentum of the muons for Z events and on muon P^T and MET for W boson events change the ratios only slightly. The restricted angle for pseudo-rapidity η of the muon(s) has a clear impact on the ratios, while the additional selection cut on the recoil, $|\vec{u}|$, has mainly an effect for ratios $X > 1.25$.
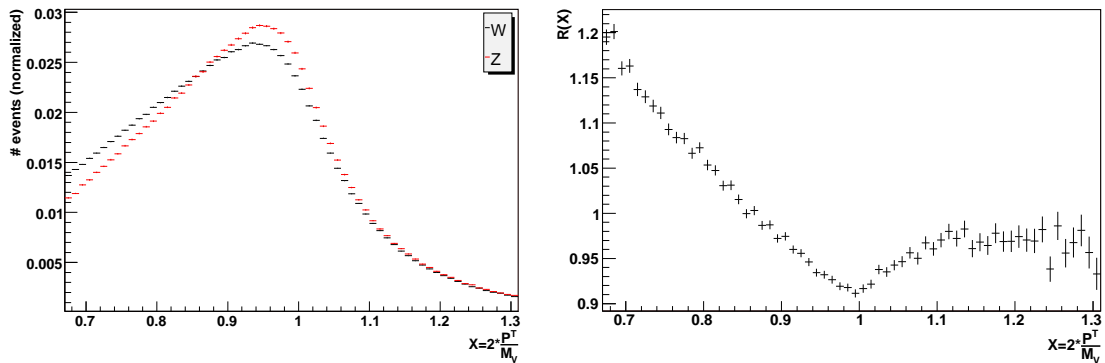
Figure 6.21: Left: the scaled muon momentum distributions for both W and Z boson events after all selection cuts have been applied. Right: the R(X) distribution calculated from the scaled muon momenta.
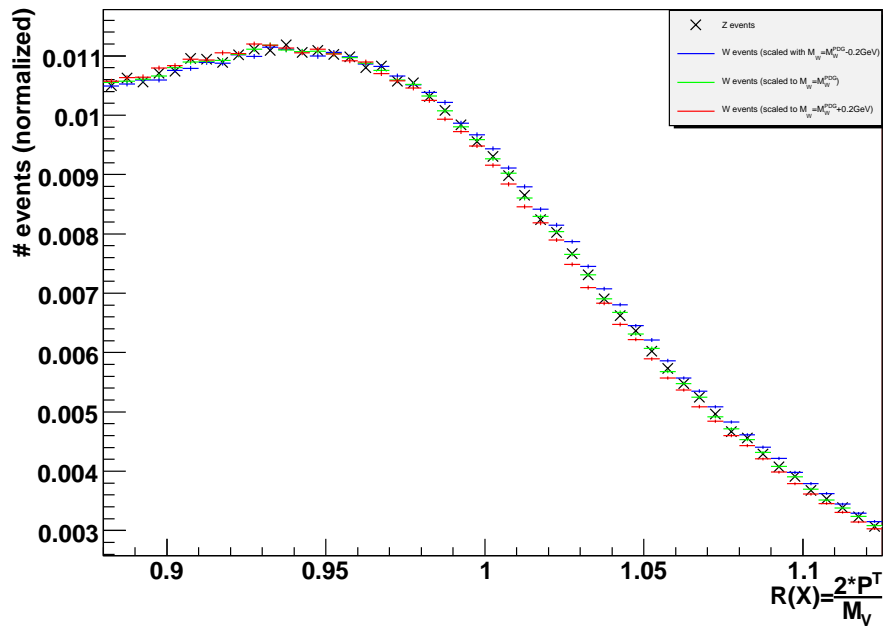
Figure 6.22: The scaled muon momentum distribution from Z boson events is compared to the scaled muon momentum distribution from W boson events for three exemplary W boson test masses.
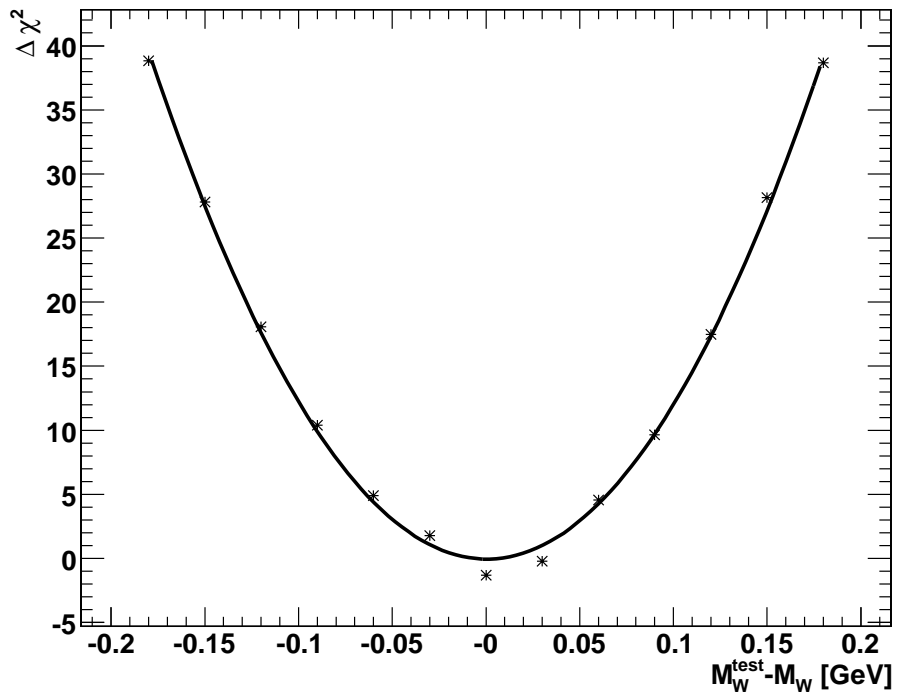
Figure 6.23: The $\Delta\chi^2$ distribution for the scaling method at the working point has been determined by comparing scaled muon P^T distributions for Z boson events and W boson events using different test mass values M_W^{test}. M_W is the generator mass value for the W boson mass; the statistics has been scaled to an integrated luminosity of 1 fb^{-1}. The minimum of the parabola is at +1 MeV; the resolution is computed from the parabola to be $\pm$29.2 MeV.

to the inverse reconstructed muon momenta. The uncertainty is 9 MeV.

Angular Offsets and Resolution

For the muon θ, the resolution is increased by 10% of the RMS and the angle itself is shifted by σ_θ. The uncertainties of these effects are 4 MeV and 13 MeV, respectively.

For the pseudo-rapidity of the muon, a shift of the boundaries of the acceptance region and expansion/reduction of the acceptance region by σ_η have been investigated. The resulting uncertainties are 17 MeV and 14 MeV, respectively.

Nonlinearities in the Momentum Scale

As discussed on page 93, the nonlinearities in the momentum scale for the muons are expected to be insignificantly small.

Calorimeter MET Scale and Resolution

The sensitivity of the scaling method to the calorimeter MET scale is tested by changing $E_{miss,calo}^T$ by $\pm 2\%$. This results in an uncertainty of 14 MeV.

The modelling of the missing transverse energy in the calorimeter is tested by assuming a systematic error of 5% on the modelling of the resolution of $E_{miss,calo}^T$. The effect is 10 MeV on the W boson mass.

W Width

The dependency of the W boson mass measurement on the W boson width is tested by using an R(X) function, which has been calculated by using W boson events with the width increased/decreased by the experimental uncertainty [PDG]. The resulting uncertainty is 14 MeV.

Alignment of the Early Detector

For the early phase of data taking, the detector alignment will not be perfectly understood. The effect on the W mass measurement is tested by applying an additional smearing to the reconstructed inverse muon transverse momenta (simulating an early detector effect described in [PTDR1]). Since the W mass resolution for the early detector is 31.2 MeV instead of 29.2 MeV for the perfectly aligned detector, the approximation for the uncertainty of the W boson mass is 11 MeV.

Background Modelling

The systematic uncertainty resulting from the misestimation of the background is investigated by changing the number of events in the main background for W boson events by $\pm 10\%$. This uncertainty is 12 MeV.

PDFs

By varying the independent parameters and using the master equation (see page 96), the PDF uncertainty is determined to be

$$
\begin{aligned}
\Delta m_W^+ &= 23 \text{ MeV}, \\
\Delta m_W^- &= 19 \text{ MeV}.
\end{aligned}
$$

Transverse Momentum Spectrum of the W Boson

Measuring the W boson mass with the scaling method depends on the precision of the knowledge on the transverse momentum distribution of the W boson. This uncertainty can be quantified as the uncertainty associated with the theoretical prediction of $R(X)$ for the scaled transverse momentum due to soft gluon emission. (The transverse mass distribution has only small radiative corrections and, therefore, is only slightly sensitive to the transverse momentum spectrum of the W boson [SNV].) The dependence of the NLO prediction on the choice of renormalization and factorization scale using the DYRAD program [GGK] was studied in order to approximate the resulting uncertainty for the W boson measurement. The effect on the W boson measurement with the scaling method for the electron channel is given in [PhysJG]. The resulting uncertainty is 30 MeV, which can also be used as the respective uncertainty for the muon channel.

Summary

The systematic effects discussed in this subsection are summarized in Table 6.7. The statistical uncertainty of the scaling method is

$$
\Delta m_W^{stat} = 29 \text{ MeV},
$$

the systematic uncertainty calculated from the effects discussed in this subsection is

$$
\Delta m_W^{sys} = 54 \text{ MeV}.
$$

For other systematic effects, the remarks from the summary on the morphing method on page 96 apply.

source of effect and size variation	shift of reconstructed W mass	10 MeV effect on $m_{\rm W}$
background change by 10%	12 MeV	8%
muon momentum scale by 0.1%	10 MeV	0.1%
muon $1/P^T$ resolution smeared by 10%	9 MeV	11%
nonlinearities in muon momentum scale	expected to be negligible	-
muon θ resolution smeared by 10%	4 MeV	25%
systematic shift in muon θ $\pm$ resolution	13 MeV	0.8 σ_η
systematic shift in muon η $\pm$ resolution	17 MeV	0.6 σ_η
expansion of η acceptance $\pm$ resolution	14 MeV	0.7 σ_η
calorimeter MET scale by 2%	14 MeV	1.4%
calorimeter MET resolution by 5%	10 MeV	5%
W width $\pm 1\sigma_{\Gamma_{\rm W}}$	14 MeV	0.7$\sigma_{\Gamma_{\rm W}}$
detector alignment for 1 fb^{-1}	11 MeV	
PDF errors	21 MeV	
$P^T(W)$ Spectrum	30 MeV	
systematic uncertainty	**54 MeV**	
statistical uncertainty	**29 MeV**	

Table 6.7: This table summarizes the effects of the systematic uncertainties of the scaling method studied for an integrated luminosity of 1 fb^{-1}; the last column lists the precision needed for restricting the respective systematic error on the W mass to ± 10 MeV. The last two lines summarize the statistical and the systematic uncertainty.

method	statistical uncertainty	systematic uncertainty
morphing method	39 MeV	73 MeV
scaling method	29 MeV	54 MeV

Table 6.8: Summary of the statistical and systematic uncertainties for the morphing method and the scaling method for an integrated luminosity of one inverse femtobarn.

6.6 Comparison of the Results and Outlook

The two methods provide different statistical uncertainties for the W mass, because the transverse momentum of the muon has a higher precision than the transverse mass (see Table 6.8). The transverse mass is calculated from the transverse momentum of the muon and from the missing transverse energy, with the latter having a low resolution.

In the systematic uncertainties, the main differences can be explained by the different approaches the methods have. For the morphing method, the systematic uncertainty due to the calorimeter MET resolution is much higher than for the scaling method. The MET is used in the selection cuts and in calculating the transverse mass in the morphing method, while for the scaling method the MET is only used in the selection cuts.

The transverse mass distribution has small radiative corrections and, therefore, is only slightly sensitive to the $P^T(W)$ spectrum. But in the scaling method for the muon transverse momentum the uncertainty is approximated with 30 MeV.

In [PhysJG], the scaling method is also applied to the electron transverse momentum. The systematic uncertainties are compatible with the ones presented in this thesis for the muon transverse momentum; the statistical uncertainty is lower for the decay into muons due to a higher selection efficiency.

For both analysis methods presented in this thesis, the statistical and systematic uncertainties were studied for an integrated luminosity of one inverse femtobarn. The uncertainties presented will be only achievable with a fully functional detector; this might not be the case for the first inverse femtobarn of data taken.

With a growing integrated luminosity, not only the statistical uncertainty will become smaller but also the systematic effects will be understood better and, therefore, will become smaller. For the scaling method, the systematic error resulting from the transverse mass spectrum of the W boson will go down with the availability of further theoretical calculations.

In order to obtain a high precision measurement of the W boson mass, a combination of different methods for the measurement needs to be applied to the data taken

by the CMS experiment and the ATLAS experiment.

Chapter 7

Conclusions and Outlook

Two methods for measuring the W boson mass with the CMS detector have been presented in this thesis. Both methods use similarities between W boson and Z boson decays. Their statistical and systematic precisions have been determined for $W \to \mu\nu$; the statistics corresponds to one inverse femtobarn of data.

A large number of events needed to be simulated for this analysis; it was not possible to use the full simulation software because of the enormous computing time which would have been needed. Instead, a fast simulation tool for the CMS detector was used. Still, the computing requirements for the fast simulation exceeded the capacity of the local compute cluster.

Since the data taken and processed at the LHC will be extremely large, the LHC experiments rely on the emerging grid computing tools. The computing capabilities of the grid have been used for simulating all physics events needed for this thesis. To achieve this, the local compute cluster had to be integrated into the grid and the administration of the grid components had to be secured. As this was the first installation of its kind, several contributions to grid training events could be made: courses on grid installation, administration and grid-enabled applications were given.

The two methods for the W mass measurement are the morphing method and the scaling method. The morphing method relies on an analytical transformation of Z boson events into W boson events and determines the W boson mass by comparing the transverse mass distributions; the scaling method relies on scaled observables from W boson and Z boson events, e.g. the transverse muon momentum as studied in this thesis. In both cases, a re-weighting technique applied to Monte Carlo generated events is used to take into account different selection cuts, detector acceptances, and differences in production and decay of W boson and Z boson events.

The statistical resolution of the scaling method, $\Delta M_{W,stat.} = 29$ MeV, is better than the resolution of the morphing method, $\Delta M_{W,stat.} = 39$ MeV, since the transverse momentum has a higher experimental precision than the transverse mass, which is

diluted by the low resolution of the missing transverse energy.

The main contributions to the systematic uncertainty of $\Delta M_{W,sys.} = 73$ MeV in the morphing method result from the calorimeter MET resolution, which is low and biased by pileup events. In the scaling method, the main contribution to the systematic uncertainty of $\Delta M_{W,sys.} = 54$ MeV arises from the uncertainty on the transverse momentum spectrum of the W boson, which can be decreased by NNLO calculations.

A high precision measurement of the W boson mass at the LHC will require a thorough understanding of the detectors, in order to constrain the systematic effects, and a combination of several analysis methods.

Appendix A

Job Description Language

In the gLite middleware, the <u>J</u>ob <u>D</u>escription <u>L</u>anguage (JDL, [JDL]) is used for specifying the requirements of a grid job. In the JDL file, each requirement must be stated in the format `attribute=expression`.

A standard JDL file has the form:

```
Executable = "/bin/executable_name";
StdOutput = "std.out";
StdError = "std.err";
InputSandbox = {"inputfile1","inputfile2"};
OutputSandbox = {"outputfile1","outputfile2"};
```

- The only attribute that is required in a JDL file is `Executable`, which defines an executable file already installed on the Worker Node or an executable file sent along with the job in the input sandbox. Usually, the executable file is a shell script.

- If the standard output of a grid job has to be redirected to a file, the name of this file needs to be specified in the attribute `StdOutput`. The same applies to the standard error, the respective attribute being `StdError`.

- A user can send files along with the job in the input sandbox; the respective attribute is `InputSandbox`. The maximum size for the input sandbox is 10 MB. If larger files are needed for the job, they have to be put on a Storage Element beforehand, where they can be retrieved by the job.

- In order to get output files from a job, the according files have to be specified in the attribute `OutputSandbox`. Usually, the output sandbox contains user specific files as well as the files stated for the standard output and the standard error.

Often users have specific requirements for the software installed on the remote site or for the minimum CPU time available for their jobs. These requirements, and many others, can be specified using the attribute `Requirements`. The most important expressions are:

- `other.GlueCEUniqueID`: This expression allows to choose specific batch system queues or specific Computing Elements; regular expressions can be used. The short queue at the IEKP grid site can be specified by
`other.GlueCEUniqueID==ekp-lcg-ce.physik.uni-karlsruhe.de:`
`2119/jobmanager-pbs-short`.

- `other.GlueCEPolicyMaxWallClockTime`: It allows to specify actual running time (in minutes) on a Worker Node available to a grid job, e.g.
`other.GlueCEPolicyMaxWallClockTime>1440` for one day.

- Grid sites publish tags for the software components preinstalled on their machines. This is important for users who need specific software to be available on the grid site, e.g. simulation software. An example expression is
`Member("VO-cms-CMSSW_1_7_1",other.`
`GlueHostApplicationSoftwareRunTimeEnvironment)`, indicating that version 1.7.1 of the CMS software package CMSSW is required.

Requirements can be combined by using Boolean expressions; some requirements allow the use of regular expressions.

In the JDL file, several types of jobs can be specified. Besides the standard job described above, the most important ones are: interactive jobs, collection jobs (allowing submission of several jobs using a single JDL file), and <u>D</u>irect <u>A</u>cyclic <u>G</u>raph (DAG) jobs, which allow a simple workflow model.

Appendix B

Grid Monitoring Tools

Detailed monitoring is essential for grid computing; it is needed for both local computer clusters and grid sites. There are several grid monitoring tools available; three of them are described in the following.

- The Service Availability Monitor (SAM, [SAM]) is a highly configurable tool for grid monitoring. Its database system allows to choose different sets of tests (e.g. tests of specific grid components, tests of software tags) depending on the purpose of the monitoring. SAM can be used for site wide, VO wide or federation wide tests. The results of the tests are published on a web page, with users being able to query for specific data.

- The CMS dashboard ([CMSD]) provides a single entry point for monitoring data collected from the CMS grid sites. It works for both gLite and Open Science Grid middleware systems. The dashboard monitors CMS grid computing with respect to quantities (e.g. jobs per site, per user, per data collection), use of resources (e.g. CPU, memory, I/O rates), success or failure of jobs, and behavior of CMS applications. Just as SAM, the results can be queried via a web page.

- A prototype of a special monitoring tool for datasets has been developed at the University of Karlsruhe [Pos]. Contributions to this prototype have been made in the context of this thesis. The tool tests grid sites on their capabilities to perform the whole data analysis workflow; the workflow includes using the CMS software CRAB and accessing CMS datasets stored on the respective site. A site is considered to be fully functional if a test job finishes successfully within a specified time. The results of the monitoring are published in a daily format (see Figure B.1) and in a weekly format.
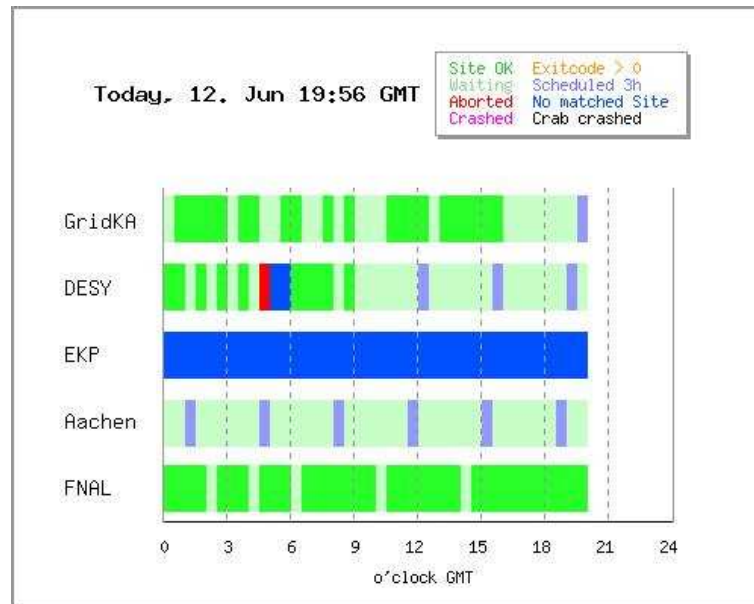
Figure B.1: This graphical summary is an example for the test results from the dataset monitoring. The IEKP website was on a scheduled downtime due to the redesign of the grid cluster and therefore did not have any successful test jobs. [Pos]

Appendix C

Important User Commands for the gLite Middleware

The gLite middleware, which is used in the LCG, has been described in section 4.4. In the following, user commands for authentication and authorization, job handling, and data management are summarized; a more extensive description can be found in [gLUG].

C.1   Authentication and Authorization

The gLite middleware uses proxies for authentication and authorization of users and services.

C.1.1   Proxy Initialization

As a first step in using grid resources, the user creates a personal proxy. The respective command is

```
voms-proxy-init [-voms <VO name>] [-valid hh:mm] [-vomslife hh:mm]
```

This command asks the user for the grid passphrase. The proxy is locally stored in the \tmp directory.

- Without the optional parameter -voms, the command only performs the authentication. Using -voms, the VOMS of the respective VO is contacted and the user is authorized. (This allows the user to be in different VOs at the same time; also the user is able to have different roles in these VOs, which are described later in this section.)

- The authorization is an extension of the authentication part of the proxy. Therefore, different life times for the proxy itself and for its VOMS extension can be specified via `-valid` and `-vomslife`, respectively. The default value for both life times is 12 hours.

In production environments users have different tasks. To fulfill them the users need special rights and permissions. On the grid, these rights and permissions are represented by user groups and user roles within a VO. They are managed by the VOMS. In order to create a proxy with a certain user authorization, the parameter `-voms` has an extended form:

```
-voms <VO name>:/<group name>[/Role=<role name>]
```

For example, the German CMS users have a special user group, which can be accessed with `-voms cms:/cms/dcms`, while the CMS Monte Carlo production manager role can be adopted by authorized users via `-voms cms:/cms/Role=cmsprod`.

C.1.2 Proxy Information

In order to get information on an already existing proxy, a user can execute the following command:

`voms-proxy-info [-all]`.

Used without parameters, the command returns information on the proxy only. The parameter `-all` adds this information. An example output is

```
>voms-proxy-info -all
subject   : /O=GermanGrid/OU=FZK/CN=Christopher Jung/CN=proxy
issuer    : /O=GermanGrid/OU=FZK/CN=Christopher Jung
identity  : /O=GermanGrid/OU=FZK/CN=Christopher Jung
type      : proxy
strength  : 512 bits
path      : /tmp/x509up_u4413
timeleft  : 11:54:09
=== VO cms extension information ===
VO        : cms
subject   : /O=GermanGrid/OU=FZK/CN=Christopher Jung
issuer    : /DC=ch/DC=cern/OU=computers/CN=lcg-voms.cern.ch
attribute : /cms/dcms/Role=NULL/Capability=NULL
attribute : /cms/Role=NULL/Capability=NULL
attribute : /cms/production/Role=NULL/Capability=NULL
attribute : /cms/analysis/Role=NULL/Capability=NULL
attribute : /cms/uscms/Role=NULL/Capability=NULL
timeleft  : 11:54:09
```

C.1.3 Deleting a proxy

A user's proxy can be deleted by using the following command:

```
voms-proxy-destroy
```

It should be used with care, as all the jobs using this proxy will fail automatically.

C.2 Job Handling

The use of the Job Description Language has been already described in appendix A; the necessary commands for queries on computing resources, for job submission, and for output retrieval will be explained in the following subsections.

In the latest versions of gLite the Resource Broker has been phased out and replaced by the Workload Management System (WMS). Therefore, only job submission commands for the WMS are discussed.

C.2.1 Job Submission

The job submission is invoked by the following gLite command:

```
glite-wms-job-submit <-a|-d <delegation_id>> [-o <job_id_file>] \
   [-r <CE>] <jdl_file>
```

- The command `glite-wms-job-submit` requires a delegation proxy that is either stated directly by passing its identification (id), `-d <delegation_id>`, or that is automatically generated at the time of the job submission by using the option `-a`. Since the delegation requires a non-negligible amount of time, the former is advised for a better performance.

- The option `-o` is highly advised for a better overview on submitted jobs; it logs the job identifiers, which have the format `https://<LB_host>[:port]/<unique-string>`, in the file `<job_id_file>`. Without knowing the identifier of a job, the job cannot be accessed.

- Sometimes a user wants or needs to send his/her jobs to a certain CE (e.g. for testing a specific grid site); for this, the option `-r <CE>` can be used.

- The JDL file `jdl_file` has to be correct in syntax, otherwise the job submission will fail. Common errors include missing semicolons and the use of incorrect quotation marks.

The job submission command returns information on the WMS used for job submission and on the job identifier given to the job submitted. All this information is given on the standard output; is might look like this:

```
> glite-wms-job-submit -a -o myJobIds.id job.jdl

Connecting to the service https://wms102.cern.ch:7443/glite_wms_wmproxy_server


==================== glite-wms-job-submit Success ====================

The job has been successfully submitted to the WMProxy
Your job identifier is:

https://lb103.cern.ch:9000/gzPu2Mdz2tSOux2bevSfmA

The job identifier has been saved in the following file:
/afs/cern.ch/user/c/cjung/myJobIds.id


==========================================================================
```

The `https://`... identifier is needed for the job information command, which is explained in the following subsection, and for the retrieval of the output sandbox (see subsection C.2.3).

Sometimes it is of interest to know which grid sites fulfill the requirements given in the JDL file of the job. This can be queried by using

```
glite-wms-job-list-match <-a|-d <delegation_id>> <--rank>  <jdl_file>
```

with the optional parameter `--rank` sorting the matching job queues by their ranking in the WMS (this ranking depends, for example, on the number of free job slots).

C.2.2   Job Information

After a job or several jobs have been submitted, the user wants to know if the job has already been transferred to a grid site (if yes, to which one), if it is running, and, finally, if it has successfully finished.

All this information can be obtained by using the following command:

```
glite-wms-job-status [-v <0|1|2|3>] [-i <job_id_file>] <jobID>
```

- `glite-wms-job-status` needs to be given one or several job identifiers, which can either be passed via `<jobID>`, or in one or several job identifier files `<job_id_file>`. The use of job identifier files is highly recommended.

status	description
Submitted	job submission has been logged in the Logging and Bookkeeping (LB)
Wait	job is being matched to the resources
Ready	job is being sent a matching CE
Scheduled	job is scheduled in the queue controlled by the selected CE
Running	job is running on a WN of the selected CE queue
Done	job has terminated without grid-specific errors
Cleared	the user has retrieved the job output
Aborted	job has been aborted by the grid middleware
Canceled	job has been canceled by the user

Table C.1: Possible states for a grid job in the gLite middleware.

- The level of information, the so-called verbosity level, can be raised via the `-v` option. This option is extremely helpful in debugging failing jobs.

A typical output has the following format:

```
> glite-wms-job-status -i myJobIds.id



************************************************************
BOOKKEEPING INFORMATION:

Status info for the Job : https://lb103.cern.ch:9000/gzPu2Mdz2tSOux2bevSfmA
Current Status:      Ready
Destination:         cmsgrid02.hep.wisc.edu:2119/jobmanager-condor-cms
Submitted:           Mon Oct 15 09:11:53 2007 CET
************************************************************
```

Possible job states are listed in Table C.1.

C.2.3   Output sandbox retrieval

With the job being successfully finished (status 'Done'), the user can easily retrieve the output sandbox with the following command:

command	description
lfc-ls	lists entries in a directory
lfc-mkdir	creates a directory
lfc-rm	removes a file or directory
lfc-rename	renames a file or directory
lfc-ln	creates a symbolic line to a file or directory
lfc-setacl	sets access control lists for a file or directory
lfc-setcomment	adds a comment or replaces an old comment for a file or directory
lfc-delcomment	deletes a comment for a file or directory

Table C.2: Most important commands for the LCG File Catalog.

```
glite-wms-job-output [--dir <save_directory>][-i <job_id_file>] <jobID>
```

- As with `glite-wms-job-status`, one or several job identifiers can be passed either via `<jobID>` or via one or several job identifier files `<job_id_file>`.

- It is advisable to pass a directory in which the output sandbox will be saved via `--dir <save_directory>`; if `<save_directory>` does not exist, it will be created. If this parameter is not used, a standard directory is used; this directory has to be set up by the administrator and usually is `/tmp`.

C.3   Data Management

The gLite middleware uses the LFC (see section 4.4) as its file catalog. A VO can have several instances of the LFC running in parallel, so the first step on a UI or in a job script on a WN is to set the system variable `$LFC_HOST` to the preferred LFC.

The LFC offers a directory structure similar to the Linux one. All 'grid directories' have the structure `/grid/<VO_name>/furtherSubdirectories`. The commands are in the style of Linux, with the prefix `lfc-`, e.g. `lfc-ls`, and `lfc-rm` (most important `lfc`-commands are listed in Table C.2).

In order to store data on the grid, the user has to know which SEs are available in his/her VO. This can be achieved by

```
lcg-infosites --vo <VO_name> se
```

- The SE list obtained with this command may contain SEs that are currently not working; users should also use information obtained from monitoring systems when choosing a SE for their data.

- This command can also be used to find out other grid components available in a VO, e.g. CEs and BDIIs.

- The VO specified as a parameter does not need to correspond to the user's VO.

Grid jobs often need access to files that are too large for the input sandbox, so these files need to be put on a storage element. This can be done by:

```
lcg-cr [--vo <VO_name>] [-v] [-d <SE_name>] \
    [-l lfn:<full_file_name_in_LFC>] file:<full_local_file_name>
```

- The command returns the GUID of the file to the standard output.

- If the option `-d <SE_name>` is not given, the file will be stored on a default SE. This SE, the so-called 'close SE', is defined during the installation of a UI or a WN.

- The use of `-l lfn:<full_file_name_in_LFC>` is highly advisable, as it gives the user an easy overview of the files stored on the grid. Otherwise, the file can be only accessed via the GUID returned by this command.

- The VO only needs to be specified via `--vo <VO_name>` if the environmental variable is not defined or not set for the needed VO.

Files that are read often from different grid sites should be replicated, i.e. the file exists on several SEs with the GUID and the LFNs being the same on all SEs. The replication command is

```
lcg-rep [--vo <VO_name>] [-v] [-d <target_SE_name>] \
    <file_protocol>:<file identifier>
```

- If the option `-d <SE_name>` is not stated, the file will be replicated to a close SE (as described for `lcg-cr`).

- The file protocol `<file_protocol>` can be `guid` or `lfn`, while the `<file identifier>` needs to be the GUID or the logical file name in the LFC, respectively.

The locations of the existing replicas of a file can be retrieved via the `lcg-cr` command; an example is

command	description
lcg-lr	lists all replicas of a file
lcg-lg	returns the GUID of a file
lcg-ls	lists all aliases of a file
lcg-rf	registers a file (which is on a SE) to the file catalog
lcg-aa	adds alias for a file

Table C.3: Summary of gLite commands used in management of logical file names in the LFC.

```
> lcg-lr --vo cms lfn:/grid/cms/cjung/file1.root
srm://grid003.ca.infn.it/dpm/ca.infn.it/home/cms/generated/2007-07-10\
  /filee840f948-cece-45dc-8caf-4676c37f069e
srm://se.cc.ncu.edu.tw/dpm/cc.ncu.edu.tw/home/cms/generated/2007-07-10\
  /file5aee9ad1-15fd-4653-96ad-f53c668aea25
srm://srm-disk.pic.es/pnfs/pic.es/data/cms/generated/2007-07-10\
  /file210fe510-5c6e-46c0-902e-8e6d345f9165
```

All replicas are listed with their respective storage protocol (in this example SRM (Storage Resource Manager)); a file path includes the name of the SE and the physical location of the file.

When deleting a file from the grid, the user needs to choose between deleting a certain replica or all instances of the file. The former is performed via

```
lcg-rep [--vo <VO_name>] [-v] [-s <SE_name>] \
    <file_protocol>:<file identifier>
```

while the later needs the parameter -a for 'all'

```
lcg-rep [--vo <VO_name>] [-v] \
    -a <file_protocol>:<file identifier>
```

The gLite middleware provides several commands for management of logical file names; these commands are summarized in Table C.3.

List of Figures

List of Tables

Bibliography

[Aal] T. Aaltonen et al., The CDF Collaboration, First Measurement of the W Boson Mass in Run II of the Tevatron,
Phys. Rev. Lett. 99,. 151801 (2007).

[APT] APT,
`http://www.debian.org/doc/manuals/apt-howto/index.en.html`

[Ber] C, Berger, *Elementarteilchenphysik*, B.G. Teubner Stuttgart Leipzig, 2006

[BL] V. Blobel, E. Lohrmann, *Statistische und numerische Methoden der Datenanalyse*, B.G. Teubner Stuttgart Leipzig, 1998.

[Bue1] Büge *et al.*, Integrating a heterogeneous and shared computer cluster into grid, Procedings of CHEP 2006

[Bue2] V. Büge, Aufbau eines Grid-Standorts zum Einsatz der CMS-spezifischen Software und Messung von Parametern des W- und Z-Bosons am LHC, Diploma thesis, IEKP-KA/2005-21,
`http://www-ekp.physik.uni-karlsruhe.de/pub/web/thesis/iekp-ka2005-21.pdf`

[Castor] CASTOR - CERN Advanced STORage manager - homepage,
`http://castor.web.cern.ch/castor/`

[CDFEW] CDF Run 2 Electroweak Public Results.
`http://fcdfwww.fnal.gov/physics/ewk/`

[CMS] The Compact Muon Solenoid detector at LHC, CMS Collaboration, to be submitted to the Journal of Instrumentaion (JINST)

[CMSD] Julia Andreeva, Juha Herrala, CMS Dashboard of Grid Activity, presentation given at EGEE User Forum 2006,
`http://indico.cern.ch/contributionDisplay.py?contribId=102&`
`sessionId=22&confId=286`

[CMSO] CMS Experiment Outreach homepage, `http://cms.cern.ch`

[ColSop] John C. Collins and Davison E. Soper, Angular distribution of dileptons in high-energy hadron collisions,
Phys. Rev. D 16, 2219 - 2225 (1977)

[CO1] CMS Experiment homepage, Poster of the CMS Tracking Detectors,
      `http://cms.cern.ch`

[CO2] CMS Experiment homepage, Slice through CMS showing particles incident on
      the different sub-detectors,
      `http://cms.cern.ch`

[CRAB] CRAB (CMS Remote Analysis Builder) homepage,
      `http://cmsdoc.cern.ch/cms/ccs/wm/www/Crab/index.html`

[dCache] dCache homepage, `http://www.dcache.org`

[D-Grid] D-Grid Initiative, D-Grid homepage,
      `http://www.d-grid.de`

[EGEE] Enabling Grids for E-sciencE, EGEE homepage,
      `http://www.eu-egee.org/`

[ETDR] The CMS collaboration, *"CMS: ECAL Technical Design Report"*,
      CERN, CERN/LHCC 97-33, 1997

[FK] Ian Foster, Carl Kesselman, The Grid: Blueprint for a New Computing Infras-
      tructure, Morgan Kaufmann Publishers 1998

[FKT] Ian Foster, Carl Kesselman, Steven Tuecke,The Anatomy of the Grid,
      `http://www.globus.org/alliance/publications/papers/anatomy.pdf`

[Fos] Ian Foster, What is the Grid? A Three Point Checklist,
      `http://www-fp.mcs.anl.gov/~foster/Articles/WhatIsTheGrid.pdf`

[Geant1] GEANT 4 web page, CERN
      `http://cern.ch/geant4`

[Geant2] Agostinelli, S. *et al.*, GEANT4: A simulation toolkit., *Nucl. Instrum. Meth.*
      A506, 2003, 250-303

[GGK] W.T. Giele, E.W.N. Glover, David A. Kosower, Higher Order Corrections To
      Jet Cross-Sections In Hadron Colliders, Nucl.Phys.B403:633-670,1993, [HEP-PH
      9302225]

[GiKe] W. T. Giele, S. Keller, Determination of W-Boson Properties at Hadron Col-
      liders, Phys.Rev.D57:4433-4440 (1998)

[Globus] The Globus Alliance homepage,
      `http://www.globus.org/`

[GGUS] Antoni *et al.*, Global Grid User Support: the model and experience in the
      Worldwide LHC Computing Grid, Procedings of CHEP 2006

[gLite] gLite Lightweight Middleware for Grid Computing, glite homepage, `http://www.glite.org/`

[gLUG] gLite User Guide, `https://edms.cern.ch/file/722398//gLite-3-UserGuide.pdf`

[GMaps] Google Maps, `http://maps.google.com`

[Gold] J. Goldstone, *Nuov. Com.* **10** (1961) 154

[Gor] , A. S. Gordon, Measurement of the W Boson Mass With the Collider Detector at Fermilab, PhD thesis, Harvard University, 1998

[Gri] D. Griffiths, Introduction to Elementary Particles, WILEY-VCH 2004

[GridKa] Grid Computing Center Karlsruhe, "GridKa homepage", `http://grid.fzk.de/`

[Gui] J. Guillaud, "PYTHIA miniguide", available at `http://lappc-in39.in2p3.fr/Pythia/`

[Hay] S. Haywood *et al.*, Electroweak Physics, "Proceedings of the Workshop on Standard Model Physics (And More) at the LHC", CERN Yell. Rep. 2000-004, Geneva 2000, hep-ph/0003275

[HERWIG] G. Corcella *et al.*, "HERWIG 6.5 release note", arXiv:hep-ph/0210213.

[IEKPCluster] P. Schemitz and M. Stanitzki, Aufbau eines Datenanalyse-Clusters, IEKP-KA/2003-12, `http://www-ekp.physik.uni-karlsruhe.de/clusmon/EKPplus/ekpplus-iekp-ka2003-12.pdf`

[IEKPGrid] Büge *et al.*, Integrating the IEKP Linux Cluster as a Tier-2/3 prototype centre into the LHC computing grid, 2006, `http://www-ekp.physik.uni-karlsruhe.de/pub/web/thesis/2006-03.pdf`

[ISAJET] H. Baer, F. E. Paige, S. D. Protopescu and X. Tata, "ISAJET 7.69: A Monte Carlo event generator for p p, anti-p p, and e+ e- reactions", arXiv:hep-ph/0312045.

[Jackson] John David Jackson, Classical Electrodynamics, Wiley 1998

[JDL] F. Pacini, Job Description Language Attributes Specification for the gLite middleware (submission through WMProxy service), `https://edms.cern.ch/document/590869/1/`

[Kemp] Y.Kemp, Identification of Electrons in the Forward Region of the CDF Experiment for the Search for Electroweak Top Quark Production, PhD Thesis, IEKP-KA/2006-1, `http://www-ekp.physik.uni-karlsruhe.de/pub/web/thesis/iekp-ka2006-1.pdf`

[Leone] INFN: Pisa, Review of W and Z physics at the Tevatron, HEP EPS Lisbon, July 21-27 2005

[LEPEWWG] The LEP Electroweak Working Group, "LEPEWWG homepage", `http://lepewwg.web.cern.ch`

[Mart] A. D. Martin and R. G. Roberts and W. J. Stirling and R. S. Thorne, Parton Distributions and the LHC: W and Z Production, European Physical Journal C, 14, `http://www.citebase.org/abstract?id=oai:arXiv.org:hep-ph/9907231`

[MirOhn] E. Mirkes and J. Ohnemus, *W and Z Polarization Effects in Hadronic Collisions*, Phys.Rev. D50 (1994) 5692-5703, 1994. `arxiv.org/abs/hep-ph/9406381`

[Nad] P. M. Nadolsky and Z. Sullivan, DF uncertainties in WH production at Tevatron, `arxiv.org/hep-ph/0110378`

[Nordu] NorduGrid, NorduGrid homepage, `http://www.nordugrid.org/`

[OSG] Open Science Grid, Open Science Grid homepage, `http://www.opensciencegrid.org/`

[Oscar1] OSCAR web page, CERN `http://cmsdoc.cern.ch/OSCAR/`

[Oscar2] Abdoulline *et al.*, An Object-Oriented Simulation Package for CMS, Procedings of CHEP 2004

[PAW] PAW web page, CERN `http://paw.web.cern.ch/paw/`

[PDG] Review of Particle Physics, W.-M. Yao *et al.*, Journal of Physics G **33**, 1 (2006) 2006

[Photos] E. Barberio, Z. Was, PHOTOS - a universal Monte Carlo for QED radiative corrections: version 2.0, Computer Physics Communications, Volume 79, Issue 2, p. 291-308.

[PhysJG] V. Büge *et al.*, Prospects for the precision measurement of the W mass with the CMS detector at the LHC, 2006. `CERN-CMS-NOTE-2006-061` and **J.Phys.G34:N193-N220,2007**.

[Pich1] A. Pich, The Standard Model of Electroweak Interactions, 2005, arXiv:hep-ph/0502010

[Pich2] A. Pich, Aspects of Quantum Chromodynamics 2000, arXiv:hep-ph/0001118 **JHEP 0310 (2003) 046**.

[Pos] A. Poschlad, Gridbasierte Analyse elektroschwacher Eichbosonen, Diploma thesis, to be published.

[PTDR1] The CMS collaboration, *"CMS Physics Technical Design Report, Volume I: Detector Performance and Software"*,
CERN, CERN/LHCC 2006-001, 2006

[PTDR2] The CMS collaboration, *"CMS Physics Technical Design Report, Volume I: Detector Performance and Software"*, **CERN, CERN/LHCC 2006-001, 2006**

[Pum] J. Pumplin *et al.*, Inclusive Jet Production, Parton Distributions, and the Search for New Physics,

[PYTHIA] T. Sjostrand, P. Eden, C. Friberg, L. Lonnblad, G. Miu, S. Mrenna and E. Norrbin, "High-energy-physics event generation with PYTHIA 6.1", Comput. Phys. Commun. **135** (2001) 238, [arXiv:hep-ph/0010017].

[ROOT] ROOT web page, CERN
http://root.cern.ch/

[SAM] Sam Overview on LGC wiki, CERN
https://twiki.cern.ch/twiki/bin/view/LCG/SAMOverview

[Sch] A, Schmidt, Entwicklung von Analyse-Software und Bestimmung von Parametern des W-Bosons am LHC durch Vergleich mit Z-Bosonen. Diploma thesis, IEKP-KA/2004-2,
http://www-ekp.physik.uni-karlsruhe.de/pub/web/thesis/schmidt_dipl.pdf

[Schm] P. Schmüser, Feynman-Graphen und Eichtheorien für Experimentalphysiker, Springer-Verlag 1995

[SFTGM] Site Functional Test GoogleMap,
http://goc02.grid-support.ac.uk/googlemaps/lcg.html

[SNV] J. Smith, W. L. van Neerven, and J. A. M. Vermaseren, Transverse Mass and Width of the W Boson, Phys. Rev. Lett. 50, 1738 - 1740 (1983)

[TTDR1] The CMS collaboration, *"CMS: The Trigger and Data Acquisition project, Volume I. The Level-1 Trigger"*,
CERN, CERN/LHCC 2000-38, 2000

[Wein] S. Weinberg, The Quantum Theory of Fields (Vol. II): Modern Applications, Cambridge University Press 1996

[Wil] S. Willenbrock, "The standard model and the top quark. ((U))", arXiv:hep-ph/0211067.

[WLCG] Worldwide LHC Computing Grid, WLCG homepage,
http://lcg.web.cern.ch

[YAIM] YAIM in the EGEE section of the CERN TWiki, http://www.yaim.info

Acknowledgements